

## REPORT DOCUMENTATION PAGE

AFRL-SR-BL-TR-99-

Public reporting burden for this collection of information is estimated to average 1 hour per response, including gathering and maintaining the data needed, and completing and reviewing the collection of information. Send comments regarding this burden estimate or any other aspect of this collection of information, including suggestions for reducing this burden, to Washington Headquarters Services, Directorate for Information Operations and Reports, 1215 Jefferson Davis Highway, Suite 1204, Arlington, VA 22202-4302, and to the Office of Management and Budget, Paper Project Collection (0148-0187), Washington, DC 20503.

0046

rces,  
of this  
erson

1. AGENCY USE ONLY (Leave blank)		2. REPORT DATE January 1999	3. REPORT TYPE AND DATES COVERED Final Technical Report 1 Mar 98 to 30 Nov 98
4. TITLE AND SUBTITLE "The Effects of Expansion Waves on Vortices and Turbulence"			5. FUNDING NUMBERS F49620-98-1-0358 2307/AS
6. AUTHOR(S) G. Briassulis, J. H. Agui and Yiannis Andreopoulos			
7. PERFORMING ORGANIZATION NAME(S) AND ADDRESS(ES) Experimental Aerodynamics and Fluid Mechanics Laboratory Department of Mechanical Engineering City College of CUNY New York, NY 10031			8. PERFORMING ORGANIZATION REPORT NUMBER
9. SPONSORING/MONITORING AGENCY NAME(S) AND ADDRESS(ES) AFOSR/NA 801 N. Randolph Street, Rm 732 Arlington, VA 22203-1977			10. SPONSORING/MONITORING AGENCY REPORT NUMBER  F49620-98-1-0358
11. SUPPLEMENTARY NOTES			
12a. DISTRIBUTION AVAILABILITY STATEMENT Approved for public release; distribution unlimited.			12b. DISTRIBUTION CODE
13. ABSTRACT (Maximum 200 words) A decaying compressible nearly homogeneous and nearly isotropic, grid generated turbulent flow has been set-up in a large scale shock tube research facility. Experiments have been performed by using instrumentation with spatial resolution of the order of 7 to 26 Kolmogorov viscous length scales. A variety of turbulence generating grids provided a wide range of turbulence scales with flow Mach numbers ranging from 0.3 to 0.6 and turbulent Reynolds number up to 700. The decay of Mach number fluctuations was found to follow a power law similar to that describing the decay of incompressible isotropic turbulence. It was also found that the decay coefficient and the decay exponent decrease with increasing Mach number while the virtual origin increases with increasing Mach number. A mechanism possibly responsible for these effects appears to be the inherently low growth rate of compressible shear layers emanating from the cylindrical rods of the grid. Measurements of time-dependent, three dimensional vorticity vector were attempted for the first time with a 12 wire miniature probe. This also allowed estimates of dilatation, compressible dissipation and dilatational stretching to be obtained. It was found that the fluctuations of these quantities increase with increasing Mach number of the flow. The time-dependent signals of enstrophy, vortex stretching/tilting vector and dilatational stretching vector found to exhibit a rather strong intermittent behavior which is characterized by bursts of high amplitudes with values up to 8 times their r.m.s. followed by less violent periods of time. Several of these bursts are evident in all signals suggesting the existence of a dynamical flow phenomenon as a common cause.			
14. SUBJECT TERMS			15. NUMBER OF PAGES
			16. PRICE CODE
17. SECURITY CLASSIFICATION OF REPORT UNCLASSIFIED	18. SECURITY CLASSIFICATION OF THIS PAGE UNCLASSIFIED	19. SECURITY CLASSIFICATION OF ABSTRACT UNCLASSIFIED	20. LIMITATION OF ABSTRACT UL

# The structure of weakly compressible grid generated turbulence

by

G. Briassulis, J.H. Agui and Y. Andreopoulos  
Experimental Aerodynamics and Fluid Mechanics Laboratory  
Department of Mechanical Engineering  
City College of CUNY  
New York, New York 10031 USA

## Abstract

A decaying compressible nearly homogeneous and nearly isotropic, grid generated turbulent flow has been set-up in a large scale shock tube research facility. Experiments have been performed by using instrumentation with spatial resolution of the order of 7 to 26 Kolmogorov viscous length scales. A variety of turbulence generating grids provided a wide range of turbulence scales with flow Mach numbers ranging from 0.3 to 0.6 and turbulent Reynolds number up to 700. The decay of Mach number fluctuations was found to follow a power law similar to that describing the decay of incompressible isotropic turbulence. It was also found that the decay coefficient and the decay exponent decrease with increasing Mach number while the virtual origin increases with increasing Mach number. A mechanism possibly responsible for these effects appears to be the inherently low growth rate of compressible shear layers emanating from the cylindrical rods of the grid. Measurements of time-dependent, three dimensional vorticity vector were attempted for the first time with a 12 wire miniature probe. This also allowed estimates of dilatation, compressible dissipation and dilatational stretching to be obtained. It was found that the fluctuations of these quantities increase with increasing Mach number of the flow. The time-dependent signals of enstrophy, vortex stretching/tilting vector and dilatational stretching vector found to exhibit a rather strong intermittent behavior which is characterized by bursts of high amplitudes with values up to 8 times their r.m.s. followed by less violent periods of time. Several of these bursts are evident in all signals suggesting the existence of a dynamical flow phenomenon as a common cause.

## 1. Introduction

A fundamental understanding of compressible turbulence in the absence of shock wave interactions, is necessary for the development of supersonic transport aircraft, combustion processes, as well as high speed rotor flows. Compressibility effects on turbulence are significant when the energy associated with dilatational fluctuations is large or when the mean flow is compressed or expanded. Most of the previous work on compressible turbulence has been carried out in shear layers (see Gutmark et al., 1995, for the most recent review on compressible free shear flows) or boundary layers (see Spina et al., 1994). Previous work on homogeneous and isotropic compressible turbulence (see figure 1 for a typical flow schematic) is very limited although this flow is the best candidate for testing calculation methods and turbulence modeling. The reader is referred to the work by Lele (1994) where different contributions to the understanding of compressibility effects on turbulence are reviewed in detail. A substantial amount of experimental work dealing with the *incompressible* grid generated turbulence already exists (see Compte-Bellot and Corrsin, 1966, 1971). The effects of grid and perforated plates as flow straighteners on the free stream turbulence was studied by Tan-Atichat et al. (1982) for Reynolds number based on mesh size  $Re_M$  up to 735. They found that the performance of the grid is depended on the characteristics of the incoming flow. For larger range of mesh Reynolds number  $Re_M$  ranging from 12800 to 81000, Frenkiel et al. (1979) performed experiments where they observed that data exhibit a high degree of similarity. Analysis of the higher order correlations and moments on the turbulent velocity components revealed that the turbulent fluctuations is of non-Gaussian character. Tavoularis et al., (1978) presented a comprehensive study of values of the skewness of velocity derivative for a variety of flow fields and  $Re_\lambda$ . This study indicated that the skewness of the velocity derivative reaches a maximum at  $Re_\lambda=5$  and then gradually decreases as the turbulent Reynolds number increases.

1 9990224027

Grid turbulence at large mesh Reynolds number ( $1.2 \times 10^5$  to  $2.4 \times 10^6$ ) was studied by Kistler and Vrebalovich (1966). To avoid compressibility effects the mean flow was kept below 60 m/sec. The flow field under investigation was anisotropic but nevertheless they concluded that if the  $-5/3$  slope is to be used for the spectral curve then a minimum turbulence Reynolds number ( $Re_\lambda$ ) of 300 is required. From the literature review it is evident that in all of the above studies on grid generated turbulence compressibility effects were absent or undesirable. One of the first attempts to generate isotropic turbulence was described by Honkan and Andreopoulos (1992) and Honkan, Watkins and Andreopoulos (1994) who set up a flow with  $Re_\lambda \approx 1000$ . Recently Budwig et al (1995) and Zwart et al. (1996) work with compressible streams for three different Mach numbers in a supersonic wind tunnel. The decay coefficient for the lowest Mach number of 0.16 was found to be -1.24 and for the highest Mach number of 1.6 was -0.49. Inhomogeneity across the test section prevented them from measuring decaying turbulence.

The present experimental work is a fundamental study of compressibility effects in grid generated turbulence for flows with Mach numbers ranging from 0.3 to 0.6. The measurements were carried out inside the induced flow behind a traveling shock wave in a shock tube facility. Time-dependent measurements of one, two or three velocity components have been carried out. Measurements of the vorticity vector and the full dissipation tensor at limited locations inside the flow have been also attempted for the first time in compressible flows.

It should be mentioned that in the present work there is no interaction of the flow with the shock wave which causes sudden compression of the flow field, as it was in our previous work (Briassulis and Andreopoulos, 1994, 1996).

## 2. Experimental set-up

The experiments were performed in the Shock Tube Research Facility (STURF), shown in figure 2a, which is located at the Mechanical Engineering Department of CCNY. The large dimensions of this facility, 1 ft in diameter and 88 ft in length, provide an excellent platform for high spatial resolution measurements of turbulence with long observation time of steady flow. The induced flow behind the traveling shock wave passes through a turbulence generating grid properly installed in the beginning of the working section of the facility. Several turbulence generating grids were used at three different flow Mach numbers. All grids had about the same solidity but different mesh sizes which provided a large variety of length scales. The velocity of the induced flow behind the shock wave, depends on the rupture pressure of the diaphragm, i.e. driver strength. The working (test) section is fitted with several hot-wire and pressure ports. Thus pressure, velocity and temperature data can be acquired simultaneously at various locations downstream from the grid (see figure 2b), and therefore reduce the variance between measurements. High frequency pressure transducers, hot wire anemometry and Rayleigh scattering techniques for flow visualization have been used in the present investigation.

To assess the flow quality in the facility several tests were carried out. First the shock wave was visualized in order to check its inclination and planform by using a non intrusive optical technique using a YAG laser emitting at the UV range and a UV sensitive, 16 bit CCD camera made by ASTROMED Corporation. Second the flow homogeneity was checked by a hot-wire rake constructed for simultaneous acquisition of velocity and temperature data at various radial positions. Details of an extensive evaluation of the flow quality can be found in the work of Briassulis et al. (1996).

To resolve simultaneously two dimensional velocity components with hot wires, a cross wire (X-wire) arrangement was used. New three-wire probes were designed and custom built by AUSPEX Corp. Six different three-wire probe assemblies were used concurrently at different downstream locations, all adjustable to different lengths, each carrying 2 hot-wires in an X configuration and one cold-wire for simultaneous velocity and temperature measurements respectively. The three-wire probes were equipped with  $5 \mu\text{m}$  Platinum/Tungsten wires for velocity measurements and with a  $2.5 \mu\text{m}$  Platinum/Tungsten wire for temperature measurements. To eliminate any wake effects from upstream probes on any downstream, all of the probes were staggered at different distances from the tube wall and 90 degrees apart every other probe. The cross wires were driven by DANTEC anemometers model CTA56C01 and the temperature wires were connected to EG&G model 113 low noise, battery operated pre-amplifiers/filters. The output signal of the cold-wire was digitally compensated for thermal lag up to frequencies of interest. For more details on the hot-wire techniques applicable to shock tubes see Briassulis et al. (1995) where estimates of uncertainties in the measurements are also given.

Time dependent pressure fluctuations were obtained by 6 miniature high frequency Kulite pressure transducers

installed on the shock tube wall.

During each experiment all signals were acquired simultaneously with the ADTEK data acquisition system. The ADTEK AD830 board is a 12 bit EISA data acquisition system, capable of sampling simultaneously 8 channels at 333 KHz each channel. Three of those boards are currently available providing 24 simultaneous sampled channels at 333 KHz per channel. It should be mentioned that no sample-and-hold units were used in the present data acquisition since each channel was dedicated to an individual Analog to Digital converter.

This experimental set-up provided time dependent measurements of two velocity components, temperature and wall pressure at several locations of the flow field simultaneously. In addition, time dependent three-dimensional vorticity measurements were carried out by using a new vorticity probe (see Andreopoulos and Honkan, 1996 and Honkan and Andreopoulos, 1997). Details of this technique are given in section 3 below.

The bulk flow parameters of the experiments performed are summarized in table 1 and include the grid mesh density, the mesh size  $M$ , the flow Mach number  $M_{flow}$ , the Reynolds number based on mesh size  $Re_M$ , the Reynolds number based on Taylor's microscale  $\lambda$ ,  $Re_\lambda$  and the solidity of the grids  $\sigma$ . The grids were selected so that the open area is higher than the corresponding sonic area for a given pressure ratio/Mach number.

Grid(Meshes/in)	$M$ (mm x mm)	$\sigma$	$M_{flow}$	$Re_M$	$Re_\lambda$
5x5	5.1x5.1	0.37	0.371	59654	222
5x5	5.1x5.1	0.37	0.477	86315	250
5x5	5.1x5.1	0.37	0.576	102421	325
4x4	6.35x6.35	0.44	0.354	68208	223
4x4	6.35x6.35	0.44	0.446	105389	277
4x4	6.35x6.35	0.44	0.594	132921	355
3x3	8.5x8.5	0.39	0.321	81687	224
3x3	8.5x8.5	0.39	0.474	124203	316
3x3	8.5x8.5	0.39	0.564	215043	654
2x2	12.7x12.7	0.38	0.346	137319	267
2x2	12.7x12.7	0.38	0.436	169025	405
2x2	12.7x12.7	0.38	0.592	261667	737
1.33x1.33	19.05x19.05	0.26	0.368	200371	270
1.33x1.33	19.05x19.05	0.26	0.504	295721	550
1.33x1.33	19.05x19.05	0.26	0.607	398661	680

Table 1: Bulk flow parameters of the experiments performed.

### 3. The vorticity probe

A new multi hot-wire probe has been developed which is capable of measuring velocity-gradient related quantities in non-isothermal flows or in compressible flows. The present probe has been build upon the experience gained with vorticity measurements in incompressible flows (see Honkan and Andreopoulos, 1997) by using a probe with nine wires. The present probe which consists of 12 wires is a modification of the original design by Honkan and Andreopoulos (1997) hereafter referred as HA. The three additional wires were operated in the so called Constant Current Mode and used to measure time dependent temperature.

Since the probe essentially consists of a set of three modules it is necessary to provide several key features of the individual hot-wire modules. Each module contains three hot-wires operated in the Constant Temperature Mode (CTM) and one cold-wire sensor operated in the Constant Current Mode (CCM). Each wire of the triple wire sub-



module is mutually orthogonal to each other, thus oriented at 54.7 degrees to the probe axis. Each of the 5  $\mu\text{m}$  diameter tungsten sensors is welded on two individual prongs which have been tapered at the tips. Each sensor is operated independently since no common prongs are used. Each of the 2.5  $\mu\text{m}$  diameter cold-wire was located on the outer part of the sub-module.

The hot-wire output voltage  $E$  is related to the effective cooling velocity,  $U_{\text{eff}}$  through the well known King's law:

$$\frac{E^2}{(T_w - T_0)} = A \left[ \frac{T_0}{T_r} \right]^a + B \left[ \frac{T_0}{T_r} \right]^b \cdot (\rho U_{\text{eff}})^n \quad (3.1)$$

where  $T_w$  is the hot-wire temperature,  $T_0$  is the total temperature of the flow and  $T_r$  is a reference temperature, the ambient temperature in the present case. The values of the exponent  $a$  and  $b$  were taken as suggested by Kovaszny (1950)  $a=b=0.768$ . The effective velocity is related to  $U_N$ ,  $U_T$  and  $U_B$ , the normal, tangential and binormal components of the velocity vector respectively, by

$$U_{\text{eff}}^2 = U_N^2 + k^2 U_T^2 + h^2 U_B^2 \quad (3.2)$$

where  $k$  and  $h$  are yaw and pitch coefficients. Details of the techniques associated with the use of triple wire probes can be found in Andreopoulos (1983a) while estimates of errors related to probe geometry and turbulence intensity are described by Andreopoulos (1983b).

The probe, shown schematically in figure 3 consists of a set of three individual modules with four wire sensors each, put together so that the probe remains geometrically axisymmetric.

In selecting the dimensions of the vorticity probe several conflicting considerations have to be taken into account. The individual wire length, the size of the individual sub-module and the size of the overall probe should be as small as possible so that small scales can be resolved adequately since it is known that most of the contributions to vorticity come from small scales of turbulence. However, small wire spacing can lead to thermal interference and cross talk between the wires. This was of particular concern in the present case because of the high overheat ratio used in the experiments. Yaw and pitch tests of the probe were carried out in order to identify any thermal effects on wires located in the heated wake of a neighboring wire located upstream. These tests indicated no thermal interference among the wires. The reason for this behavior is that the spreading rate of the thermal wakes is reduced in high Reynolds number flows.

The requirement to reduce the probe size had to be counterbalanced with the requirement that the spacing between the sub-modules and the individual wires should be finite so that the velocity gradients which were used to compute vorticity and strain-rates do not disappear.

The present probe design differs from that used in the work by HA in the following aspects:

- I. It consists of 12 wires with 3 of them measuring temperature;
- II. The overheat ratio in which the hot-wires were operated was close to 130 %. This high overheat ratio was required in order to maintain the heat transfer rate from the wire to the driven flow at substantial levels.
- III. The wire diameter of the velocity sensing wires was 5  $\mu\text{m}$ . This reduced the length to diameter ratio of each wire to about 200 which is large enough to suppress end heat conduction effects. Attempts to work with 2.5  $\mu\text{m}$  wires were unsuccessful because of substantial strain-gauging effects and wire breakage.

Velocity calibrations were carried out inside the shock tube by firing the tube at various pressures corresponding to Mach numbers anticipated to be found in the flows under investigation. Yaw and pitch calibration of the probe was also carried out *in-situ*. These data help to extend a complete and detailed map of the yaw and pitch response of the probe obtained in a low speed wind tunnel to the subsonic range of flow velocities needed in the present investigation.

The digitized signals were processed off-line. The cold-wire signals were first converted to total temperature which, together with the hot wire signals were used to obtain instantaneous three dimensional mass fluxes at three neighboring locations within the probe. Numerical techniques and algorithms used in the computations of velocity gradients were very similar to those described by HA. The only difference is that in the present case mass fluxes and

their gradients were computed at the centroid of each module instead of velocities and velocity gradients.

Mass fluxes were further separated into density and velocity by using the method adopted by Briassulis et al. (1996). Decoupling density from mass fluxes assumes that pressure fluctuations are small. This is the "weak" version of the original "strong Reynolds analogy" hypothesis of Morkovin (1956). The original hypothesis is based on the assumption that pressure and total temperature fluctuations are very small. In the present work, total temperature was measured directly and therefore no corresponding assumptions were needed. The pressure, however, was measured at the wall and not at the location of the hot wire. The mean value of this pressure signal was used to separate the density and velocity signals since no mean pressure variation has been detected across a given section of the flow. The procedure involves an expression for mass flux,  $m_i$ , in terms of total temperature,  $T_0$ , and pressure,  $p$ , at the centroid of each module

$$m_i = \rho U_i = \frac{p U_i}{RT} = \frac{p U_i}{R \left[ T_0 - \frac{U_k U_k}{2c_p} \right]} \quad (3.3)$$

$U_i$  is the instantaneous velocity component,  $i=1,2$  or  $3$  and  $U_k U_k = U_1^2 + U_2^2 + U_3^2$ . The velocity can be decomposed into  $U_i = \bar{U}_i + u_i$

An iterative scheme was used to decouple density and velocity. During the first iteration it was assumed that the quantity  $(u_2^2 + u_3^2)/2c_p$ , where  $u_2$  and  $u_3$  are the velocity components in the spanwise and normal directions respectively, is substantially smaller than the quantity  $T_0 - U_1^2/2c_p$ . Then the above relation (3.3) can be rearranged to obtain a quadratic equation for  $U_i$ ,

$$\frac{R m_i}{2c_p} U_i^2 + p U_i - m_i R T_0 = 0 \quad (3.4)$$

For each digitized point,  $T_0$  and  $m_i$  were available instantaneously at the centroid of each module while pressure was measured at the wall. If the thin shear layer approximation is invoked then the pressure at the centroid of the module which appears in (3.4) can be substituted by the mean pressure at the wall. This assumption is justified because pressure fluctuations are extremely small and therefore their impact on velocity fluctuations is minimal.

The discriminant of the above equation (3.4)  $\Delta = p^2 + 2m_i^2 R^2 T_0 / c_p$  is always positive and therefore there are two real roots: one positive and one negative. The negative root is unrealistic and only the positive root was accepted. The longitudinal velocity component  $U_1$  was computed first while the other two components were obtained from the mass flux ratios as  $u_2 = m_2/m_1 U_1$  and  $u_3 = m_3/m_1 U_1$ . These values provided the first estimate of the velocity components which were used to obtain a better estimate of the  $U_k^2/2c_p$  in (3.3) which subsequently was used to improve the estimate of the velocity components. This iterative scheme required no more than two iterations for convergence.

#### 4. Qualification tests

The newly designed probe has been evaluated by carrying measurements of vorticity and turbulent stresses in the incompressible boundary layer flow where the data of HA were obtained. This allowed a direct comparison of the present data obtained at  $Re_\theta = 5300$  with the data of HA obtained at  $Re_\theta = 2800$ .

The bulk flow parameters of the boundary layer experiments are given in table 2:

$U_e$ (m/s)	Boundary layer thickness $\delta$ (mm)	Momentum thickness $\theta$ (mm)	$Re_\theta$	Friction velocity $u_\tau$ (m/s)
9.1	97	9.21	5,300	0.315

Table 2: Incompressible boundary layer flow parameters.

The estimates of the flow scales resolution expressed in Kolmogorov microscale or viscous scales units are shown in Table 3.

Dimension	Resolution in Kolmogorov scales
Wire length	$\eta_w = 5$
Separation of sub-modules in normal direction	$\eta_{\Delta x1} = 6$
Separation of sub-modules in spanwise direction	$\eta_{\Delta x2} = 8$

Table 3: Spatial resolution estimates in incompressible boundary layer experiment

The performance characteristics of the present probe is demonstrated in figure 4 where the shear stress  $-\rho u_1 u_2$  across the boundary layer, normalized by the wall mean shear  $\rho u_\tau^2$ , is plotted against the distance from the wall normalized by the boundary layer thickness  $\delta$ ,  $x_2/\delta$ . Among all the turbulent stresses, shear stress is the most challenging quantity to measure accurately. The reason is that this quantity is sensitive to small changes in probe alignment and experimental conditions which can increase substantially the uncertainty of the measurements. The data presented in figure 4 are the averaged data obtained at the centroid of the probe. The present data are compared with the measurements of HA, the data of Balint et al. (1991) and the data of Klebanoff (1954) as well as with the Direct Numerical Simulation results of Spalart (1988). The present data seems to agree well in the logarithmic and outer ( $x_2/\delta > 0.05$ ) region of the boundary layer when compared with previous data.

Figure 5 shows the distribution of the mean velocity gradient  $\overline{(\partial U_1 / \partial x_2)}$  across the boundary layer as measured at the centroid of the probe by time-averaging its instantaneous values. On the same figure 5 the mean velocity derivative in the logarithmic law region,  $1/\kappa x_2^+$ , where  $\kappa$  is von Kármán's constant, is also plotted for comparison. It appears that the measured mean velocity gradient data are in very good agreement with those obtained from the log-law. The present data are also in good agreement with the data of Honkan and Andreopoulos (1997) (not shown here) which were obtained in the same facility at  $Re_\theta = 2790$  which is considerably lower than the present one.

A comparison of the r.m.s. of fluctuations of the three vorticity components across the boundary layer measured by the present probe with data obtained by other investigators is shown in figure 6a, 6b, and 6c. These data are scaled with the boundary layer thickness  $\delta$  and friction velocity  $u_\tau$ . The values are compared with the DNS results of Spalart (1988) and the experimental results of Honkan and Andreopoulos (1997), Balint et al. (1991) and Lemonis (1995), for the three vorticity components. Additionally the measurements of Klewicki (1989) are also indicated on the plots for the spanwise component.

The present data for  $\omega_1$  are very close to the data of Honkan and Andreopoulos (1997) and those of Balint et al. (1991). These three experimental data sets as a group have values considerably greater than the DNS results of Spalart (1988).

The present values of the r.m.s. of the normal vorticity component  $\omega_2$  agree rather well with the data of Balint et al. and they are substantially lower than the data of Honkan and Andreopoulos in the outer part of the boundary layer

$x_2/\delta > 0.1$  which agree with the measurements of Lemonis (1995). The fluctuations of the dominant component of vorticity  $\omega_3$  as measured by the present probe compare well with the data of Balint et al.

It should be noted that there is a substantial difference in  $Re_\theta$  among all data sets under consideration. The present data and the data of Lemonis which correspond to  $Re_\theta = 5,300$  and  $Re_\theta = 6,500$  respectively represent the higher Reynolds number data under comparison while the DNS data of Spalart with  $Re_\theta = 1,410$  represent the lower  $Re_\theta$  data. Several of the differences among the data sets can be attributed to  $Re_\theta$  effects although it is not known how an increasing  $Re_\theta$  will affect vorticity fluctuations and their averages. It may be expected for instance, that the r.m.s. of vorticity fluctuations will decrease in the outer layer of the boundary layer as  $Re_\theta$  increases. Evidence to support this argument can be found in the r.m.s. values of wall vorticity flux shown in HA, which have one of the strongest ever observed Reynolds number dependence of any quantity involving vorticity: for a factor of 3 increase of  $Re_\theta$  a decrease by a factor 5 in the r.m.s. of wall vorticity flux has been observed. This evidence points to the direction that the r.m.s. of  $\omega_1$ ,  $\omega_2$  and  $\omega_3$  are expected to decrease with increasing  $Re_\theta$ . In fact the present data, if one limits the comparison with the HA data only, clearly support this conclusion. This comparison is more meaningful because both data sets were obtained in the same wind tunnel facility by almost identical techniques and procedures. Thus, it is very plausible to expect that the present data should be lower than the data of HA because of  $Re_\theta$  effects.

The conclusion of the qualification tests of the newly designed vorticity probe is that the probe performed very well in the measurements of mean and fluctuating vorticity in turbulent boundary layers as well as in the measurements of shear and normal stresses. Comparison of the data with previous measurements was very satisfactory. This provided considerable confidence in the use of the probe in weakly compressible, grid generated turbulence.

## 5. Isotropic decay relations

Three characteristic regions can be found in the flow behind a grid. First is the developing region close to the grid where rod wakes are merging and production of turbulent kinetic energy takes place. This region is followed by one where the flow is nearly homogeneous and isotropic but where appreciable energy transfer from one wave number to another occurs. This region is best described by the power law decay of velocity fluctuations

$$\frac{\overline{u^2}}{U^2} = A \left[ \frac{x}{M} - \left( \frac{x}{M} \right)_0 \right]^{-n} \quad (5.1)$$

where  $A$  is the decay coefficient,  $(x/M)_0$  is the virtual origin,  $n$  is the decay exponent.

The third region or final region of decay is the farthest downstream of the grid and is dominated by strong viscous effects acting directly on the large energy containing eddies.

Compressible homogeneous and isotropic turbulence has not yet been set-up experimentally and decay laws for this case have yet to be established. The turbulent or fluctuation Mach number  $M_t = q/\bar{c}$  with  $q = (u_i u_i)^{1/2}$ , seems to be the most appropriate parameter describing compressible turbulence. By extrapolating the validity of the previous law into compressible flows one can obtain the power law decay

$$M_t^2 = B \left[ \frac{x}{M} - \left( \frac{x}{M} \right)_0 \right]^{-n} \quad (5.2)$$

here  $B = 3A M_{\text{flow}}^2$  and  $B$ ,  $(x/M)_0$  and  $n$  depend on the grid size, mesh Reynolds number ( $Re_M$ ) as well as the mean flow Mach number  $M_{\text{flow}}$  which simply comprise the initial conditions.

## 6. Dissipation rate of turbulent kinetic energy

The transport equation for the instantaneous kinetic energy  $\frac{1}{2} U_i U_i$  in compressible flows is

$$\rho \frac{D \left( \frac{1}{2} U_i U_i \right)}{Dt} = -U_i \frac{\partial p}{\partial x_i} + U_i \frac{\partial \tau_{ij}}{\partial x_j} \quad (6.1)$$

where  $\tau_{ij}$  is the stress tensor  $\tau_{ij} = 2\mu S_{ij} + \lambda \delta_{ij} S_{kk}$  which is related to the bulk viscosity  $\mu_b$  through  $\lambda = \mu_b - 2/3\mu$ .

and where  $\lambda$  is the second coefficient of viscosity

The above equation can be manipulated to yield

$$\rho \frac{D \left( \frac{1}{2} U_i U_i \right)}{Dt} = \frac{\partial (-p U_j + \tau_{ij} U_j)}{\partial x_i} + p S_{kk} - \tau_{ij} S_{ij} \quad (6.2)$$



where the last term on the right hand side contains the dissipation rate of kinetic energy,  $E$ , converted into thermal/internal energy. The term  $p S_{kk}$  represents the work done by pressure forces during compression or expansion of the flow. Both terms, the dissipation rate  $E = \tau_{ij} S_{ij}$  and the pressure work term also appear with opposite sign in the transport equation for internal energy. While the dissipation rate is always positive at any given point in space and time, the pressure-dilatation term can, in principle, be positive or negative.

The dissipation rate is given by

$$E = \tau_{ij} \frac{\partial U_i}{\partial x_j} = \tau_{ij} S_{ij} = 2\mu S_{ij} S_{ij} + \lambda \frac{\partial U_k}{\partial x_k} \delta_{ij} \frac{\partial U_i}{\partial x_j} \quad (6.3)$$

After invoking Stokes hypothesis which suggests that the bulk viscosity is negligible,  $\mu_b \approx 0$ , the above equation becomes

$$E = 2\mu S_{ij} S_{ij} - \frac{2}{3}\mu \frac{\partial U_k}{\partial x_k} \frac{\partial U_m}{\partial x_m} \quad (6.4)$$

The second term in the right hand side of the above relation represents the additional contribution of compressibility to the dissipation rate of kinetic energy. This term disappears in the cases of incompressible flows. Since  $\partial U_k / \partial x_k \partial U_m / \partial x_m = (\partial U_k / \partial x_k)^2$  this term is always positive, the negative sign of this term in 6.4 may erroneously suggest that compressibility reduces dissipation. This is incorrect because the term  $S_{ij} S_{ij}$  also contains contributions from dilatation effects which can be revealed if one considers that

$$S_{ij} S_{ij} = \frac{1}{2} \Omega_k \Omega_k + \frac{\partial U_i}{\partial x_j} \frac{\partial U_j}{\partial x_i} \quad (6.5)$$

where  $\Omega_k \Omega_k$  is the enstrophy rate. The second term in the right hand side represents the inhomogeneous contribution in the case of incompressible flows. In the case of compressible flows, terms related to dilatation can be extracted through

$$\left( \frac{\partial U_i}{\partial x_j} \frac{\partial U_j}{\partial x_i} \right) = \left( \frac{\partial U_k}{\partial x_k} \right) \left( \frac{\partial U_m}{\partial x_m} \right) + \left[ \left( \frac{\partial U_i}{\partial x_j} \frac{\partial U_j}{\partial x_i} \right) - \left( \frac{\partial U_k}{\partial x_k} \right) \left( \frac{\partial U_m}{\partial x_m} \right) \right] \quad (6.6)$$

Then, the dissipation rate becomes

$$E = \mu \Omega_k \Omega_k + \frac{4}{3}\mu \frac{\partial U_k}{\partial x_k} \frac{\partial U_m}{\partial x_m} + 2\mu \left[ \frac{\partial U_i}{\partial x_j} \frac{\partial U_j}{\partial x_i} - \frac{\partial U_k}{\partial x_k} \frac{\partial U_m}{\partial x_m} \right]$$

$$E = \mu \Omega_k \Omega_k + \frac{4}{3}\mu S_{kk}^2 + 2\mu \left[ \frac{\partial U_i}{\partial x_j} \frac{\partial U_j}{\partial x_i} - S_{kk}^2 \right] \quad (6.7)$$

or

The second term on the right hand side describes the direct effects of compressibility i.e. dilatation on the

dissipation rate. It is obviously zero in the case of incompressible flows.

The first two terms on the right hand side of the last relation are quadratic with positive coefficients and positive signs and they are, therefore, always positive. The last term on the right hand side indicates the contributions to the dissipation rate by the purely non-homogeneous part of the flow. Its time-averaged contribution disappears in homogeneous flows like the present one. This term, in principle, can obtain negative values and thus it can reduce the dissipation rate. This does not violate the second thermodynamic law as long as the total dissipation remains positive at any point in space and time. It should be noted that the dissipation term appears as a source term in the transport equation for entropy. In the present context we will try to evaluate the contribution of the first two terms to the total dissipation as it has been computed from our measurements.

It has been customary in the past, see for instance (Zeman, 1990) to decompose  $E$  into a solenoidal part  $E_s$ , which is the traditional incompressible dissipation and the dilatational part  $E_d$ . In this case

$$E = E_s + E_d \text{ with } E_s = \mu \Omega_k \Omega_k + 2\mu \left[ \frac{\partial U_i}{\partial x_j} \frac{\partial U_j}{\partial x_i} - S_{kk}^2 \right] \quad \text{and } E_d = 4/3 \mu S_{kk}^2$$

Since all the mean velocity gradients are zero in the present homogenous flow the above can be transformed into

$$E = \mu \omega_k \omega_k + \frac{4}{3} \mu s_{kk}^2 + 2\mu \left[ \frac{\partial u_i}{\partial x_j} \frac{\partial u_j}{\partial x_i} - s_{kk}^2 \right] \quad (6.8)$$

where the lower case letters represent the fluctuating part only.

It is also useful to consider the time-averaged turbulent kinetic energy transport equation. This is usually expressed in terms of the mass-weighted averages according to Favre (1965). In the present case, velocity fluctuations were decoupled from mass fluxes and therefore the transport equation for turbulent energy  $\frac{1}{2} u_i u_i$  will be used. However, reference to the mass-weighted averages will be given when the order of magnitude of various terms appearing in the equation is considered.

If  $V$  is the specific volume defined as  $V = 1/\rho$  then  $\frac{1}{V} \frac{DV}{Dt} = S_{kk}$  and equation (6.1) can be

transformed to yield the transport equation for  $\frac{1}{2} u_i u_i$  after considering that mean pressure and velocity gradients are zero in the present flow.

$$\begin{aligned} \overline{U_k} \frac{\partial (\overline{u_i u_i / 2})}{\partial x_k} = & \overline{u_i u_i s_{kk}} + \overline{p u_i \frac{\partial v}{\partial x_i}} - \overline{\frac{\partial v u_i p}{\partial x_i}} - \overline{\frac{\partial \overline{V} u_i p}{\partial x_i}} + \overline{v p s_{kk}} + \overline{V p s_{kk}} - \overline{\frac{\partial (u_i u_i u_k / 2)}{\partial x_k}} \\ & - \overline{u_i \tau_{ik} \frac{\partial v}{\partial x_k}} + \overline{\frac{\partial v u_i \tau_{ik}}{\partial x_k}} + \overline{\frac{\partial \overline{V} u_i \tau_{ik}}{\partial x_k}} - \overline{v \tau_{ij} s_{ij}} - \overline{V \tau_{ij} s_{ij}} \end{aligned} \quad (6.9)$$

In the present context lower case letter represent fluctuations about the mean which is denoted with an over bar. The first term on the right hand side represents production of turbulent kinetic energy by the fluctuating dilatation  $s_{kk}$  which, as found in our measurements is very small and it can be neglected. DNS results of Lee et al. (1993) indicated that all the pressure transport terms are negligible and they can be ignored. The turbulent transport term  $\partial u_i u_i u_k / \partial x_k$  and the viscous transport are also found to be negligible. The work of Lee et al. refers to mass-weighted quantities while the

present analysis uses the specific volume as an independent variable. However their conclusions can be extrapolated to the present context if one considers the relation between fluctuating density  $\rho'$  and fluctuating specific volume  $v$ :

$$v = \frac{-\rho' \bar{v} + \bar{v} \rho'}{\bar{\rho} + \rho'} \quad \bar{v} = \frac{1 - \bar{\rho} \bar{v}}{\bar{\rho}}$$

If the time-average product of the two fluctuations is small i.e.  $\bar{\rho}' \bar{v} \ll 1$  then  $\bar{v} = \frac{1}{\bar{\rho}}$  and

$$v \approx \frac{-\rho' \bar{v}}{\bar{\rho}} . \text{ These relations link the fluctuating and mean density with fluctuating and mean specific volume}$$

and therefore the conclusions of Lee et al. can be invoked to obtain

$$\bar{U}_k \frac{\partial \overline{(u_i u_i / 2)}}{\partial x_k} = \overline{p u_i \frac{\partial v}{\partial x_i}} + \overline{v p s_{kk}} + \bar{v} \overline{p s_{kk}} - \overline{u_i \tau_{ik} \frac{\partial v}{\partial x_k}} + \overline{v \tau_{ij} s_{ij}} - \bar{v} \overline{\tau_{ij} s_{ij}}$$

Terms containing the fluctuating specific volume  $v$  or its derivative are also expected to be small because they are of third order.

Therefore for the present case of homogeneous turbulence

$$\bar{U}_k \frac{\partial \overline{(u_i u_i / 2)}}{\partial x_k} \approx \bar{v} \overline{p s_{kk}} - \bar{v} \overline{\tau_{ij} s_{ij}} \quad (6.10a)$$

The pressure-dilatation term in the absence of shock waves can also be ignored and therefore

$$\bar{U}_k \frac{\partial \overline{q^2}}{\partial x_k} \approx - \bar{v} \overline{\tau_{ij} s_{ij}} \quad (6.10b)$$

where  $\epsilon = \bar{E} \bar{v}$  and  $\overline{q^2} = 1/2 \overline{u_i u_i}$ .

Thus measurement of the convection of  $q^2$  by the mean flow can provide a good estimate of the dissipative viscous term  $\epsilon$  and its length scale  $L_\epsilon$  through

$$-\bar{U} \frac{\partial \overline{q^2}}{\partial x} = \epsilon = \frac{(\overline{q^2})^{3/2}}{L_\epsilon} \quad (6.11)$$

Once the dissipation length scale is obtained then the dissipation rate  $\epsilon$  as well as the associated micro scales (length, time, velocity) can be calculated. The above equation can be transformed to the following relation by non dimensionalizing with the mesh size  $M$ :

$$-\frac{\varepsilon M}{U^3} = \frac{3}{2} \frac{\partial(\overline{u^2}/U^2)}{\partial(x/M)} = \frac{3}{2} \frac{(\overline{u^2})^2}{L_e} \left[ \frac{M}{U^3} \right] \quad (6.12)$$

From this equation (6.12) the decay rate can be calculated using the coefficients of the power law of equation (5.1). Substitution of (5.1) in equation (6.12) yields:

$$\varepsilon = \frac{3}{2} n A \left[ \frac{x}{M} - \left( \frac{x}{M} \right)_0 \right]^{(-n-1)} \left[ \frac{U^3}{M} \right] \quad (6.13)$$

where A is the decay coefficient,  $(x/M)_0$  is the virtual origin, n is the decay exponent, U is the mean flow velocity and M the mesh size.

## 7. Dissipation rates estimates

The complete time-averaged dissipation rate of turbulent kinetic energy is, for the present homogeneous and isotropic flow

$$\bar{E} = \mu \overline{\omega_k \omega_k} + \frac{4}{3} \mu \overline{s_{kk}^2}$$

Direct evaluation of  $E$  requires simultaneous, highly resolved measurements of nine velocity gradients at a given location of the flow field as has been described in the previous section. This has been attempted in several locations of the present flow field. Traditionally for truly isotropic turbulent flows with moderate or low Mach number fluctuations,

the above relation is considerably simplified to  $\epsilon = 15 \nu \overline{\left(\frac{\partial u}{\partial x}\right)^2}$  (Tennekes and Lumley, 1972). Thus in the present

case the dissipation rate  $\epsilon$  has been computed by five different methods:

1. From the decay rate of turbulent kinetic energy and the use of equations 6.12 or 6.13.
2. From frequency spectra of velocity fluctuations after invoking Taylor's hypothesis to compute the three dimensional wave number spectrum  $E(k)$ . The dissipation  $\epsilon$  can be computed from the integral

$$\epsilon \approx 2\nu \int_0^\infty k^2 E(k) dk \quad (7.1)$$

3. From estimates of  $\overline{(\partial u / \partial x)^2}$  and the isotropic relation  $\epsilon = 15 \nu \overline{(\partial u / \partial x)^2}$ . The quantity  $\overline{(\partial u / \partial x)^2}$  has been computed by differentiating in time the velocity fluctuation signal and invoking Taylor's hypothesis of frozen turbulence convection.

4. From estimates of Taylor's microscale  $\lambda$  obtained from autocorrelations of longitudinal velocity fluctuations. Then the rms of the fluctuations of the velocity gradient  $\overline{(\partial u / \partial x)^2}$  can be obtained independently from

$$\overline{(\partial u / \partial x)^2} = \overline{u^2} / \lambda^2 \quad \text{and therefore dissipation can be computed from} \quad \epsilon = 15 \nu \frac{\overline{u^2}}{\lambda^2}$$

5. By direct measurement of all time-dependent velocity gradients and computation of all the terms appearing in eq (6.8). This method can also provide an assessment of all the assumptions made in the previous methods of estimating  $\epsilon$ . The estimates usually obtained from these methods are not identical since the assumptions associated with and the uncertainties involved in each of them may differ considerably. The lack of adequate spatial resolution is one of the major source of errors and affects each estimate of  $\epsilon$  differently. However even in cases where the estimates of  $\epsilon$  differ

by 50% or more the estimates of  $L_\epsilon$  or Kolmogorov's viscous scale  $\eta = (\nu^3/\epsilon)^{1/4}$  differ only by 8.5% (see Andreopoulos and Honkan, 1996). In the present case the estimates of  $\epsilon$  obtained from the decay rate of  $q^2$  and those obtained from Taylor's microscale (autocorrelations) were the most reliable and very close to those obtained by the method #5. Based on these estimates of  $\epsilon$  the spatial resolution of probe used in the present investigation was between  $7\eta$  and  $26\eta$ , depending on the flow. If one considers that the spatial resolution usually achieved in measurements of compressible flows is of the order of  $10^3\eta$  (see Andreopoulos and Muck, 1987; Smits and Muck, 1987) then the present one appears to be very satisfactory even if it is compared to values usually achieved in low Reynolds number incompressible flows. In the case of vorticity measurements the spatial resolution was also in the range of  $7\eta$  to  $30\eta$ .

## 8. Flow homogeneity and isotropy

The flow visualization experiments and quantitative analysis of velocity and temperature obtained at different locations simultaneously across a section of the tube indicated that the flow is homogeneous within 85% of the diameter. A full documentation of the flow quality in the shock tube is provided by Briassulis et al. (1995).



The flow isotropy was verified directly and indirectly. Direct verification provided by computing the anisotropy tensor  $b_{ij}$  of the velocity field

$$b_{ij} = \frac{\overline{u_i u_j}}{\overline{u_i u_i}} - \frac{1}{3} \delta_{ij} \quad (8.1)$$

where  $u$  is velocity fluctuation about the mean and  $\delta$  is the Kronecker delta. Generally, grid generated turbulence tends to be anisotropic with the streamwise component slightly larger the cross-stream components. Compere-Bellot and Corrsin (1966) were able to generate turbulence very close to an isotropic state by introducing a contraction after the grid. However in most experiments where isotropic turbulence has been configured by using biplane grids all turbulent quantities have been found to agree reasonably well with isotropic conditions at sufficiently large distances from the grid, even with the presence of slight anisotropy which usually decreases with downstream distance from the grid.

The present data, shown in fig. 7, suggest a rather good degree of isotropy, with minor variations, well within established margins. For comparison it should be mentioned that for boundary layers  $b_{11}=0.45$  and  $b_{12}=0.15$ . Anisotropy of the present flow field is compared with one of the latest and most complete study in this matter that of Tsinober et al (1992) in incompressible flows. It appears the values of  $b_{ij}$  in the present experiment are confined within the band  $\pm 0.075$  in the region  $30 < x/M < 60$  and within the band of  $\pm 0.035$  in the region  $65 > x/M$ . It is also evident from figure 7 that the degree of flow isotropy achieved in the present flow configuration is slightly better than that of Tsinober et al. (1992). Both data sets show that anisotropy decrease with downstream distance.

The anisotropy of the vorticity field is also shown in fig.7. The anisotropy tensor for vorticity is defined similarly as

$$c_{ij} = \frac{\overline{\omega_i \omega_j}}{\overline{\omega_i \omega_i}} - \frac{1}{3} \delta_{ij} \quad (8.2)$$

Values of  $c_{ij}$  are compared with the data of Tsinober et al. (1992) which include vorticity measurements. Our present vorticity data indicate that the anisotropy of the flow is well within the established limits. The reasonably low values of the anisotropic tensors  $b_{ij}$  and  $c_{ij}$ , shown in figure 7, establish the isotropic nature of the present flow generated in the shock tube.

Indirect evidence of isotropy was provided by considering the skewness of velocity fluctuations and the skewness of velocity derivative (Tavoularis et al., 1978, Mohamed and LaRue, 1990).

Figure 8 presents the skewness of velocity fluctuations for three mean flow Mach numbers. It appears that  $S_u$  remains constant and close to zero for all measured downstream locations.

The skewness of velocity derivative  $S_{\partial u / \partial x}$  represents the average rate of production of mean square vorticity by vortex stretching (Batchelor, 1953) and it is related, according to Tavoularis et al. (1978), to the spectral energy transfer which depends on the turbulent Reynolds number,  $Re_\lambda$ . In the same work, Tavoularis et al. present a comprehensive study of values of the skewness of velocity derivative for a variety of flow fields and  $Re_\lambda$ . From this study, if one considers the data obtained from isotropic grid turbulence, it can be observed that  $S_{\partial u / \partial x}$  decreases with  $Re_\lambda$  for  $Re_\lambda > 5$ . The theoretical analysis of George (1992) also suggests that  $S_{\partial u / \partial x}$  varies as  $Re_\lambda^{-1}$ . Typical values for  $S_{\partial u / \partial x}$  are shown in figure 9a for three different flow cases of the present investigation together with values obtained by other researchers in various turbulent flow fields. The values obtained are between 0.2 and 0.4, a range which is lower than the  $S_{\partial u / \partial x}$  value at  $Re_\lambda \approx 5$ . Determination and calculation of the skewness of velocity derivative is described in detail in Briassulis (1996).

The self-preservation theory of George (1992) suggests that the value of the product  $S_{\partial u / \partial x} Re_\lambda$  depends on initial conditions and asymptotically should vary as  $Re_M^{1/2}$  as it has also been proposed by Batchelor and Townsend (1947). Figure 9b shows values of the ratio  $S_{\partial u / \partial x} Re_\lambda / Re_M^{1/2}$  plotted against  $Re_M$  for three different Mach number  $M_{flow}$  as they have computed from measured data obtained in the present investigation. The data show that this ratio maintains a

reasonably constant value which depends on  $M_{\text{flow}}$ . For the lowest  $M_{\text{flow}}=0.3$  this value appears to be 0.28 on average, while for  $M_{\text{flow}}=0.475$  this value increases to a new level of 0.32. The value of the constant reduces to 0.21 for  $M_{\text{flow}}=0.6$ . It should be noted that the data of Batchelor and Townsend show that the asymptotic value of this constant is 0.12. The apparent difference between the present data and those of Batchelor and Townsend may be due to the fact that all flow cases investigated in the present work can be considered as compressible. Thus compressibility may increase the value of this constant. The self-similarity theory of George (1992) has been developed for incompressible flows. It remains to be seen whether self-similarity is an attainable state of compressible turbulence. The fact that there is a constant value of the ratio  $S_{\partial u/\partial x} \text{Re}_\lambda / \text{Re}_M^{1/2}$  for each  $M_{\text{flow}}$  suggests that self-similarity theory may be extended to weakly compressible turbulence.

It can be therefore concluded from all the results presented in this section that direct and indirect evidence exists that support the argument that the present flow is nearly homogeneous and isotropic.

## 9. Decay of mach number fluctuations

The typical decay of turbulent kinetic energy data with  $x/M$  was fitted with the power law of equation (5.2). It should be noted that this relation which describes the decay rate of turbulence is based on entirely empirical grounds. In the early experiments of Simmons and Salter (1934) and Dryden (1943) the decay rate of turbulence was found to be inversely proportional to  $x-x_0$ . Subsequent experiments by Corrsin and co-workers indicated that the decay rate described by eq (5.1) provides a better fit to the experimental data with  $n$  in the range of 1.1 to 1.35.

In the present work, the variables  $A$ ,  $(x/M)_0$ , and  $n$  were determined so that the residual deviation from the original data to be minimized. This way all variables were determined concurrently under the condition of minimum deviation. In that respect this approach represents a departure from previous practices where only two of the three parameters were determined through a best fit procedure while the third one was fixed. Exceptions to this past practice is the work of Mohamed and LaRue (1990). A consequence of this approach is that  $n$  can reach any positive value and not only  $>1$  as usually is the case in previous works.

It should be emphasized that the validity of the empirical power-law decay does not necessarily imply isotropy. Thus the data used for the best fit procedure had not only to obey the power law but also to be in the region where nearly isotropy holds. This was achieved by considering the values of the anisotropy tensor typically shown in figure 7.

The present work documents the effects of the mesh size/mesh Reynolds number as well as the flow Mach number on the above mentioned variables  $A$ ,  $(x/M)_0$ , and  $n$ . The importance of these parameters is evident when one considers eq (6.13). Once these parameters are available the dissipation rate of turbulent kinetic energy  $\epsilon$ , the corresponding dissipative length scale  $L_\epsilon$  and Taylor's microscale  $\lambda$  can be computed.

Several grids were used in the present experiments so that the Reynolds number based on the mesh size  $\text{Re}_M$  as well as the dominant length scales present in the flow can be varied. The mesh Reynolds number ranged from 35,000 to 600,000 while the mesh size ranged from 3mm to 25mm. Measurements were obtained at three different driver pressures/shock strengths. The bulk parameters of all flow cases are shown in table 1. The Reynolds numbers achieved in the present investigation are one of the highest ever attempted in laboratory configurations of nearly homogeneous and nearly isotropic turbulence.

Figure 10 demonstrates the power law decay behavior of all the measured data as it is described by equation (5.2). The results of nine experiments are plotted in logarithmic scales in this figure. They include 3 different grids at three different pressures/mean flow Mach numbers which are in the subsonic range of  $0.3 \leq M_{\text{flow}} \leq 0.6$  placing the flows in the weakly to moderately compressible regime.

Several conclusions can be drawn from their data. First the data shown in this log-log plot indicate that Mach number fluctuations  $M_t$  decay with downstream distance  $x/M$  according to the proposed power law

$$M_t^2 = B \left[ \frac{x}{M} - \left( \frac{x}{M} \right)_0 \right]^n \quad (9.1)$$

Second, the exponent  $n$  and the constant  $B$  depend on the grid, Mach number or  $\text{Re}_M$ . Third, the region where isotropy starts, depends more on the grid and its solidity than on the flow Mach number or  $\text{Re}_M$ . It also appears that  $M_t$  increases

with increasing Mach number of the flow  $M_{flow}$  in all experiments with same grid. This behavior is more evident in downstream positions with  $x/M > 30$ .

The effect of  $Re_M$  or  $M$ , hereafter mentioned as  $Re_M/M$ , on the coefficient  $B$  for three different Mach numbers is shown in figure 11a. It should be mentioned that the coefficient  $B$  shown above is related to the coefficient  $A$  of the velocity fluctuations power law decay through the relation  $B=3AM_{flow}^2$  which clearly suggests that  $B$  depends on  $M_{flow}^2$ . In addition to this rather obvious dependence of  $B$  on  $M_{flow}$ , there is the yet unknown Mach number dependence of  $A$ . This is shown in figure 11b where the effects of  $Re_M/M$  on the coefficient  $A$  for three different Mach numbers is demonstrated. Reynolds number variation was produced by changing the mesh size under a constant velocity i.e. Mach number  $M_{flow}$ .

For the lowest tested velocity flow field ( $U \approx 120$  m/sec), which corresponds to a mean flow Mach number of 0.35, the decay coefficient  $A$  or  $B$  increases in a non-linear fashion with increasing mesh size  $M/Re_M$  as shown in figure 11. As the Mach number increases,  $B$  is substantially decreased from the values of the previous case and furthermore it appears to be independent of mesh size. The same holds for the highest tested Mach number, where the decay coefficient is further suppressed. It can be concluded that the decay coefficient  $A$  or  $B$  decreases when the flow Mach number increases and that it is independent of the mesh size  $M$  and  $M_{flow}$  at high  $M_{flow}$ .

The virtual origin  $(x/M)_0$  strongly depends on the mesh size/ $Re_M$ . This is shown in figures 12 where the position of the virtual origin is plotted against  $Re_M$  for a constant Mach number flow with  $M_{flow}=0.6$ . For all cases it was observed that the virtual origin approaches the grid as the mesh size/ $Re_M$  increases as shown in figure 13, where the results for the three Mach number are plotted together for comparison. This behavior is most probably due to increased mixing which is associated with increasing  $Re_M$ .

The effects of the Mach number at a particular  $Re_M$  can also be seen in figure 13. The virtual origin is strongly affected at the highest Mach number only, while for the medium and low  $M_{flow}$  cases it is moderately affected. At the highest Mach number where the associated compressibility effects expect to play a bigger role, the virtual origin moved further away from the grid at a given  $Re_M$ . It is also interesting to observe, in the same figure, that the above mentioned effect is diminished for the largest mesh size grid. Namely the virtual origin at high  $Re_M$  appears to reach the same value of about 5 mesh sizes for each of the investigated Mach numbers.

The decay exponent  $n$ , shown in figure 14, is substantially affected by the Mach number of the flow field. It is clear from the above figure that  $n$  is decreasing with increasing Mach number. The effect of the mesh size on the decay exponent can also be observed. It behaves similarly to the decay coefficient  $A$ . Namely for the lowest Mach number it increases with increasing mesh size/ $Re_M$ . That means that for finer grids, i.e. of small mesh size, there exists larger decay rates than for coarser grids. At a first glance the above statement appears to contradict previous notions based on fixed  $n$  fitting of the data, but if we consider equation (6.13) then the dissipation rate  $\epsilon$  is proportional to  $nA[(x/M)-(x/M)_0]^{-(n+1)}$ . Thus  $\epsilon$  will increase if  $n$  decreases.

When the Mach number increases the decay exponent  $n$  decreases substantially. From a value of 0.8 at  $M_{flow}=0.3$ , for instance,  $n$  drops to 0.3 at  $M_{flow}=0.6$  in the case of  $Re_M=200,000$ . This is a reduction of the decay of more than 60% for a 100% increase in Mach number. Thus, it appears that the major effect of compressibility is a substantial reduction in the decay rate. The second interesting behavior of the exponent  $n$  is that at high  $M_{flow}$  it remains almost independent of  $Re_M$  where it reaches a value of about 0.3.

A typical decay of velocity fluctuations, as fitted by the power law, for the 5.08 mm mesh size grid is shown in figure 15. The velocity fluctuations are higher at higher Mach numbers which also correspond to higher  $Re_M$ . The effect of higher velocity fluctuations can not simply be attributed to the increase of the mean Mach number and the associated compressibility effects of the flow but also to the increase of  $Re_M$ . Although Mach number and Reynolds number are two different independent variables they may cause quite similar effects on the flow which may be difficult and some times impossible to distinguish clearly from each other. A 4-fold increase in pressure, for instance, which corresponds to 100% change in Mach number and Reynolds number, results in a 3 fold increase in the Mach number fluctuations  $M_v$  throughout the entire flowfield. Most probably this increase in  $M_v$  and  $(u/U)^2$  can be attributed to both parameters, i.e.  $M_{flow}$  and  $Re_M$ .

## 10. Dissipation rate and length scales

Figure 16a shows the dissipation rate of kinetic energy  $\epsilon$  for one grid (5x5) with mesh size  $M=5.08$  mm at different flow Mach numbers. Two dissipation datasets are shown in this figure which have been computed by two

different methods. In the first method,  $\epsilon$  has been determined from the decay rate of turbulent kinetic energy by using equation (6.13). The second set of dissipation data has been computed from the dissipation spectra calculated through the relation (7.1). The two datasets agree reasonably well with each other particularly in the far field.

From the data shown in figure 16a, it appears that  $\epsilon$  increases with increasing Mach number in all investigated flows with the  $M=5.08$  mm mesh size grid. This behavior is quite similar to that of the decay of  $q^2$ . Dissipation varies proportionally to  $x^{-n-1}$  while  $q^2$  varies as  $x^{-n}$ . It remains to be seen whether this effect is a Mach number effect or it is due to Reynolds number increase.

The data shown in figure 16a are non-dimensionalized by  $M/U_1^3$  and replotted in figure 16b where the same behavior can be observed: non-dimensional dissipation increases with flow mach number  $M_{flow}$ . However, in the case of coarser grids non-dimensional dissipation  $\epsilon M/U_1^3$  is decreased with increased  $M_{flow}$ . Figure 16c shows values of the non-dimensional dissipation for the case of the 2x2 grid with mesh size  $M=12.7$  mm. These data demonstrate that dissipation is reduced when the flow Mach number increases in the case of coarse grids. As will be seen later direct measurements of dissipation also confirm this conclusion.

The difference between coarse and fine grids in the behavior of how the dissipation  $\epsilon M/U_1^3$  varies with  $M_{flow}$  can be attributed to the effects of  $Re_M$  in addition to the obvious reason of grid dependence. It should be noted that in the case of the fine grid with  $M=5.08$  mm  $Re_M$  reaches values from 59,000 to 102,000 while in the case of the coarser grid with  $M=12.7$  mm  $Re_M$  reaches values from 137,000 to 260,000.

The dissipation rate of kinetic energy  $\epsilon$  for various mesh sizes is shown in figure 17 for the highest tested Mach number case. In this figure the effects of  $Re_M/M$  at a fixed flow Mach number,  $M_{flow}$  can be depicted. The data in figure 17 suggest that coarser grids, i.e. higher  $Re_M$  produce lower dissipation rates,  $\epsilon$ , at constant  $M_{flow}$  when compressibility effects are high. In the absence of large compressibility effects, which are typical in the lowest tested Mach number flowfields, the reverse influence of the mesh size on  $\epsilon$  can be found as shown in figure 18. In this figure, dissipation data non-dimensionalized by the mean velocity and mesh size for the lowest Mach number tested flowfield of  $M_{flow}=0.35$  is plotted for various mesh sizes. The reverse trend is observed for  $\epsilon M/U^3$  in the absence of strong compressibility effects. In this case, the coarser grid with the largest mesh size and highest  $Re_M$  shows the largest non dimensionalized dissipation rate of kinetic energy. Since the mean flowfield velocity  $U$  is equal for all plotted cases the effect presented in this figure is mainly due to the Mesh size  $M$  and  $Re_M$ .

Figure 18 also shows the dissipation rate data obtained with the vorticity probe. In this case the total dissipation rate was computed directly from the measured time-dependent velocity and density gradients. These data appear to be 5% to 15% higher than the data obtained from the decay rate of turbulent kinetic energy. This difference is well within the experimental uncertainty associated with the measurements of dissipation.

The data shown in figure 17 are non dimensionalized with  $M/U^3$  and replotted in figure 19. The effect of compressibility is rather striking at this  $M_{flow}=0.6$  and the results consistently indicate that  $\epsilon M/U^3$  increases with decreasing mesh size/  $Re_M$ .

Even in the case of the medium tested Mach number flowfield compressibility effects can be observed in the dissipation data shown in figure 20. These data also demonstrate that the coarser grids with the greater mesh sizes and higher  $Re_M$  flowfield produce a lower dissipation rate  $\epsilon$ . The dissipation rate of kinetic energy for the medium tested Mach number follows the trend that exists for the highest tested Mach number and therefore suggests that the presence of compressibility effects are felt in this flowfield too. The quantitative difference of the degree of compressibility effects between  $M_{flow}=0.6$  and  $M_{flow}=0.475$  flowfields can be estimated upon closer observation of the data shown in figures 17 and 20. For almost a 4-fold increase in the mesh size and  $Re_M$  the dissipation rate decreased 10 times for  $M_{flow}=0.6$  and approximately 5 times for the  $M_{flow}=0.475$  flowfield. This behavior also suggests that, as expected, higher Mach number flowfields introduce higher compressibility effects.

The result of single measurement of total dissipation obtained with the multi-wire vorticity probe is also plotted in figure 20. The measurements were obtained in the flow with the  $M=12.7$  mm mesh size grid and with  $M_{flow}=0.425$  which is lower than the flow Mach number of the rest of the data. This value of dissipation rate is also slightly higher than the values obtained from the decay rate of turbulent kinetic energy.

The present measurements indicate that dissipation rate in addition to the particular grid used to generate the flow and the Reynolds number  $Re_M$ , depends also on the flow Mach number  $M_{flow}$ .

The dissipative length scale  $L_\epsilon$  indicates how fast the advected turbulent kinetic energy  $q^2$  at a given location, is dissipated into heat. It is a longitudinal length scale since advection of  $q^2$  in the present flow takes place only in the

longitudinal direction. As Mach number increases the results of the present investigation show that the dissipative length scale  $L_\epsilon$  increases although the dissipation rate of turbulent kinetic energy,  $\epsilon$ , also increases for a given mesh size (see fig.16). This increase in  $L_\epsilon$  is attributed to the increase in  $q^2$  with Mach number which apparently is larger than the corresponding increase of  $\epsilon$ .

A typical result is shown in figure 21. These data correspond to the three flowfields with different Mach numbers and are obtained with the same grid of mesh size  $M=12.7\text{mm}$ . It is interesting to observe that for the highest mean flow Mach number the dissipation length scale grows faster than and reaches values much greater than the medium Mach number flow case. This behavior can be attributed to higher compressibility and higher  $Re_M$  effects which can cause such a drastic increase. In the case of fine grids (not shown here), however, the trend observed is reversed: the dissipation length  $L_\epsilon$  decreases with increasing  $M_{\text{flow}}$ . For both grids i.e. the  $5 \times 5$  and the  $4 \times 4$  with  $M=5.08\text{ mm}$  and  $M=6.35\text{ mm}$  respectively  $L_\epsilon$  decreases with  $M_{\text{flow}}$ . The data indicate a fast dissipation process in flows produced by fine grids.

The effect of the grid's mesh size on the dissipation length scale is shown in figure 22. The dissipation length scale  $L_\epsilon$  increases with increasing mesh size and  $Re_M$ . From this figure it can be seen that for the same mean Mach number a 5-fold or more increase in  $L_\epsilon$  occurs for a 3-fold increase in the mesh size/ $Re_M$ . Thus the pivotal effect that the grid size exerts on the length scales in the flowfield is that coarser grids result in longer  $L_\epsilon$ . It is also apparent from both previous figures that the dissipation length scale strongly depends on  $x/M$  and that it increases with downstream distance.

The data presented in figure 21 for the highest Mach number flowfield shows large values of  $L_\epsilon$  which are indicative of a very slow dissipation process. These values exceed the shock tube diameter  $D=0.305\text{ m}$  at distances  $x/M > 130$  and about  $x/M=200$  reach values of  $L_\epsilon=0.5\text{ m}=1.63\text{ D}$ . In general, it is expected that at large distances from the grid the growth of eddies due to amalgamation will be affected by the cross-sectional size of the facility which in the present case is described by the diameter  $D$ . This requires that at any point in the flow the *lateral* length scale  $L_{22}$  should be smaller than  $D$ . Since  $L_{22}$  is related to the mesh size of the grid  $M$  the above requirement introduces for consideration the parameter  $D/M$  which has to be reasonably high in order to avoid these wall effects on the flow development. In this context, however,  $L_\epsilon$  represents a *longitudinal* length scale which characterizes the dissipative motions which are mostly taking place at the level of small scales eddies which are isotropic although, indirectly, they may be affected by the motion of the large eddies. Thus no direct effect of  $D$  is expected on  $L_\epsilon$  and therefore  $L_\epsilon$  can reach values of the order of  $D$ .

In order to estimate the length scales in the longitudinal  $\xi_1$  direction and normal  $\xi_2$  direction the cross correlation coefficients

$$r_{ij}(\xi_k) = \frac{\overline{u_i(x)u_j(x+\xi_k)}}{\sqrt{\overline{u_i^2(x)}}\sqrt{\overline{u_j^2(x+\xi_k)}}}$$

were evaluated by two point measurement in the  $\xi_2$  direction and from auto-correlations in the  $\xi_1$  direction after invoking Taylor's hypothesis.

Figure 23 shows the  $L_{11}(\xi_1)$  scale in the longitudinal direction for the three different flow cases. There exists some scatter in the data in each particular case which is attributed to the various grids used. No attempt has been made to present any  $Re_M$  effects since no clear trend or pattern among the data obtained could be identified. From the data of figure 23, it can be seen that the integral length scale increases with downstream non-dimensional distance  $x/M$  for all investigated cases. It is also evident that  $L_{11}$  in the case of  $M_{\text{flow}}=0.475$  is higher than in the case of  $M_{\text{flow}}=0.36$ . However when the flow Mach number increases to  $M_{\text{flow}}=0.6$  and therefore stronger compressibility effects are present, then the values of the integral length scale drop.

The two point correlation  $r_{11}(\xi_2)$  in the lateral direction  $\xi_2$  of the longitudinal velocity fluctuations is shown in figure 24. These data were obtained by a specially designed cross correlation probe consisting of six parallel wires and three temperature wires separated from each other by  $1\text{ mm}$ . Not all the curves cross the zero line and therefore it is very difficult to integrate them in order to obtain the classically defined length scale in the lateral direction. However the slopes of these curves are indicative of their trend. It is rather obvious that the length scales are reduced with increasing flow Mach number. This behavior is very similar to that of  $L_{11}(\xi_1)$ .



The effect of Mach number on Taylor's microscale computed from  $\epsilon = 15\nu \left( \frac{\partial u}{\partial x} \right)^2 = 15\nu \frac{u'^2}{\lambda^2}$  is shown in

figure 25 for three different Mach numbers and for one grid with mesh size 12.7 mm. Taylor's microscale appears to increase with increasing Mach number. Increase of the Taylor's microscale is also observed in flowfields produced by coarser grids. This is shown in figure 26 where the data of four different grids are plotted for the same flow Mach number. It is clear that the coarser the grid, larger mesh size, the greater the Taylor's microscale. The dependence (increase) with increasing  $x/M$  is evident, as shown earlier for the dissipation length scale, is also shown for the Taylor's microscale. However, in the case of the grid with  $M=5.08$  mm, which is considered as fine grid,  $\lambda$  appears to decrease with  $M_{flow}$  (not shown here). This difference in the behavior between the coarse and fine grids is a direct outcome of a similar behavior in the dissipation distribution which was discussed earlier in reference to dissipation data shown in figures 16b and 16c.

The effect of the flow Mach number on the viscous scales has been investigated next. The data for three different Mach numbers are shown in figure 27 for the case of the 5x5 grid with mesh size 5.08 mm. They all increase with downstream distance. The results also show that as the Mach number increases, the Kolmogorov's length scale,  $\eta$  decreases. This viscous scale appears to increase with increasing  $M_{flow}$  even in the case of coarse grids.

The effect of mesh size/ $Re_M$  on  $\eta$  is shown in figure 28 where the data are plotted for four different mesh sizes and for a decaying flowfield at a constant mean Mach number of 0.6. Similar results are obtained for the rest of the tested flowfields. It appears that  $\eta$  increases with increasing  $M/Re_M$ , a behavior which is similar to that of  $\lambda$  or  $L_e$ .

The last two figures (27 and 28) demonstrate the effects of compressibility on the viscous scales. In particular, compressibility effects appear to suppress their size. This behavior imposes a severe requirement for spatial resolution at high Mach number turbulent flows. The present measurements indicate values of  $\eta$  ranging from 0.015 to 0.06 mm. The size of the probes expressed in terms of Kolmogorov's length scales appears to be  $\eta_w = l_w/\eta = 13$  for the greatest scales and 52 for the smallest scales. The scales at error start at about half of these values, 7 and 26 respectively. Based on these values, which determine the upper limit of the valid part of the spectrum, estimates of the power spectral density of the spatially filtered scales have been obtained from Wyngaard's (1969) work for subsonic flows. It appears that the spatially filtered scales amount for about 15% of the total spectral density of velocity fluctuations for measurements close to the grid where  $\eta$  is small and less than 4% for measurements where  $\eta$  is larger. The high resolution of the hot wire probes allows us to conclude that the results obtained in regard to the compressibility effects on the viscous scales are not biased. In addition the estimates of dissipation obtained from the decay rate of  $q^2$  seem to be much less affected by the effects of inadequate spatial resolution than those obtained from spectra. One reason to explain this immunity of  $\epsilon$  to spatial resolution errors is a possible cancellation of uncertainties in the measurements of  $q^2$  when the longitudinal gradient  $\partial q^2/\partial x$  is computed. Thus the uncertainty in the estimates of  $\eta$  may be considerably lower than the 4% to 15% range quoted above.

In summary, the results of the present investigation indicated that, dissipation rate, dissipation length scale and Taylor's microscale are strongly affected by the flow mach number  $M_{flow}$ . In flows produced by fine grids dissipation increases with increasing  $M_{flow}$  while  $L_e$  and  $\lambda$  are reduced. In the case of flows generated by coarse grids, dissipation decreases with increasing  $M_{flow}$  and  $L_e$  and  $\lambda$  increase with  $M_{flow}$ . Lateral integral length scales and viscous length scales are reduced with increasing  $M_{flow}$ . This work also demonstrated that at high Mach numbers flows, all length scales i.e.  $L_e$ ,  $\lambda$  and  $\eta$  increase with increasing mesh size or  $Re_M$ .

## 11. Vorticity and enstrophy

Four additional experiments were carried out with the new multi-wire vorticity probe. Table 4 shows the bulk flow parameters of the experiments which were performed at two different flow Mach numbers and with two different grids.

No	Grid	x/M	$M_{flow}$	$U_1$ (m/s)	$\rho$ (kg/m <sup>3</sup> )	P (KPa)
1	2x2	48	0.308	121	1.59	155
2	2x2	48	0.388	151	1.74	174
3	3x3	72	0.362	139	1.7	170
4	3x3	72	0.425	161	1.84	188

Table 4: Bulk flow parameters in vorticity measurements

Figures 29 and 30 show the power spectral density of the turbulent kinetic energy  $\frac{1}{2} u_i u_i$  and enstrophy  $\frac{1}{2} \omega_i \omega_i$  weighted by the wavenumber  $k_i = 2\pi/\lambda$  as measured in the present investigation for the case of the 2x2 grid. The streamwise wavenumber  $k_1 = 2\pi f/U_1$  was computed by assuming the local longitudinal mean velocity as the convection velocity (Taylor's hypothesis). Wavenumbers have been non-dimensionalized by the mesh size  $M$ . In the case of  $M_{flow} = 0.308$  which is shown in figure 29, the maximum value of the spectral density of turbulent kinetic energy occurs at approximately  $k_1 M = 4.5$  while the maximum value of the spectral density of enstrophy occurs at about  $k_1 M = 7$ . This difference in the maxima of spectral energies indicates a shift towards higher wavenumbers of enstrophy fluctuations which suggests that they are mainly a result of a greater proportion of contributions by the smaller scales whereas the kinetic energy comes from relatively larger eddies.

In the case of  $M_{flow} = 0.388$ , shown in figure 30, the maximum energy of T.K.E. is found to occur at about the same wavenumber as in the case of  $M_{flow} = 0.308$  i.e. at  $k_1 M = 4.5$ , while the maximum energy of enstrophy occurs at a lower wavenumber  $k_1 M = 5.8$ . Once more, the data show that there is a shift towards higher wavenumbers in the case of enstrophy maxima. However, it appears that increasing  $M_{flow}$  reduces the difference between the wavenumbers where the maxima of kinetic energy and enstrophy occur. If one considers that the peak in T.K.E. represents the size of large energy containing eddies and that the peak in enstrophy represents mostly small energy dissipating eddies then it would be expected that this difference or shift increases with increasing Reynolds number. The fact that this shifts decreases with Mach number in the present case indicates that the effect of  $M_{flow}$  in reducing this difference becomes stronger than the effect of Reynolds in increasing it.

Similar observations can be made in the case of the 3x3 grid and the two experiments carried out with this grid. Figure 31 and figure 32 show the spectral densities of TKE and enstrophy for the  $M_{flow} = 0.362$  and  $M_{flow} = 0.425$  cases respectively. The maximum spectral density of TKE occurs at about  $k_1 M = 2$  in both flows. However, the maximum spectral density of enstrophy occurs at  $k_1 M = 5.6$  in the case of  $M_{flow} = 0.362$  and at  $k_1 M = 3.8$  in the case of  $M_{flow} = 0.425$ . Thus the initial wavenumber difference of 3.6 observed in the lower Mach number case is being reduced by about 50% in the case of  $M_{flow} = 0.425$ .

Figure 33a shows a semi-logarithmic plot of the probability density function (pdf) of the three vorticity components for the case of  $M = 12.7$  mm and  $M_{flow} = 0.308$ . The quantity  $M/U_1$  has been used to non-dimensionalize vorticity. The data shows that the pdfs of the vorticity components overlap substantially as it is expected to occur under isotropic conditions. The present data also indicate that these pdfs have a Gaussian distribution. As the flow Mach number increases to  $M_{flow} = 0.388$  the pdfs of vorticity start to deviate from the Gaussian distribution (see fig. 33b). The data show that the three pdfs reasonably collapse on each other indicating a good degree of isotropy. However the probability of higher amplitudes which are characterized by the tails of the distributions are lower than the probability

predicted by the Gaussian distribution. This is the first evidence to that compressibility starts to affect the high amplitude events of vorticity first.

Similar behavior can be identified in the pdfs of vorticity components for the case of  $M=8.47$  mm. These pdfs are plotted in figures 34a and 34b for the flow cases with  $M_{\text{flow}}=0.362$  and  $M_{\text{flow}}=0.462$  respectively. Both figures indicate a good degree of isotropy of the vorticity field. In the higher  $M_{\text{flow}}$  case, as in the case with the  $M=12.7$  mm grid, the tails of the distributions start to deviate from the Gaussian distribution, indicating a possible effect of compressibility.

The pdfs of the enstrophy  $\omega_k \omega_k$  for the two cases of experiments with the two different grids,  $M=12.7$  mm (2x2) and  $M=8.46$  mm (3x3), are shown in figure 35. Enstrophy values have been non-dimensionalized by  $(M/U_1)^2$ . Enstrophy is a very significant quantity in fluid dynamics. It is not only related to the solenoidal dissipation as was mentioned in section 6, but also to the invariants of the strain-of-rate matrix  $S_{ij}$ . In addition, enstrophy is a source term in the transport equation of dilatation  $S_{kk}$ :

$$\frac{D(s_{kk})}{Dt} = -s_{ik}s_{ki} + \frac{1}{2}\omega_k \omega_k + \frac{1}{\rho^2} \frac{\partial \rho}{\partial x_k} \frac{\partial p}{\partial x_k} - \frac{1}{\rho} \frac{\partial^2 p}{\partial x_k \partial x_k} + \frac{\partial}{\partial x_k} \frac{1}{\rho} \frac{\partial \tau_{kq}}{\partial x_q} \quad (11.1)$$

This transport equation relates the change of dilatation along a particle path which can be caused by the straining action of the dissipative motions ( $s_{ik}s_{ki}$ ) as well as by the rotational energy of the spinning motions as it is expressed by the enstrophy  $1/2\omega_k \omega_k$ . Pressure and density gradients as well as viscous diffusion can also affect dilatation. It should be note that the above transport equations reduces to the well known Poisson equation

$$\frac{1}{\rho} \frac{\partial^2 p}{\partial x_k \partial x_k} = -s_{ik}s_{ki} + \frac{1}{2}\omega_k \omega_k \quad (11.2)$$

for incompressible flows of constant density ( $s_{kk}=0$ ).

The distribution of the pdfs shown in figure 35 indicates that most of the data i.e. data with high frequency of occurrence are mainly associated with low amplitude fluctuations of enstrophy. However, it appears that there exists rare events, i.e. events with low probability of occurrence which have extremely high amplitude of enstrophy and which may be of significant importance in the dynamics of the fluid. This behavior observed in all experiments is indicative of highly fluctuating quantities.

Since the distributions shown in figure 35 are not normalized, the area under each them is indicative of the mean value of enstrophy. The data shows that enstrophy decreases with increasing the  $M_{\text{flow}}$ . In the case of the 2x2 grid with  $M=12.7$  mm, for instance, the mean value of enstrophy reduces by 25% when the flow Mach number increases by about 25%. In the case of the 3x3 grid enstrophy is decreased by 50% when the Mach number increases by 17%. Thus it appears that the effect of compressibility is to reduce enstrophy fluctuations. Even in the present cases of rather weakly compressible flows the effects on enstrophy are rather substantial.

It is very interesting to compare the effects of compressibility on velocity fluctuations with those on enstrophy fluctuations. Velocity fluctuations are increased with increasing  $M_{\text{flow}}$  while enstrophy fluctuations are decreased. Are these two results incompatible? The answer is no, if one considers that enstrophy varies as  $u^2/\lambda^2$  or better in non-dimensional terms as  $(u/U)^2(M/\lambda)^2$ . It appears that  $(\lambda/M)^2$  increases substantially faster with  $M_{\text{flow}}$  than  $(u/U)^2$ . In fact the present data confirm that. In addition, the variation of dissipation rate with the flow Mach number is exactly the same as that of enstrophy. Thus the conclusion that compressibility decreases enstrophy fluctuations and increases velocity fluctuations, appears to be genuine.

Figure 36 shows distributions of the pdfs of the dilatation  $1/\rho D\rho/Dt = -s_{kk}$  as measured in the four different experiments of the present investigation. Values are non-dimensionalized by  $M/U_1$ . The mean value of dilatation in this homogeneous flow is expected to be zero and the experimental data confirm it. The level of dilatation fluctuations is about 1/8 to 1/20 of the level of vorticity fluctuations. A comparison of the level of dilatational fluctuations with the

range of vorticity fluctuations as depicted from the pdfs shown in figures 33, 34 and 36 indicates that the former are about 5% to 7.5% of the latter in the case of the 2x2 grid ( $M=12.7$  mm) depending on  $M_{flow}$ , and 13% in the case of the 3x3 grid ( $M=8.4$  mm). These values are typical of weakly compressible turbulence with rather low fluctuations of Mach number (turbulent Mach number). Nevertheless compressibility effects are detectable. For instance, the data of figure 36 in the case of the 2x2 grid clearly show that dilatational fluctuations increase considerably with  $M_{flow}$ , while vorticity and enstrophy fluctuations decrease.

In the case of the 3x3 grid no substantial differences between the flows with two different Mach numbers could be detected. However, this may be an effect of the way dilatation is non-dimensionalized by  $M/U_1$  since dimensionalized values of  $1/\rho D\rho/Dt$  fluctuations are about 20% higher in the case of the  $M_{flow}=0.425$  than those in the lower  $M_{flow}=0.388$  case.

Distribution of pdfs of the non-dimensionalized quantity  $s_{ik}s_{kk}(M/U_1)^2$  which represents the dilatational part of dissipation are shown in figure 37. This term in the present cases of rather weakly compressible turbulence is about 50 to 100 times smaller than the corresponding solenoidal dissipation. In that sense its direct effect on turbulence maybe not significant. Nevertheless it is important to understand how it changes with Mach number. In the case of the 2x2 grid ( $M=12.7$  mm) compressible dissipation increases with  $M_{flow}$  while solenoidal dissipation decreases. The data also show that rare events with stronger amplitudes are present in the  $M_{flow}=0.425$  case than in the  $M_{flow}=0.388$  case.

No differences in the distributions of compressible dissipation between the two flows could be discerned in the case of the 3x3 grid. However, this effect can be attributed to the non-dimensionalizing parameter  $(M/U_1)^2$  because the raw, dimensionalized data indicated a 50 % increase in the values of compressible dissipation.

The transport equation of vorticity

$$\frac{D\omega_i}{Dt} = s_{ik}\omega_k - \omega_i s_{kk} + \varepsilon_{iq\eta} \frac{1}{\rho^2} \frac{\partial \rho}{\partial x_q} \frac{\partial p}{\partial x_\eta} + \varepsilon_{iq\eta} \frac{\partial^2 \tau_{ij}}{\partial x_q \partial x_j} \quad (11.3)$$

describes four dynamically significant processes for the vorticity vector  $\omega$ , namely that of stretching or compression and tilting by the strain  $s_{ik}$ , vorticity generation through dilatation, baroclinic generation through the interaction of pressure and density gradients and viscous diffusion. In the present work the first two terms have been evaluated directly. The baroclinic term could not be measured but order of magnitude analysis showed that it is rather small in the present flow. If the viscous term can be also ignored since its magnitude is also small, then the change of vorticity of a fluid element in a Lagrangian frame of reference can be entirely attributed to vortex stretching and/or tilting and to dilatational effects.

Figure 38 shows distributions of the pdfs of the longitudinal component of the stretching vector  $s_{ik}\omega_k$  for the four experiments carried out in the present investigation. Values are non-dimensionalized by  $(M/U_1)^2$  and plotted in semi-logarithmic scale. Typical characteristic of all distributions is their long tails which are indicative of strong but rare events with substantial contribution to the stretching process. The data also show that stretching fluctuations decrease with increasing  $M_{flow}$ . In both experiments with the two different grids, mean and fluctuating stretching appears to be lower in the cases of high  $M_{flow}$  than in the cases of low  $M_{flow}$ . This behavior is not surprising because vorticity is reduced with increasing flow Mach number and therefore source terms are expected also to decrease. However the dilatational generation of vorticity is affected by the flow Mach number in the opposite way. Figure 39 shows the distributions of the pdfs of  $\omega_i s_{kk}$  which describes the generation of vorticity by the expansion or compression of the rate of change of the specific volume since  $-1/\rho D\rho/Dt = 1/VDV/Dt = s_{kk}$ . In the case of the 2x2 grid ( $M=12.7$  mm), substantial increase in the level of fluctuations can be observed when the flow Mach number increases. This indicates that dilatational fluctuations, which increase with increase  $M_{flow}$ , dominate the process over vorticity fluctuations which are reduced with increased  $M_{flow}$ .

No substantial differences can be observed between the two distributions in the case of the 3x3 grid ( $M=8.4$  mm). This again can be attributed to the way the data are made non-dimensional, since the raw dimensionalized data show that compressibility increases the fluctuations of  $\omega_i s_{kk}$ . The long tails of the distributions also suggest that rare but violent events are substantially affecting these processes.

Some further insight of the dynamical processes involved in these flows can be gained by looking at the instantaneous signals of the various quantities present in the transport equations mentioned above. Figure 40a shows

signals of dissipation  $\omega_k \omega_k$ , dilatational dissipation  $s_{kk} s_{kk}$ , the three components of the vorticity stretching vector  $s_{1k} \omega_k$ ,  $s_{2k} \omega_k$ ,  $s_{3k} \omega_k$ , and the three components of the dilatational stretching vector  $\omega_1 s_{kk}$ ,  $\omega_2 s_{kk}$ ,  $\omega_3 s_{kk}$ . Each signal has been normalized by its r.m.s. and has been displaced by a multiple of 5 r.m.s. units for better visual aid. All signals exhibit a rather strong intermittent behavior which is characterized by bursts of high amplitude events, which sometimes reaches values up to 5 to 8 r.m.s. units, followed by less violent periods of time. Several of these bursts are evident in all signals, suggesting the existence of a dynamical flow phenomenon which may be the common cause.

It is also interesting to observe that the correlation between any two of these signals seems to be higher during any of the those violent events. In general there is some statistical correlation in several of the signals. For instance, a correlation coefficient of about  $\pm 0.04$  has been obtained between entranspy and any of the vorticity stretching components. During violent events which involved substantial vorticity stretching or compressing activities, this coefficient can be 2 to 5 times higher.

A comparison between  $\omega_k \omega_k$  and  $s_{kk} s_{kk}$ , shows that there is some correlation between them since some bursts can be observed on both signals. However there is a number of strong events on one signal without a corresponding event on the other. Figure 40b shows a portion of the previous signals expanded in time, with annotated boxes where several of the previous discussed characteristics and features are highlighted. The first box, centered at about time=2212, for instance, shows strong events which can be identified on all signals. The second box at about time=2260 shows an event detectable on  $\omega_k \omega_k$  but not on  $s_{kk} s_{kk}$ . The third box at about time=2330 shows an event on  $s_{kk} s_{kk}$  without a corresponding counterpart on  $\omega_k \omega_k$ . The signals also indicate that the durations of the strong events on  $s_{kk} s_{kk}$  are considerably shorter than the events identified on the  $\omega_k \omega_k$  signal.

The signals obtained in the experiment with  $M_{\text{flow}}=0.388$  and grid of  $M=12.7$  mm are shown in figure 41. They exhibit similar characteristics as the signals of figure 40. However the amplitude and the frequency of these bursting events appear to be higher while their duration is shorter than in the experiment with the lower Mach number.

## 12. Conclusions

The effects of compressibility in a nearly homogeneous and nearly isotropic flow of decaying turbulence have been investigated experimentally by carrying out high resolution measurements in a large scale shock tube research facility. A variety of grids of rectangular pattern of different mesh size was used to generate the flow field. The Reynolds number of the flow based on the mesh size,  $Re_M$ , ranged from 50,000 to 400,000 while the turbulent Reynolds number  $Re_\lambda$  based on Taylor's microscale  $\lambda$  was between 200 and 700 which constitutes one of the highest scale ever achieved in laboratory flow. The range of Mach number of the flows investigated was between 0.3 and 0.6 which was low enough to assure a shock free flow and reasonably high enough to contain compressibility effects.

The effects of compressibility can be classified into two categories. The first category includes those effects which have a direct impact on the flow. Compressible dissipation, for instance, is a typical example of a quantity which expresses a direct effect of compressibility on total dissipation. The indirect effects comprise the second category. This include effects which change the local or global behavior of the flow and therefore may cause significant changes of the incompressible part of the flow. Increasing the Mach number of the flow, for instance, can change the level of turbulent fluctuations in the flow which may subsequently affect the dissipation rate, particularly the incompressible part which accounts for most of the total dissipation in cases like the present subsonic flow. Direct effects of compressibility on turbulence may be described by the turbulent Mach number  $M_t$ , while indirect effects on turbulence may be characterized by the flow Mach number  $M_{\text{flow}}$ , and the Reynolds number  $Re_M$ . The parameters  $M_t$ ,  $M_{\text{flow}}$  and  $Re_M$ , however, are not completely independent from each other. A change in any of the three may cause a change in the other two. In that respect, the effects which each of the nominally independent variables impose on the flow may be difficult to distinguish. An attempt has been made here to identify the effects of  $M_{\text{flow}}$  and  $Re_M$  on homogeneous and isotropic turbulence.

The isotropy of the present flow was verified experimentally and it was found to be within the range reported for incompressible flows. In fact, it was established for the first time that isotropic compressible turbulence at moderate subsonic Mach numbers can be setup experimentally. The decay of Mach number fluctuations was found to follow a power law behavior similar to that describing the decay of incompressible isotropic turbulence



$$M_t^2 = B \left[ \frac{x}{M} - \left( \frac{x}{M} \right)_0 \right]^{-n}$$

where  $B$ ,  $(x/M)_0$  and  $n$  are constants depending on the flow Mach number as well as on the  $Re_M$  and grid. These constants have been determined concurrently so that the residual deviation from the original data is minimized. This approach represents a departure from previous practices where one of the three parameters was fixed and the other two were determined through a best fit of the data procedure. In that context, direct comparison of the present data with previously obtained values of any of the three constants may not be feasible. A direct consequence of the procedure followed in this investigation may be the fact that the exponent  $n$  has been found to reach values below 1, which indicates, in principle, a slower decay rate than that found in many previous cases under the assumption that one of the three unknown constants should be fixed.

In the present work, it was possible to investigate the effects of the Mach number and  $Re_M$  on the flow development independently from each other. The virtual origin tends to a reasonably constant value of 4.5 at high  $Re_M$  which is independent of the flow Mach number. The decay coefficient  $B$  and the decay exponent  $n$  decrease with increasing Mach number while the virtual origin  $(x/M)_0$  increases with increasing Mach number at a fixed  $Re_M$ .

Most probably the mechanism responsible for this effect is the inherently slow growth rate of compressible shear layers emanating from the cylindrical rods of the grid. Figure 42a shows a typical merging of shear layers to form an isotropic flow in the case of incompressible flows. The case of compressible shear layers is depicted in figure 42b where it is shown how a lower growth rate can result in longer virtual origin. If a shock wave had been formed in the vicinity of the grid as in the case of Zwart et al. (1996) the decay rate would have been drastically affected. Shock waves in the present case is not likely to appear at the present Mach numbers because the open area of the grids used is greater than that required to choke the flow through the grids. Therefore it is plausible to attribute the present results to the lower growth rate of compressible shear layers.

The dissipation rate of turbulent kinetic energy was found to increase with increasing flow Mach number for fine grids and decrease with increasing  $M_{flow}$  for coarse grids. As a result  $L_e$  and  $\lambda$  follow similar pattern: they both increase with increasing  $M_{flow}$  and decrease with increasing  $M_{flow}$  in the case of fine grids.

The results of the present investigation indicated that, for fine mesh grids,  $L_e$  and  $\lambda$  decrease with increasing  $M_{flow}$  and increase with increasing  $M_{flow}$  in the case of flows produced by coarse grids.

All longitudinal length scales increase with increasing  $M_{flow}$  while lateral integral length scales and viscous length scales are reduced with increasing  $M_{flow}$ . This work also demonstrated that at high Mach numbers flows, all length scales i.e.  $L_e$ ,  $\lambda$  and  $\eta$  increase with increasing mesh size or  $Re_M$ .

An attempt has also been made to measure all time-dependent velocity gradients involved in vorticity, its stretching, enstrophy and dissipation rates with adequately spatial and temporal resolution. This allowed estimates of dilatation  $s_{kk}$ , compressible dissipation  $s_{kk}^2$  and compressible stretching  $\omega_i s_{kk}$  to be obtained. These quantities are directly associated with compressibility effects. A common feature of all these quantities is that their fluctuations properly normalized by  $M$  and  $U_1$ , increase with increasing Mach number of the flow. Although this behavior may be expected, if one considers that in compressible shear layers increasing  $M_{flow}$  suppresses turbulent fluctuations then this conclusion is surprising.

The results of the present investigation have also shown that enstrophy fluctuations which comprise the solenoidal part of dissipation are reduced with increasing  $M_{flow}$ , a conclusion which is also verified by the results of dissipation obtained through the decay rate of turbulent kinetic energy for the case of coarse grids.

The time-dependent signals of enstrophy  $\omega_k \omega_k$ , dilatation  $s_{kk}$ , compressible dissipation  $s_{kk}^2$ , and the three components of the stretching vectors  $\omega_k s_{ki}$  and  $\omega_i s_{kk}$  indicated a highly intermittent behavior which is characterized by bursts of high amplitude followed by less violent periods of time. The results also show that the mean values of all these quantities are considerably smaller than their r.m.s. values which suggests that time-averaged vorticity transport equations are of very limited value in understanding vorticity related phenomena.

Table 5, presented at the end of this section, summarizes the conclusions for the parameters that were investigated in this work and their response to an increase of the mean flow Mach number and an increase in the mesh

size/ $Re_M$ . In this table three symbols are used: (  $\uparrow$  ) represents that the parameter increases with increasing  $M_{flow}$  or increasing mesh size/ $Re_M$ ,

(  $\downarrow$  ) represents that the parameter decreases with increasing  $M_{flow}$  or increasing mesh size/ $Re_M$  and finally (  $\updownarrow$  ) represents that the parameter because of compressibility effects does not present a specific trend with increasing  $M_{flow}$  or increasing mesh size/ $Re_M$ .

The financial support provided by NASA Grant #NAG-1590 monitored by Mr. Dennis Bushnell and by AFOSR Grant #F49620-98-0358 monitored by Dr. Steve Walker is greatly acknowledged.

	INCREASING $M_{flow}$	INCREASING $Re_M / M$
A	$\downarrow$	$\updownarrow$
$(x/M)_0$	$\uparrow$	$\downarrow$
n	$\downarrow$	$\updownarrow$
u	$\uparrow$	$\updownarrow$
$M_t$	$\uparrow$	$\updownarrow$
$\varepsilon$	$\uparrow$ Fine grids; $\downarrow$ Coarse grids	$\updownarrow$
$\varepsilon M/U^3$	$\uparrow$ Fine grids; $\downarrow$ Coarse grids	$\updownarrow$
$L_e$	$\uparrow$ Coarse grids; $\downarrow$ Fine grids	$\uparrow$
$\lambda$	$\uparrow$ Coarse grids; $\downarrow$ Fine grids	$\uparrow$
$\eta$	$\downarrow$	$\uparrow$
$L_{11}(\xi_1)$	$\updownarrow$	$\downarrow$
$L_{11}(\xi_2)$	$\downarrow$	$\updownarrow$
$s_{kk}^* M/U^3$	$\uparrow$	
$s_{kk}^{*2} M/U^3$	$\uparrow$	
$\omega_i s_{kk}^* M/U^3$	$\uparrow$	

Table 5: Summary of conclusions for the decaying isotropic flowfield.

## References

Andreopoulos, J., 1983a "Improvements of the Performance of Triple Hot Wire Probes", Rev. Sc. Instrum., vol. 54, 733-740.

- Andreopoulos, J., 1983b. "Statistical Errors Associated with Turbulence Intensity and Probe Geometry in Hot-Wire Anemometry," *Physics E. Sci. Instr.*, Vol. 16, 1264-1271.
- Andreopoulos, J., and Honkan, A., 1996, "Experimental Techniques for Highly Resolved Measurements of Rotation, Strain and Dissipation Rate Tensors in Turbulent Flows," *Meas. Science & Technol.*, vol. 7, pp 1462-1472, 1996.
- Andreopoulos, J. and Muck, K. C., 1987, "Some New Aspects of the Shock-Wave Boundary Layer Interaction in Compression Ramp Corner", *J. Fluid Mech.*, vol.180, 405.
- Balint, J., Wallace, J.M., Vukoslavcevic, P., 'The velocity and vorticity vector fields of a turbulent boundary layer. Part 2 Statistical Properties.', *J. Fluid Mech.*, vol. 228, pp. 53, 1991.
- Batchelor, G. K., 1953, "The Theory of Homogeneous Turbulence," Cambridge University Press.
- Batchelor, G. K., and Townsend, A. A., 1949, "The Nature of Turbulent Motion at High Wave Numbers," *Proc. Roy. Soc. A*, 199, 238.
- Batchelor, G. K., and Townsend, A. A., 1947, "Decay of Vorticity in Isotropic Turbulence," *Proc. R. Soc. London Ser. A* 190, 534.
- Bennett J. C., and Corrsin S., 1978, "Small Reynolds Number Nearly Isotropic Turbulence in a Straight Duct and Contraction," *Phys. Fluids*, 21 (12), 2129.
- Bradshaw, P., and Huang, G.P., 1995, "The law of the wall in turbulent flow", *Proc. R. Soc. Lond. A* 451, pp. 165-188.
- Briassulis, G., 1996, "Interaction of Isotropic an Homogeneous Turbulence with Shock Waves," PhD Thesis, City University of New York.
- Briassulis, G., and Andreopoulos, J., 1994, "Unsteady Pressure Field in Shock Wave Interaction with Grid Generated Turbulence in a Shock Tube," *AIAA Paper No 94-2277*.
- Briassulis, G., and Andreopoulos, J., 1996, "High Resolution Measurements of Isotropic Turbulence Interacting with Shock Waves," *AIAA Paper No 96-0042*.
- Briassulis, G., Honkan, A., Andreopoulos, J., and Watkins, B. C., 1995, "Applications of Hot-Wire Anemometry in Shock Tube Flows," *Exp. in Fluids*, vol. 19, 29.
- Briassulis, G., Agui, J., Andreopoulos, J., and Watkins, B. C., 1996, "A Shock Tube Research Facility for High-Resolution Measurements of Compressible Turbulence," *Experimental Thermal and Fluid Science*, pp. 430-446.
- Budwig, R., Zwart, P., J., Nguyen, V., and Tavoularis, S., "Grid Generated Turbulence in Compressible Streams," 2nd Symp. on Transitional and Turbulent Compressible Flows, Aug. 1995.
- Compte-Bellot, G., and Corrsin, S., 1966, "The use of contraction to improve the isotropy of gri-generated turbulence," *J. Fluid Mech.*, vol. 25, pp. 657-682.
- Compte-Bellot, G., and Corrsin, S., 1971, "Simple Eulerian time correlation of full- and narrow-band velocity signals in grid-turbulence, isotropic turbulence," *J. Fluid Mech.*, vol. 48, pp. 273-337.
- Dryden, H., L. 1943, "A Review of the Statistical Theory of Isotropic Turbulence," *Q. Appl. Math.* 1, 7.

- Favre, A., 1965, "Équations des Gaz Turbulents Compressibles I," J. Méc., vol 4, 361.
- Frenkiel, F., N., and Klebanoff, P., H., 1971, "Statistical Properties of Velocity Derivatives in Turbulent Field," J. Fluid Mech., vol. 48, 183.
- Frenkiel, F., N., Klebanoff, P., H., and Huang, T., T., 1979, "Grid Turbulence in Air and Water," Phys. Fluids, 22 (9), 1606.
- George, W. K., 1992, "The decay of homogeneous isotropic turbulence" Phys. Fluids A 4 (7), pp1492-1509.
- Gutmark, E., J., Schadow, K., C., and Yu, K., H., 1995, "Mixing Enhancement in Supersonic Free Shear Flows," Annu. Rev. Fluid Mech., vol. 27, 375.
- Honkan, A., and Andreopoulos, J., 1992, "Rapid compression of grid-generated turbulence by a moving shock wave", Phys. Fluids A, 4 (11).
- Honkan, A., and Andreopoulos, Y., 1997, "Vorticity, strain-rate and dissipation characteristics in the near-wall region of turbulent boundary layers," J. Fluid Mech., vol. 350, pp. 29-96.
- Honkan, A. Watkins C. B. and Andreopoulos, J., 1994, "Experimental Study of Interactions of Shock Wave with Free Stream Turbulence" , J. Fluids Eng., vol. 116, 763.
- Kistler, A., L., and Vrebalovich, T., 1966, "Grid Turbulence at large Reynolds numbers," J. Fluid Mech., vol. 26, 37.
- Klebanoff, P. S., "Characteristics of turbulence in a boundary layer with zero pressure gradient", NACA TN 3178, 1954
- Klewicki, J. C., 1989 "On the Interactions Between the Inner and Outer Region Motions in Turbulent Boundary Layers", Ph.D. dissertation, Michigan State University, East Lansing, Michigan.
- Kovaszny, L. S.G., 1950, "The Hot-Wire Anemometer in Supersonic Flows," J. Aeronautical Sciences, 17, 565-573.
- Lee, L., Lele, S. K. and Moin, P., 1993, "Direct Numerical Simulation of Isotropic Turbulence Interacting with a Weak Shock Wave", J. Fluid Mech., vol. 251, 533.
- Lele, S. K., 1994, "Compressibility Effects on Turbulence," Ann. Rev. Fluid Mech., vol. 26, pp. 211-254.
- Lemonis, G. C., 1995, "An experimental study of the vector fields of velocity and vorticity in turbulent flows," Doctoral Thesis, Swiss Federal Institute of Technology, Institute of Hydromechanics and Water Resources.
- Mohamed, S. M., and LaRue, C. J., 1990, "The Decay Power Law in Grid Generated Turbulence," J. Fluid Mech., vol. 219, 195.
- Morkovin, M.V., 1956, "Fluctuations and Hot-wire Anemometry in compressible flows," AGARDograph 24.
- Simmons, L., F., G., and Salter C., 1934 , "Experimental Investigation and Analysis of the Velocity Variation in Turbulent Flow," Proc. R. Soc. London, Ser. A 145, 212.
- Smits A. J., and Muck K. C., 1987, "Experimental Study of Three Shock Wave/Boundary layer Interactions," J. Fluid Mech., vol. 182, pp. 291-314.
- Spalart, P. R., 1988 "Direct Simulation of a Turbulent Boundary Layer up to  $Re = 1410$ ", J. Fluid Mech., 187, p. 61.

Spina, E., F., Smits, A., J., and Robinson, S., K., 1994, "The Physics of Supersonic Turbulent Boundary Layers," *Annu. Rev. Fluid Mech.*, vol. 26, 287.

Tan-Atichat, J., Nagib, H., M., and Loehrke, R., I., 1982, "Interaction of Free-Stream Turbulence with Screens and Grids: A Balance between Turbulence Scales," *J. Fluid Mech.*, vol. 114, 501.

Tavoularis S., Bennett J. C. and Corrsin S., 1978, "Velocity derivative skewness in small Reynolds number, nearly isotropic turbulence," *J. Fluid Mech.*, vol. 88, 63.

Tennekes, H. and Lumley, J. L., 1972. "A First Course in Turbulence", Boston, MA., MIT press .

Tsinober, A., Kit, E., and Dracos, T., 1992, "Experimental Investigation of the Field of Velocity Gradients in Turbulent Flows," *J. Fluid Mech.*, vol. 242, 169.

Wyngaard, J.C., 1969, "Spatial Resolution of the Vorticity Meter and other Hot-Wire Arrays," *J. Phys. E: Sci: Instrum.* 2, 983-987.

Zeman, O., 1990, "Dilatation dissipation: The concept and application in modeling compressible mixing layers" *Phys. Fluid A* 2 (2), pp178-188.

Zwart, P., Budwig, R., and Tavoularis, S., 1996, "Grid Turbulence in Compressible Flow," private communication.

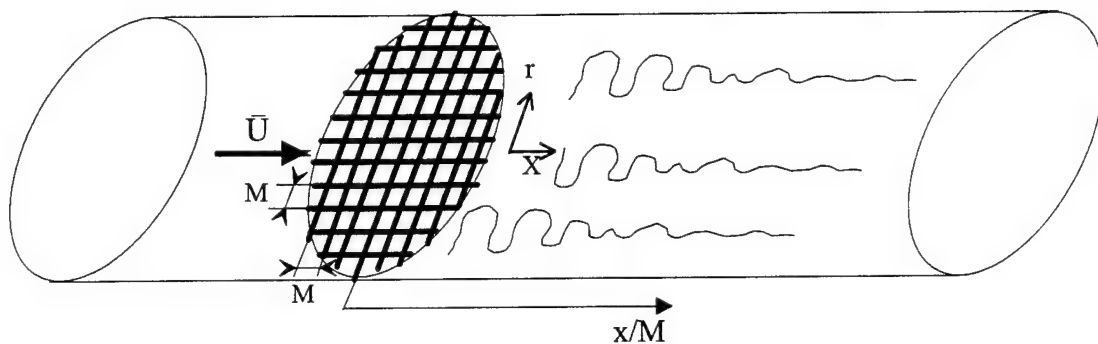


Figure 1: Grid generated flow schematic.

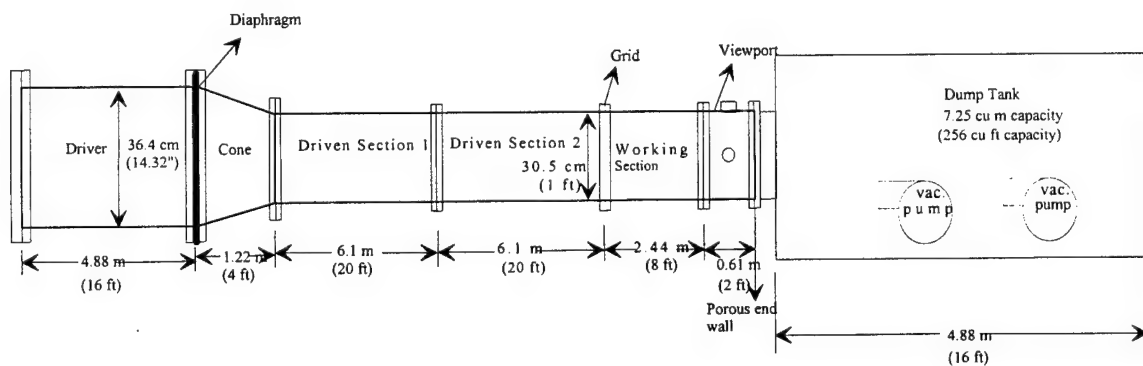


Figure 2a: Shock Tube Research Facility (not to scale)



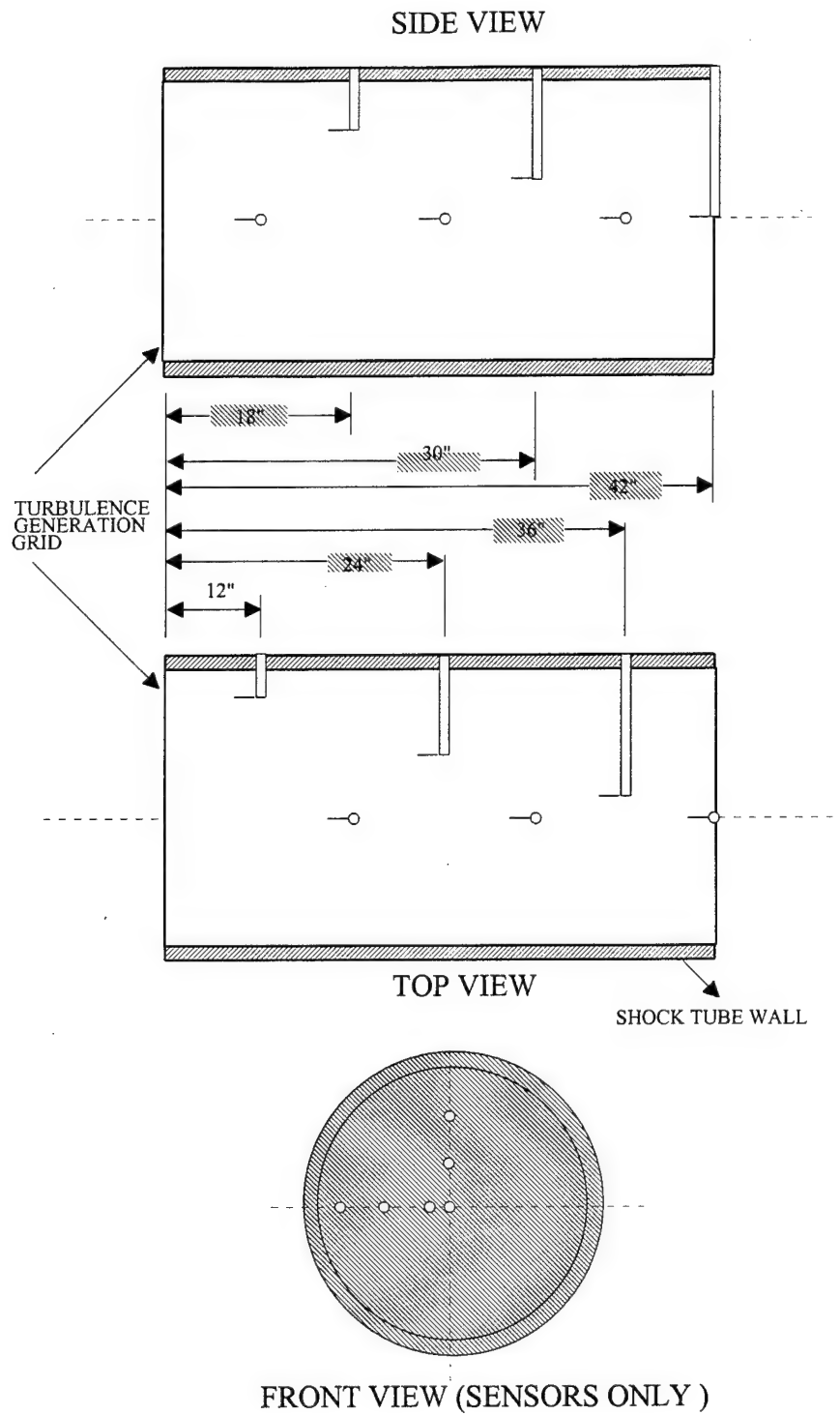


Figure 2b: X-Wire probes locations and arrangement in the shock tube.

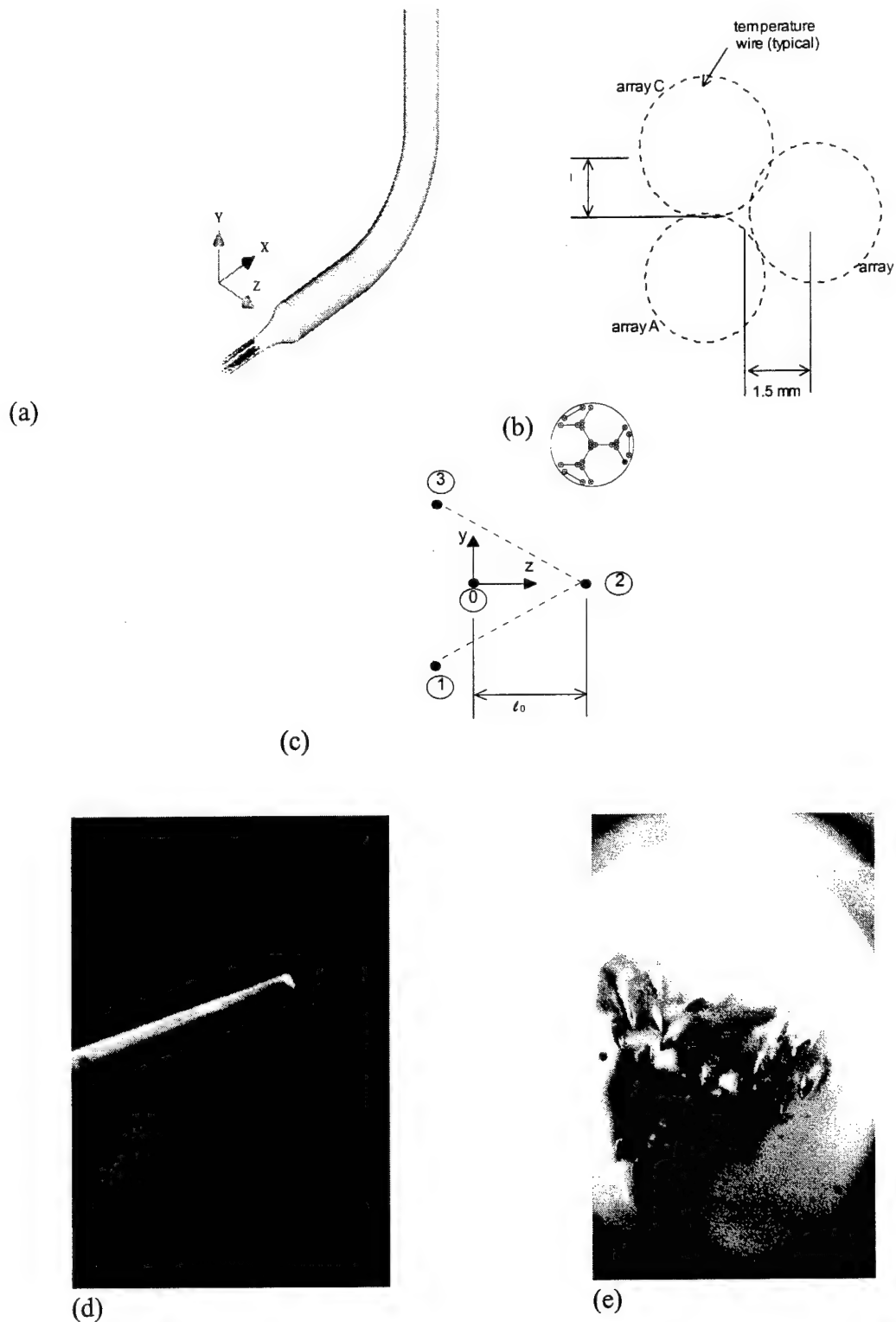


Figure 3: Vorticity probe: (a) rendered drawing in perspective view (b) probe sensor geometry (c) layout of probe centroids (d) photograph showing size comparison with toothpick (e) close-up view directly into probe.

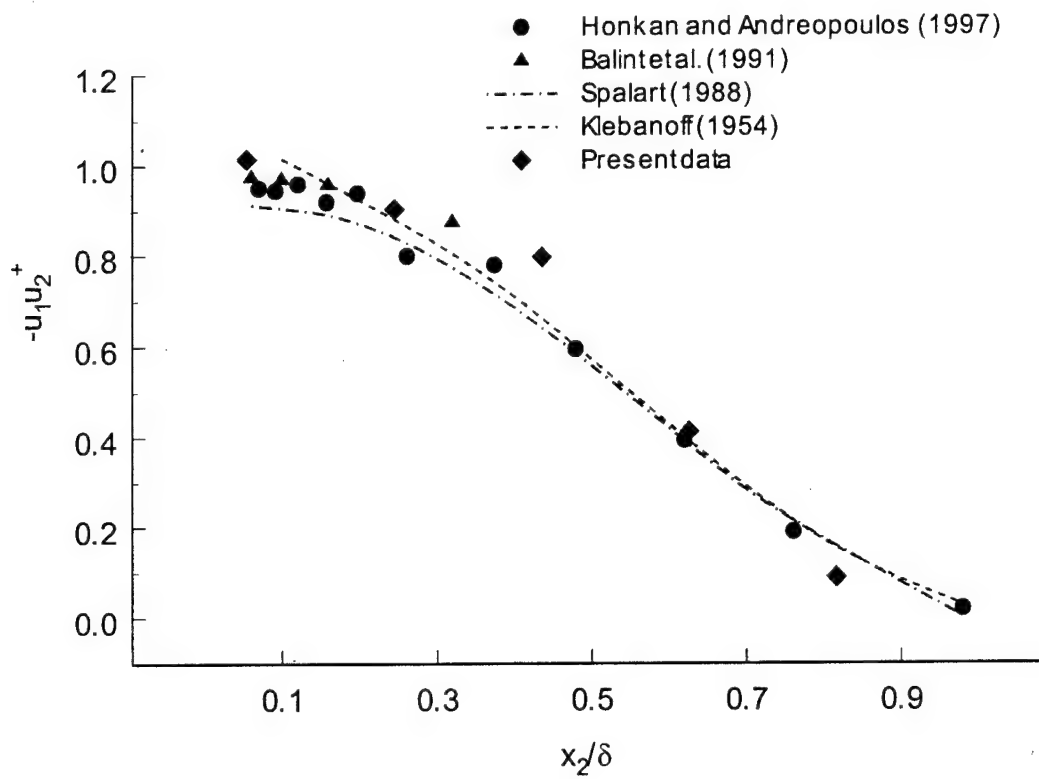


Figure 4: Normalized shear stress in boundary layer experiment and comparison with previous measurements

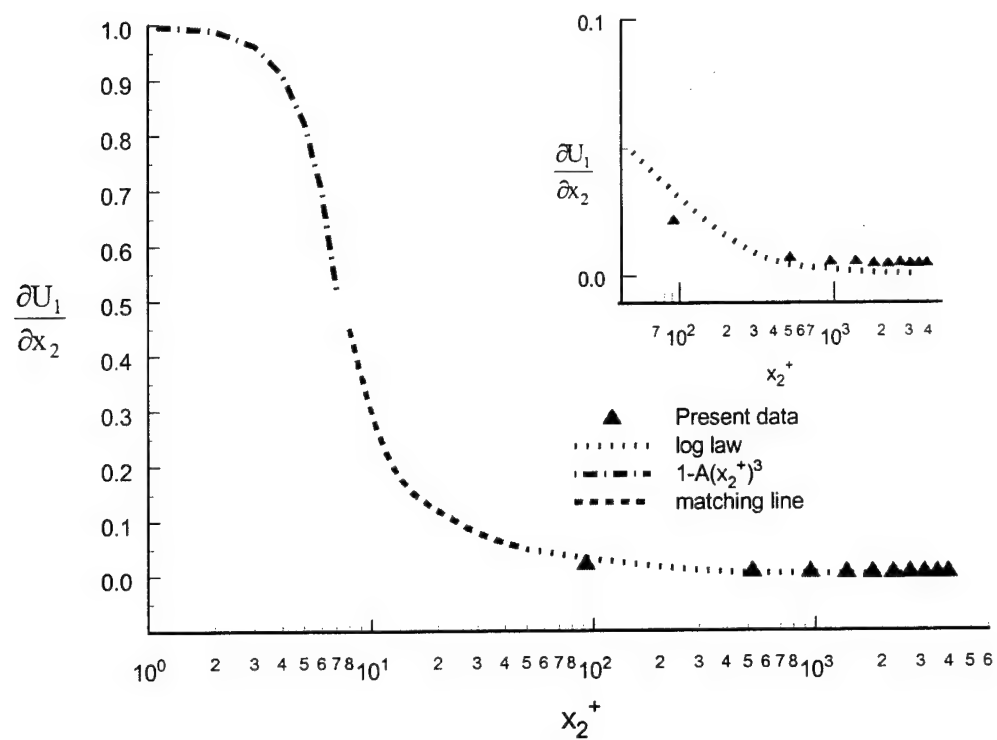


Figure 5: Mean velocity gradient across boundary layer.

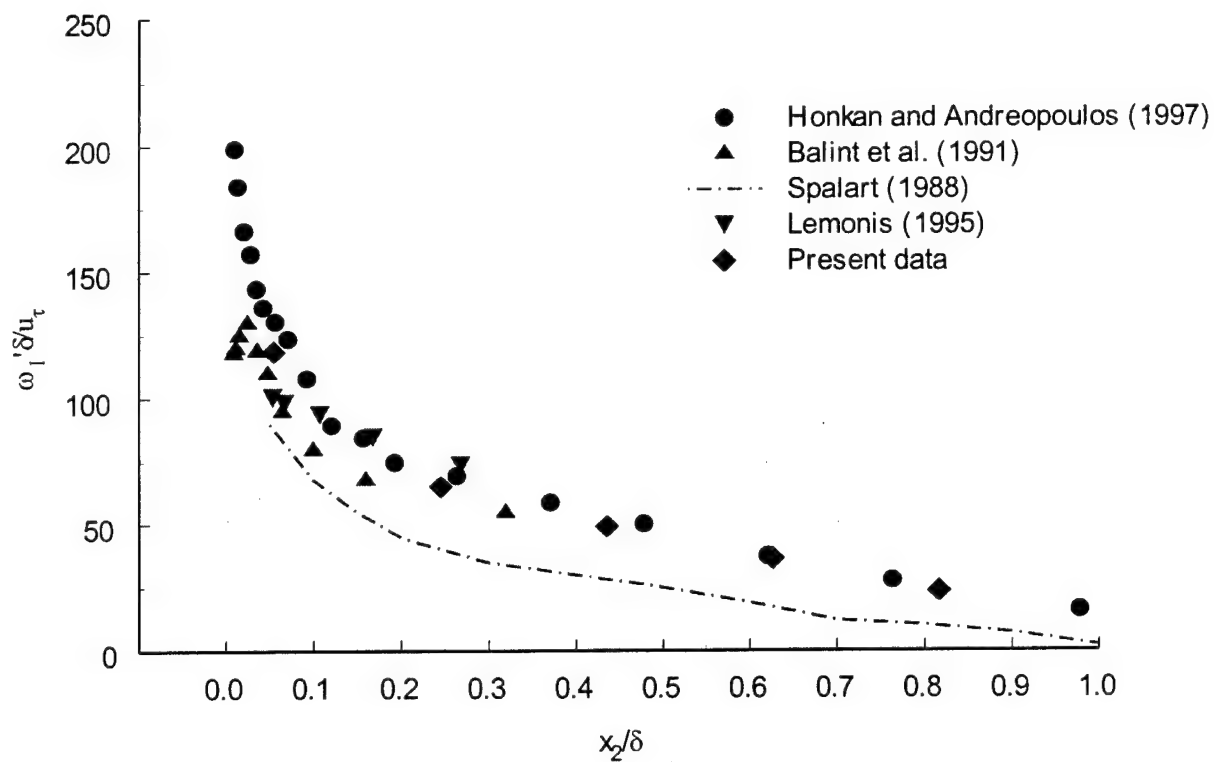


Figure 6a: R.m.s. of axial vorticity fluctuations normalized by  $u_\tau$  and  $\delta$ .

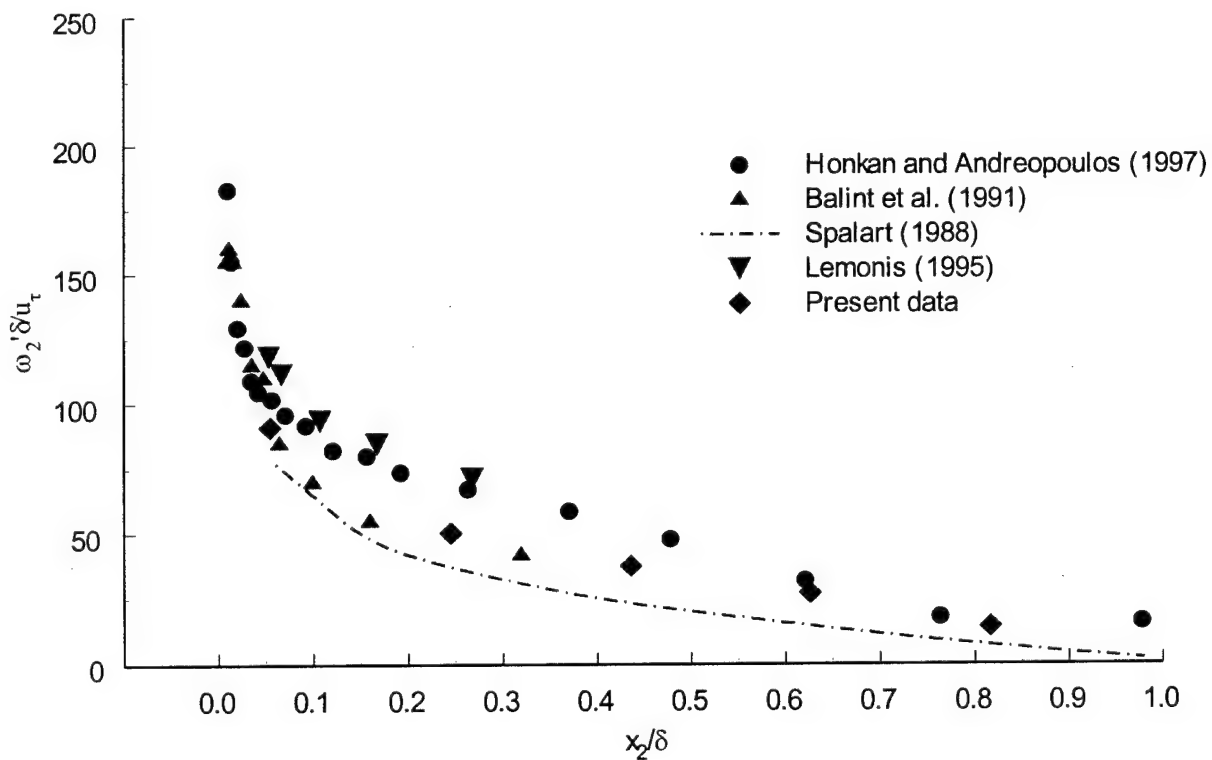


Figure 6b: R.m.s. of normal vorticity fluctuations normalized by  $u_\tau$  and  $\delta$ .

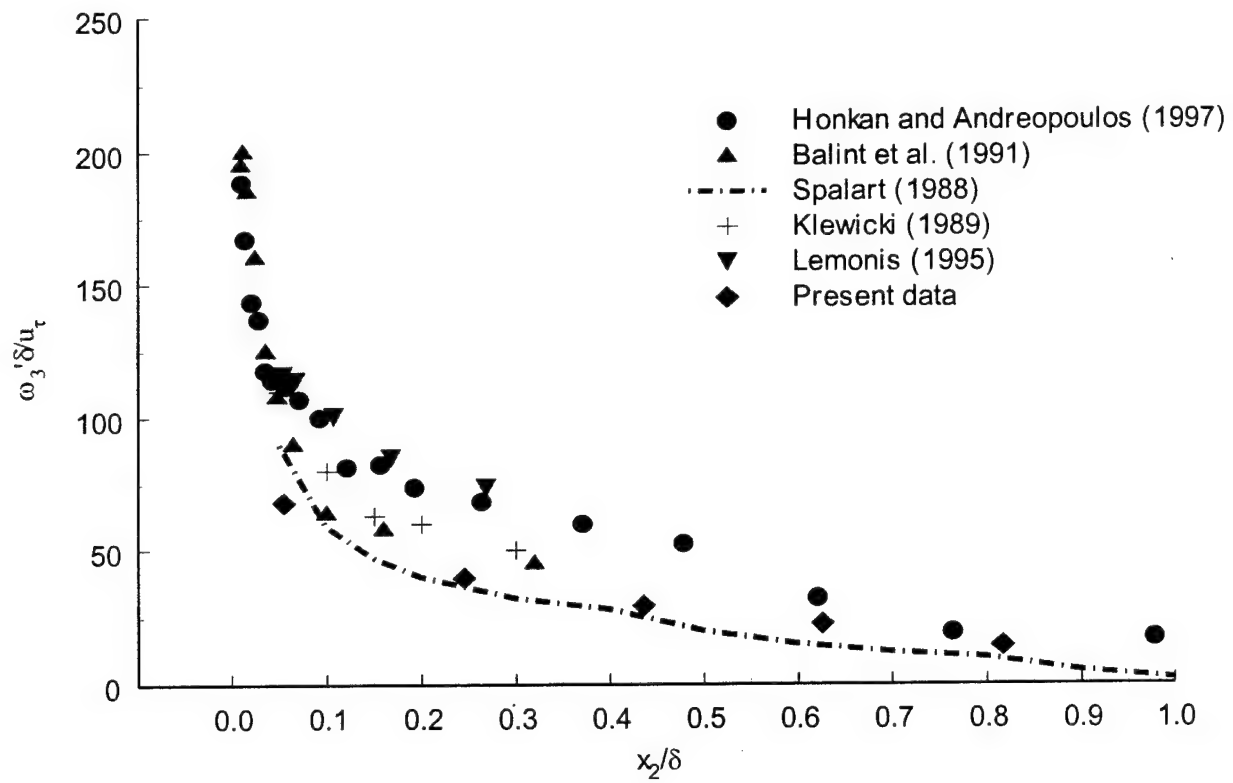


Figure 6c: R.m.s. of spanwise vorticity fluctuations normalized by  $u_\tau$  and  $\delta$ .



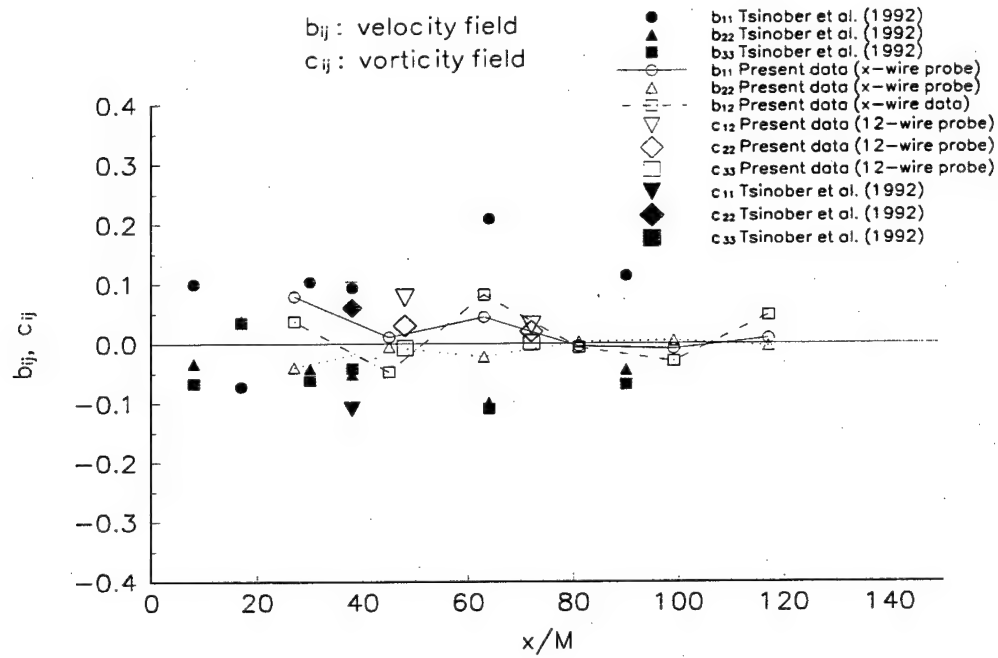


Figure 7: Anisotropy tensors  $b_{ij}$  (velocity field) and  $c_{ij}$  (vorticity field).

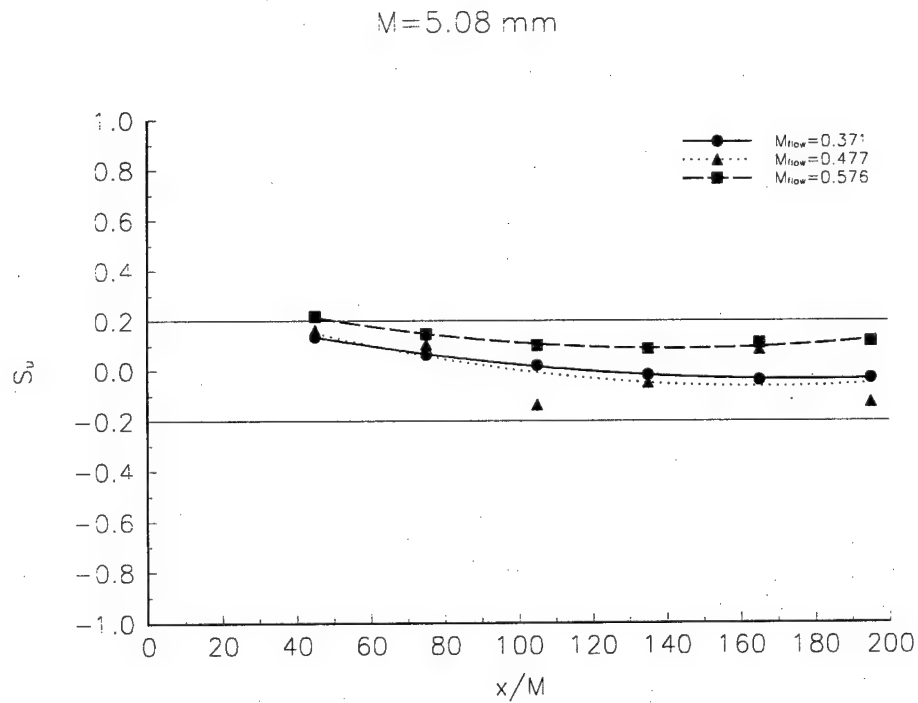


Figure 8: Skewness of velocity fluctuations for three different flowfields.

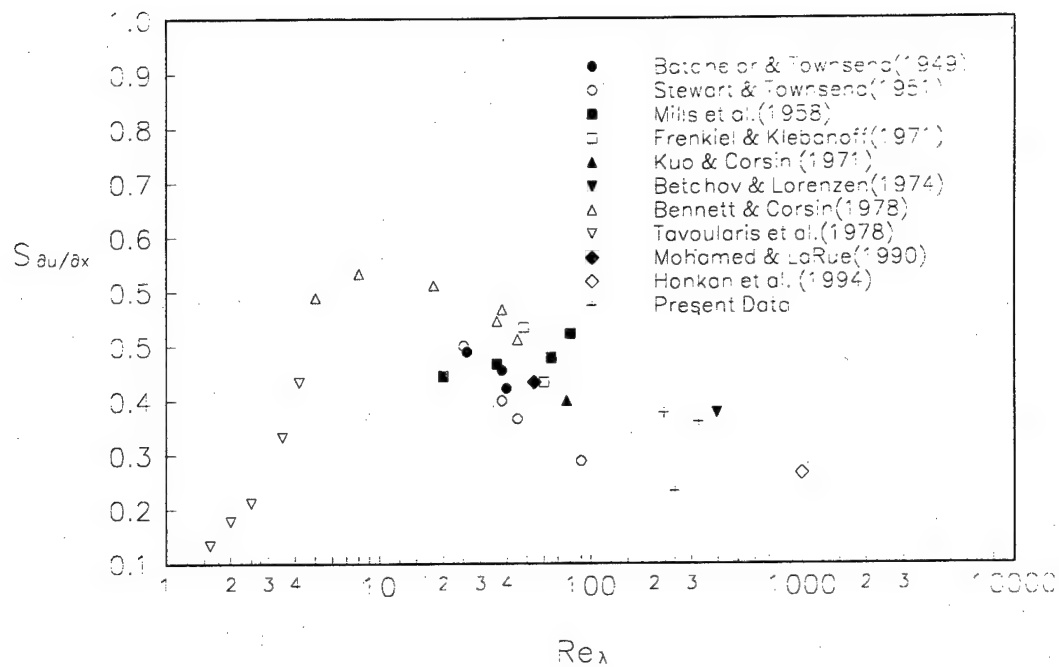


Figure 9a: Skewness of the derivative of velocity fluctuations for different flowfields.

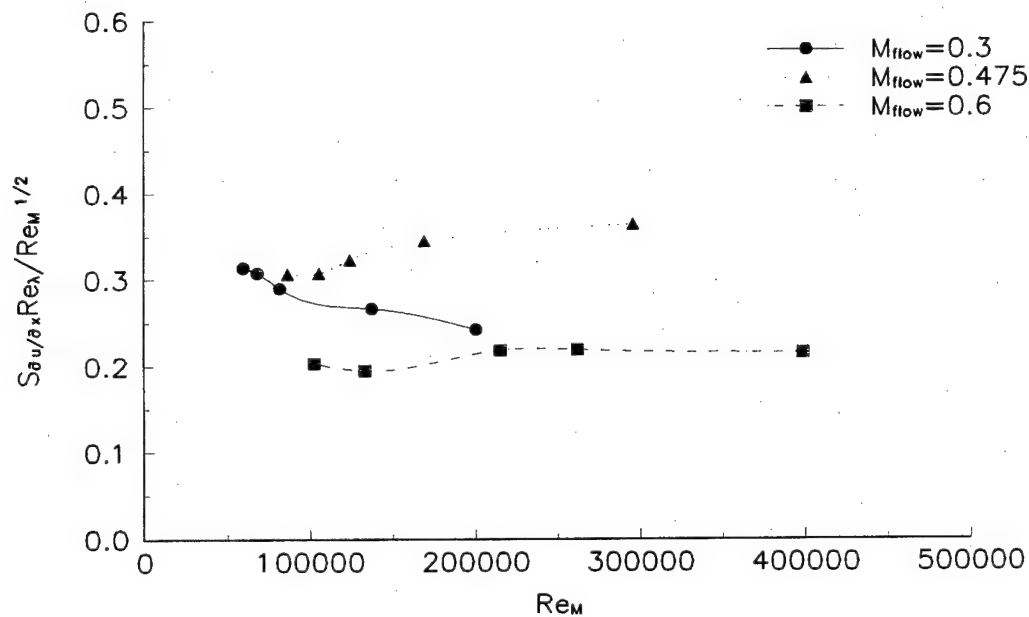


Figure 9b: The ratio  $S_{\partial u / \partial x} Re_{\lambda} / Re_M^{1/2}$  for various  $M_{flow}$

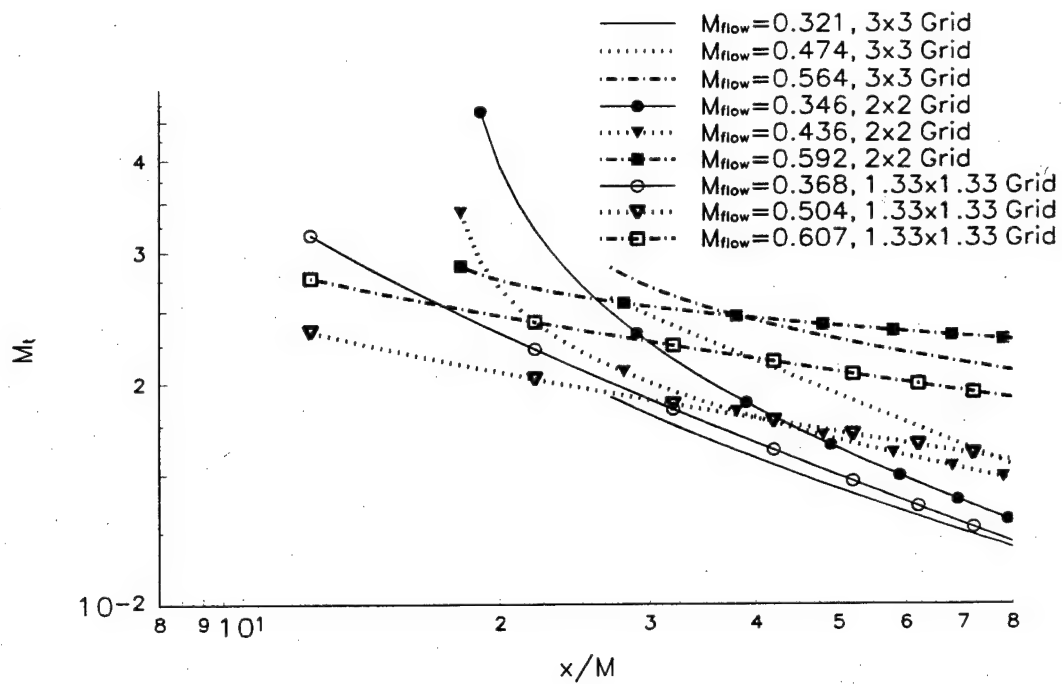


Figure 10: Mach number fluctuations for various experiments

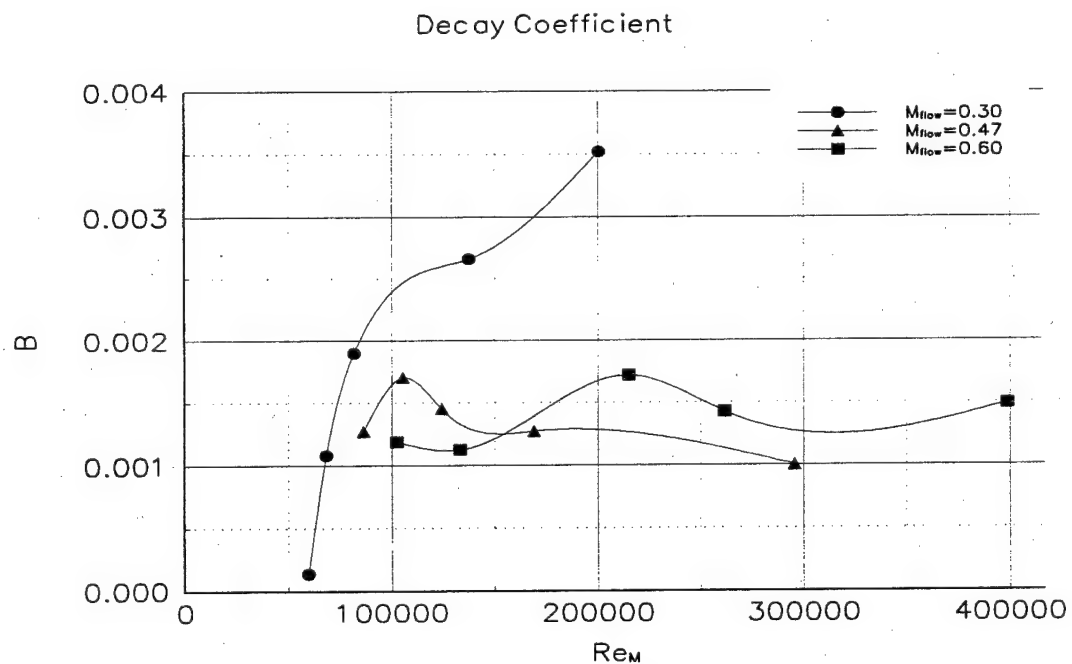


Figure 11a: Decay coefficient  $B$  vs  $Re_M$  for 3 different Mach numbers.

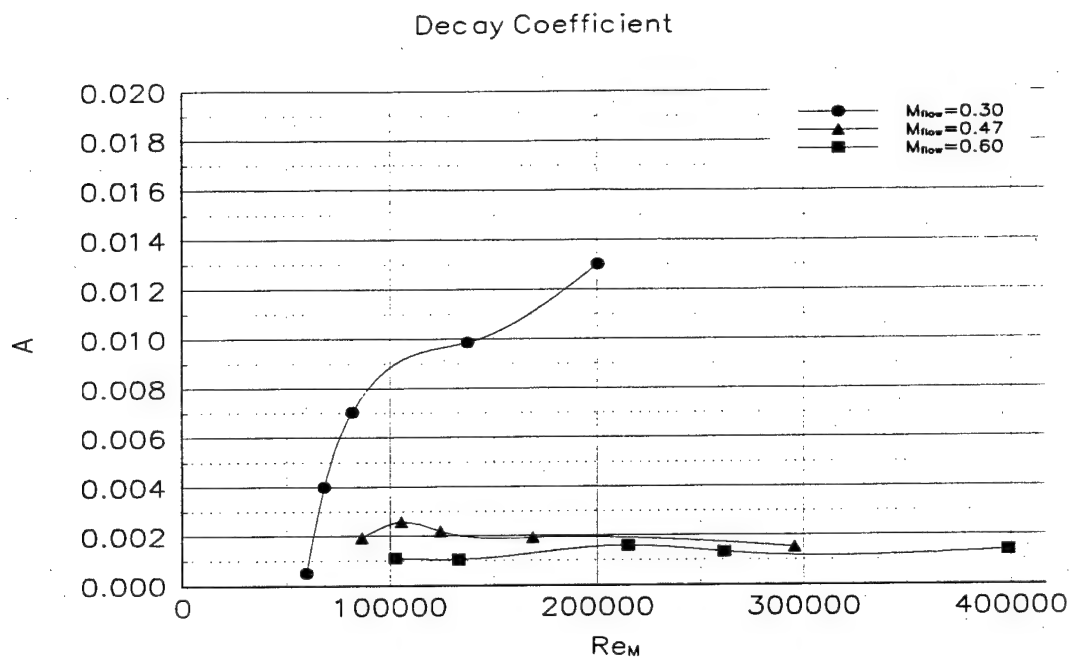


Figure 11b: Decay coefficient A vs  $Re_M$  for 3 different Mach numbers.

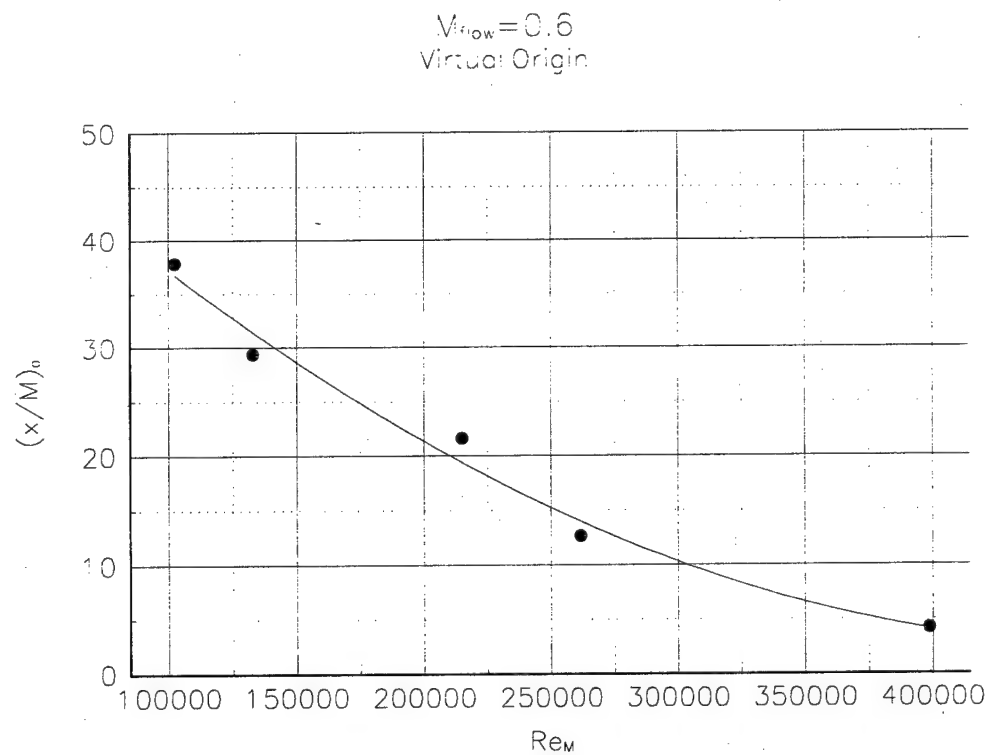


Figure 12: Virtual origin vs  $Re_M$  for  $M_{flow}=0.6$

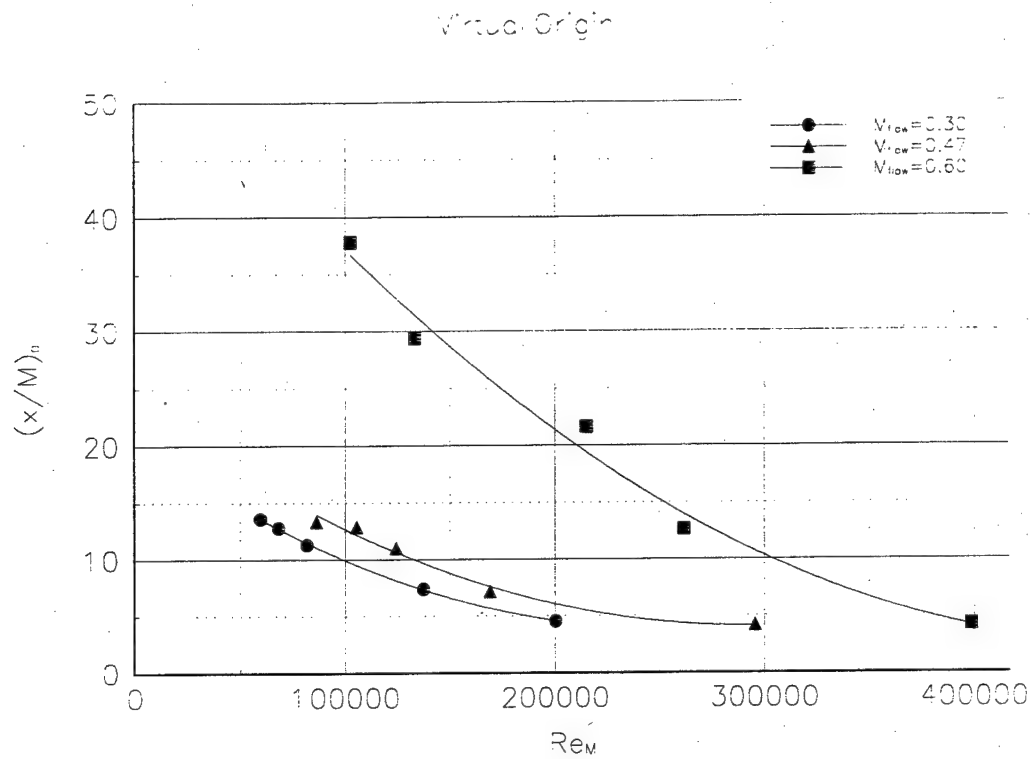


Figure 13: Virtual origin vs  $Re_M$  for 3 different Mach numbers

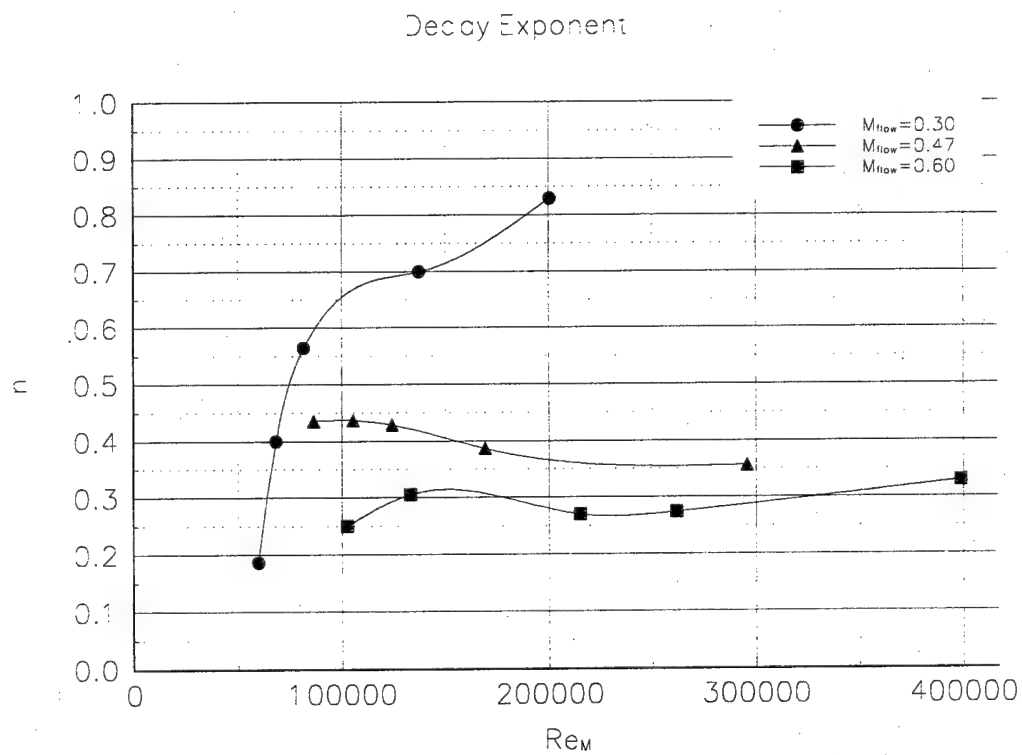


Figure 14: Decay exponent  $n$  vs  $Re_M$  for 3 different Mach numbers

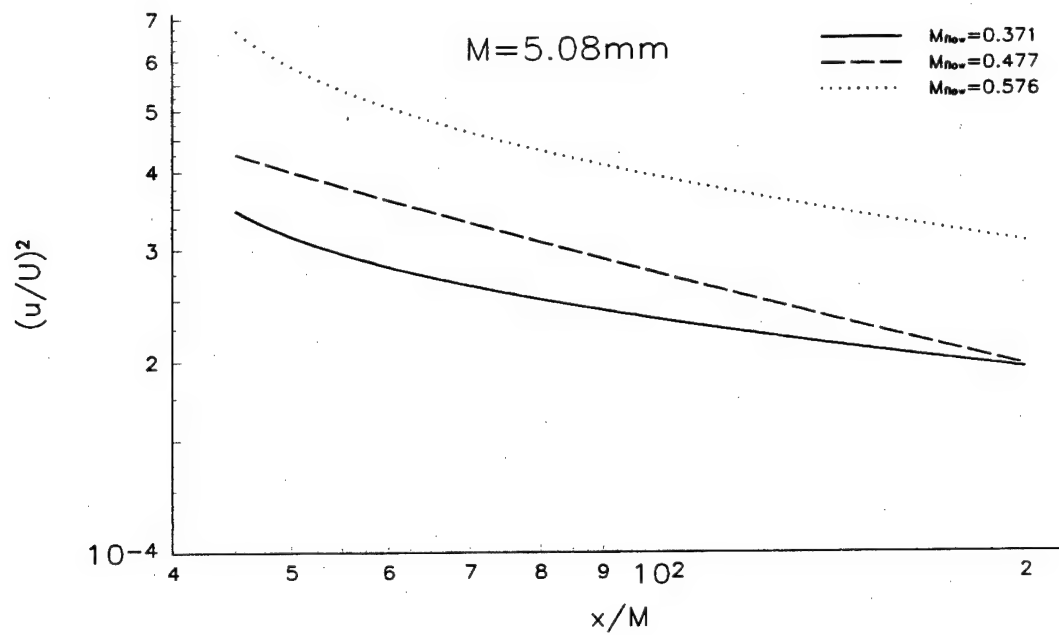


Figure 15: Decay of velocity fluctuations for various Mach numbers

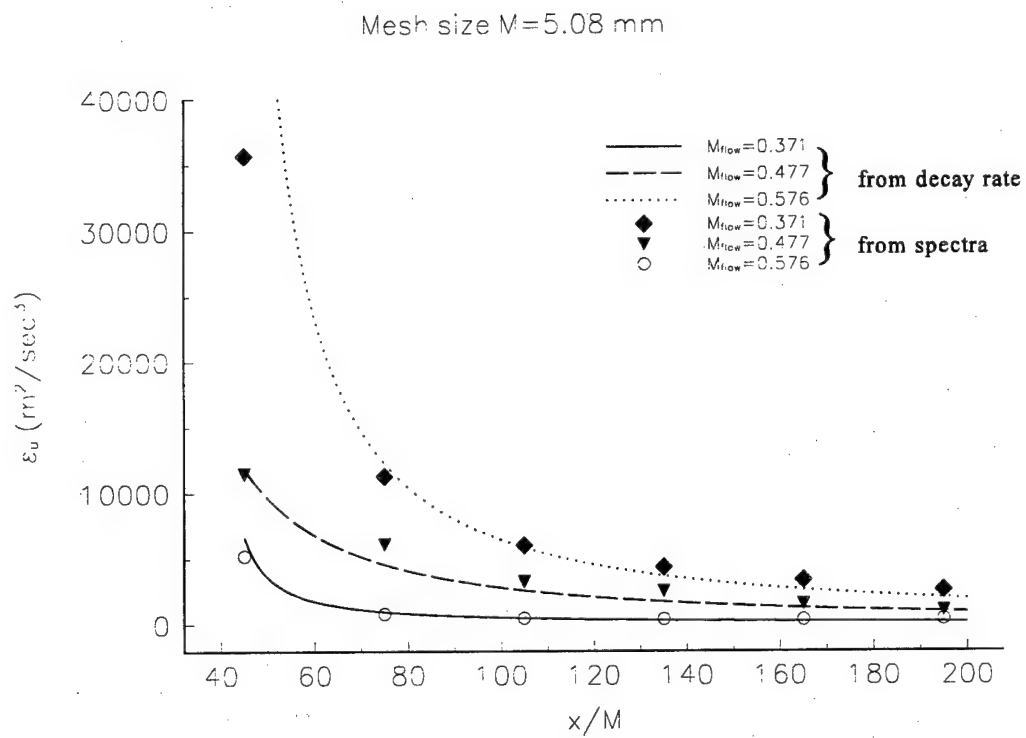


Figure 16a: Dissipation rate of kinetic energy vs  $x/M$  for 3 different Mach numbers



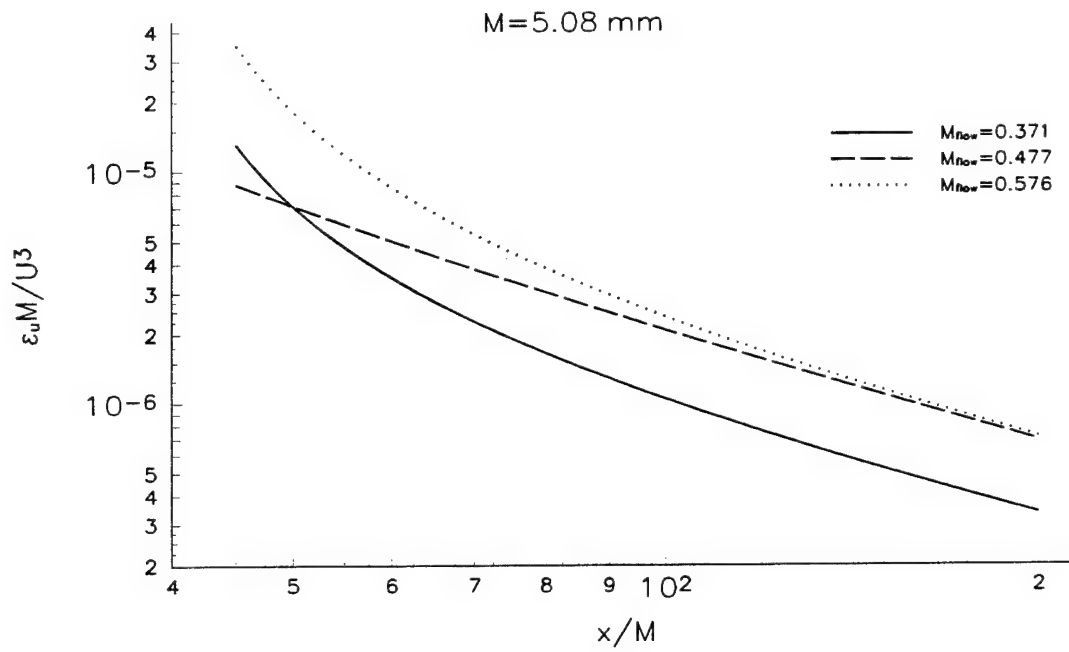


Figure 16b: Non-dimensional dissipation rate for three Mach numbers

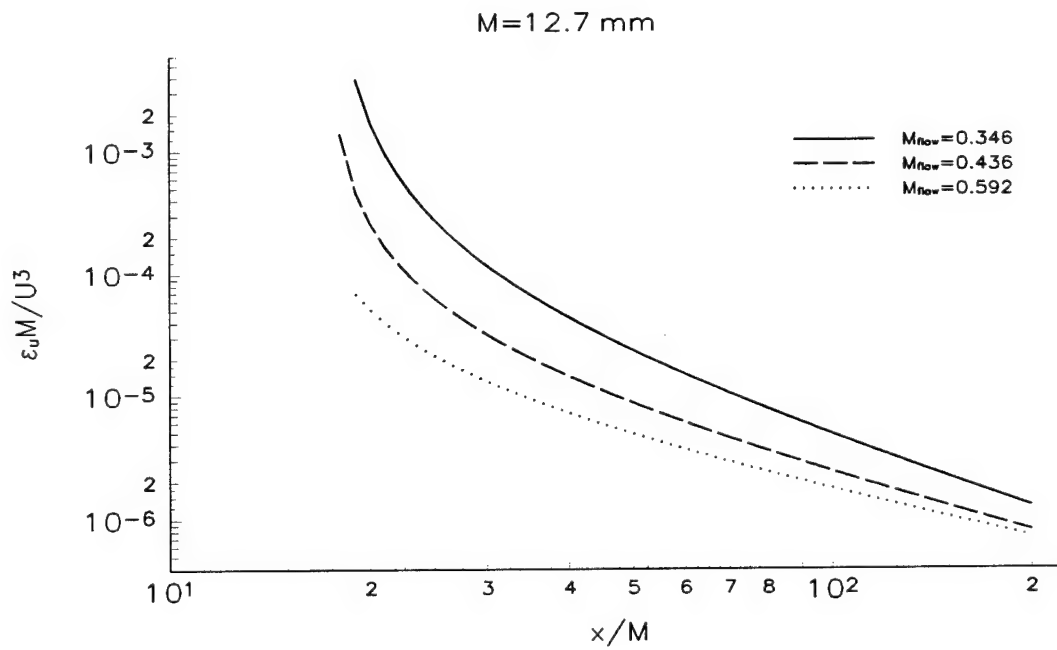


Figure 16c: Non-dimensional dissipation rate for three Mach

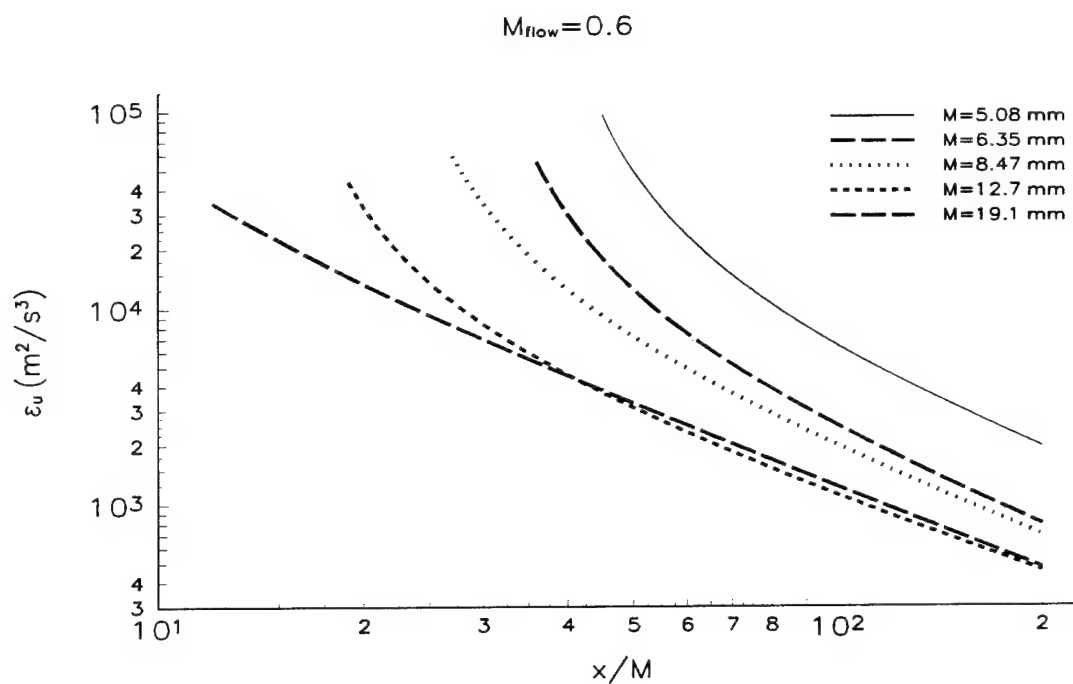


Figure 17: Dissipation rate of kinetic energy for various mesh sizes.

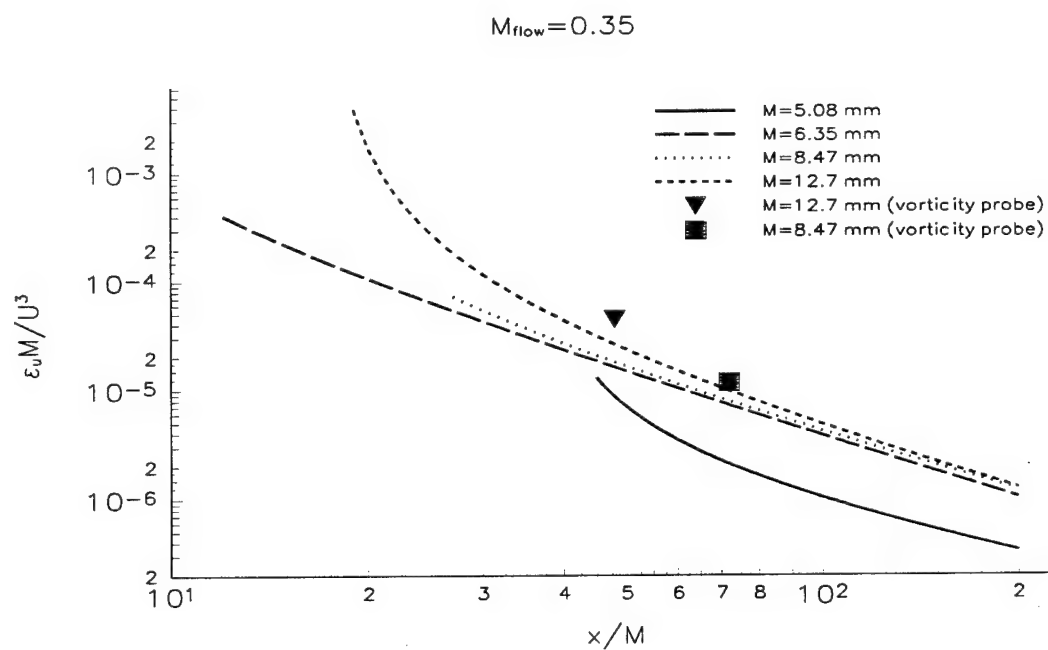


Figure 18: Non dimensional  $\epsilon$  for  $M_{flow}=0.35$  and various mesh sizes.

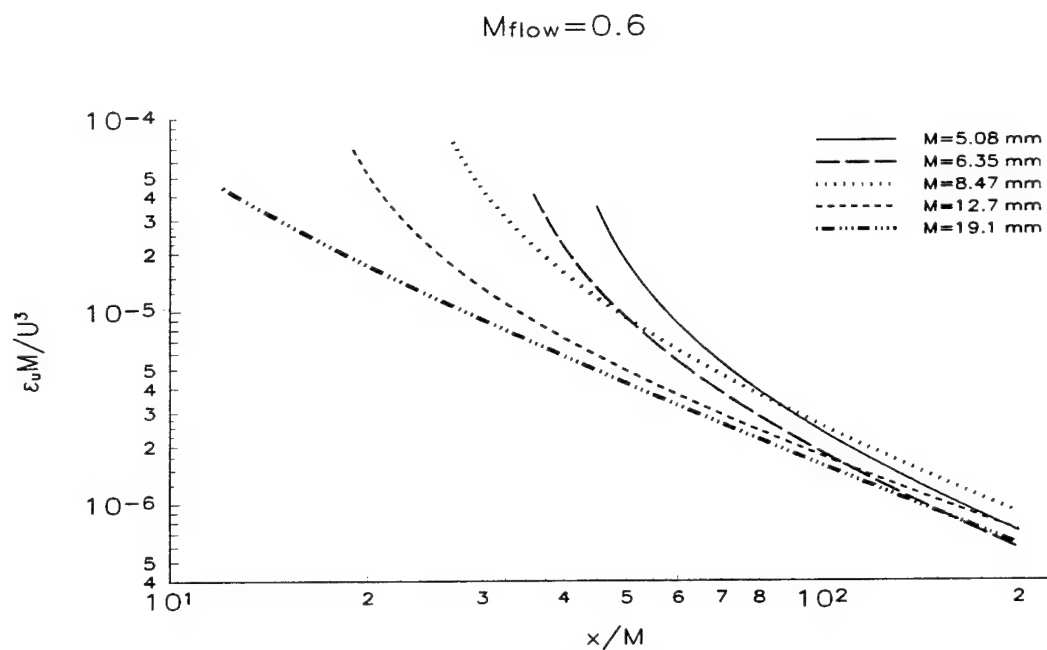


Figure 19: Non dimensional  $\epsilon$  for  $M_{flow}=0.6$  and various mesh sizes.

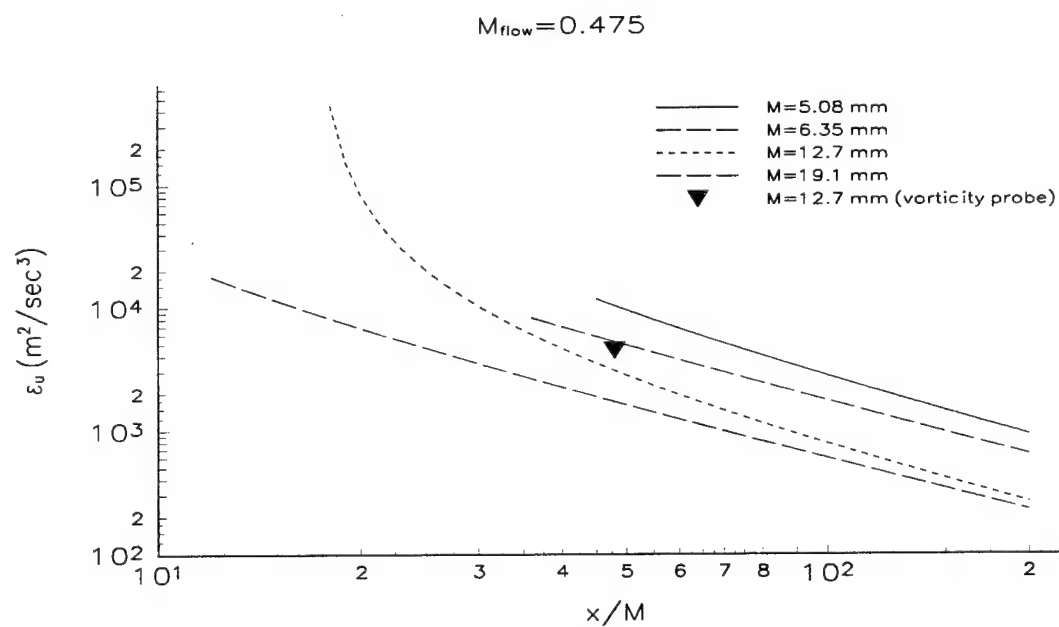


Figure 20: Dissipation rate of kinetic energy for various mesh sizes at  $M_{flow}=0.475$

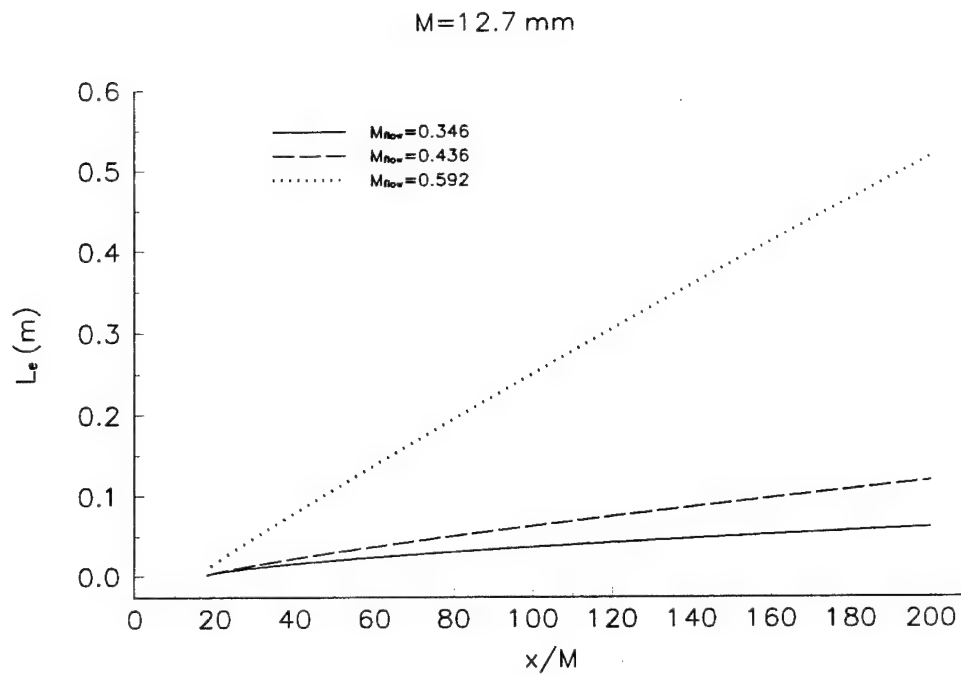


Figure 21: Dissipative length scale for three mean flow Mach numbers.

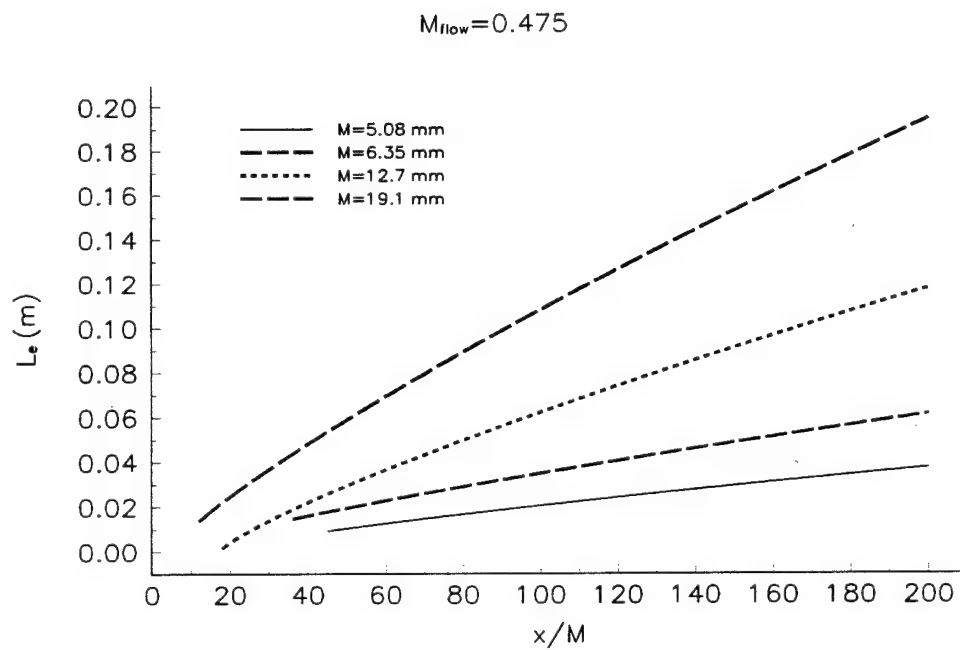


Figure 22: Dissipative length scale for several mesh sizes.

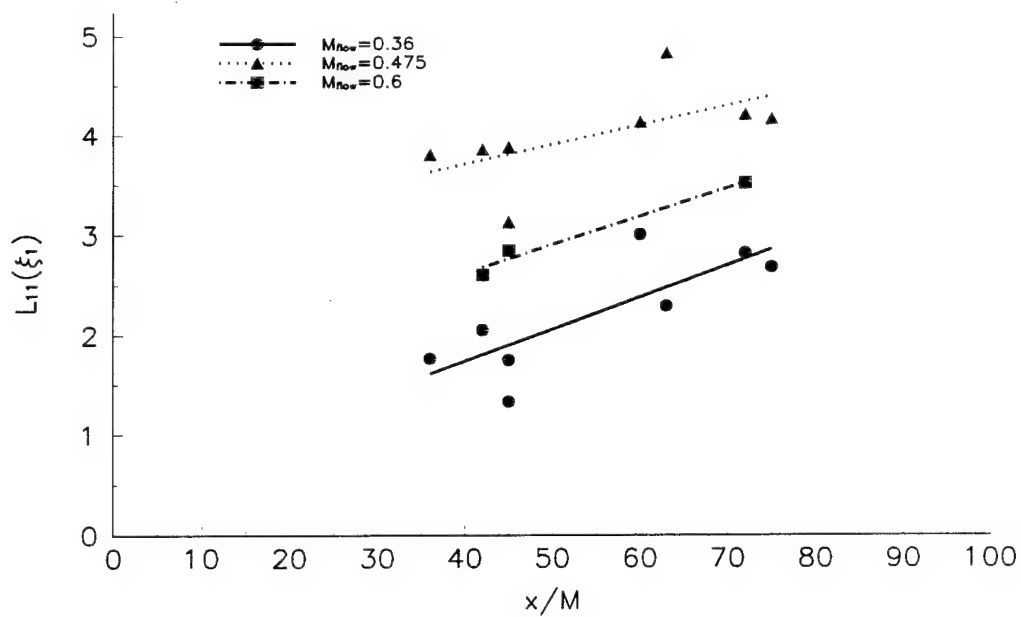


Figure 23: Longitudinal length scale for various experiments.

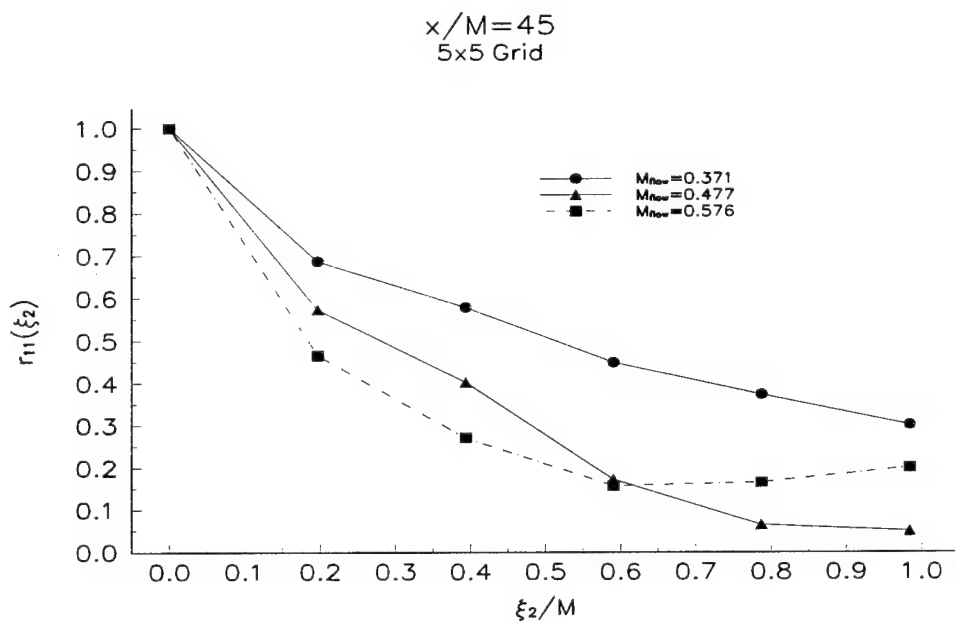


Figure 24: Space correlation in the lateral direction for three different flow cases.

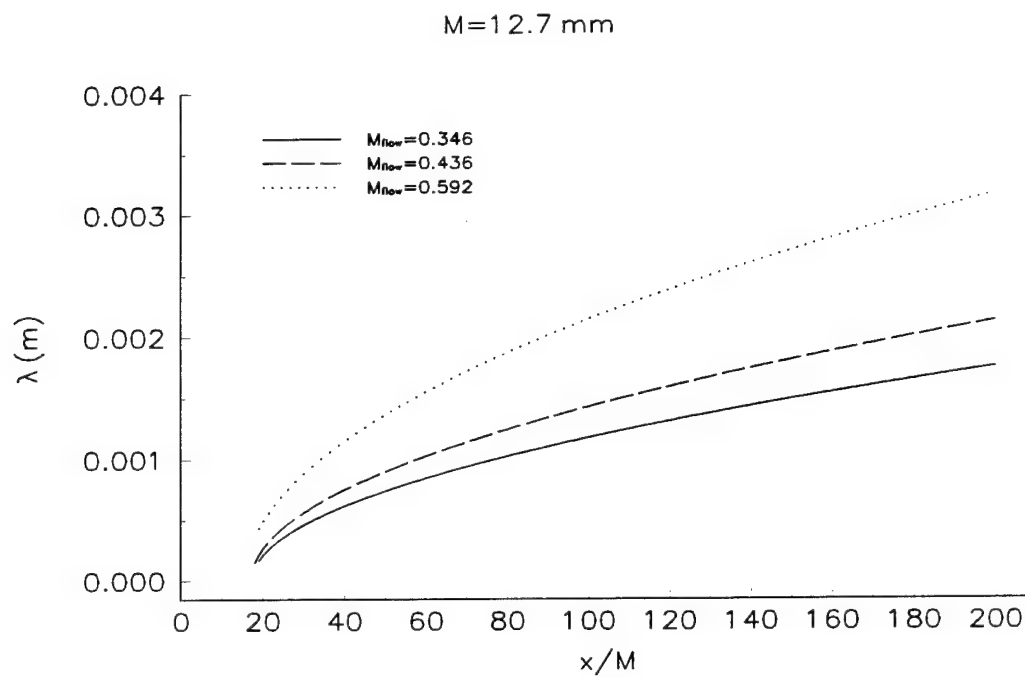


Figure 25: Taylor's microscale for three mean flow Mach numbers.

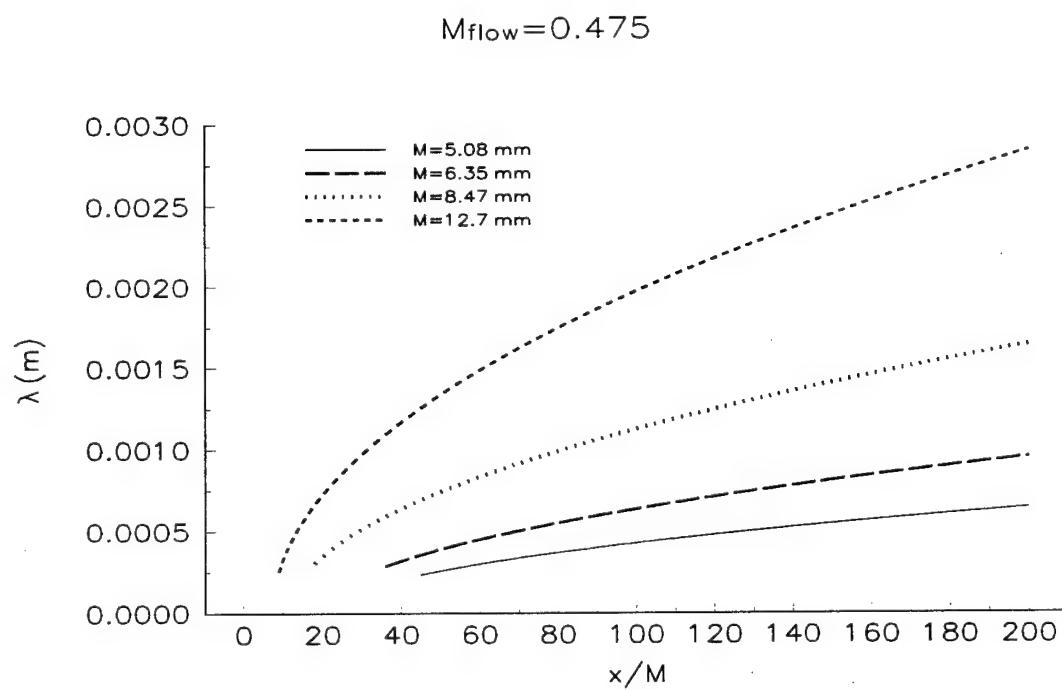


Figure 26: Taylor's microscale for several mesh sizes.

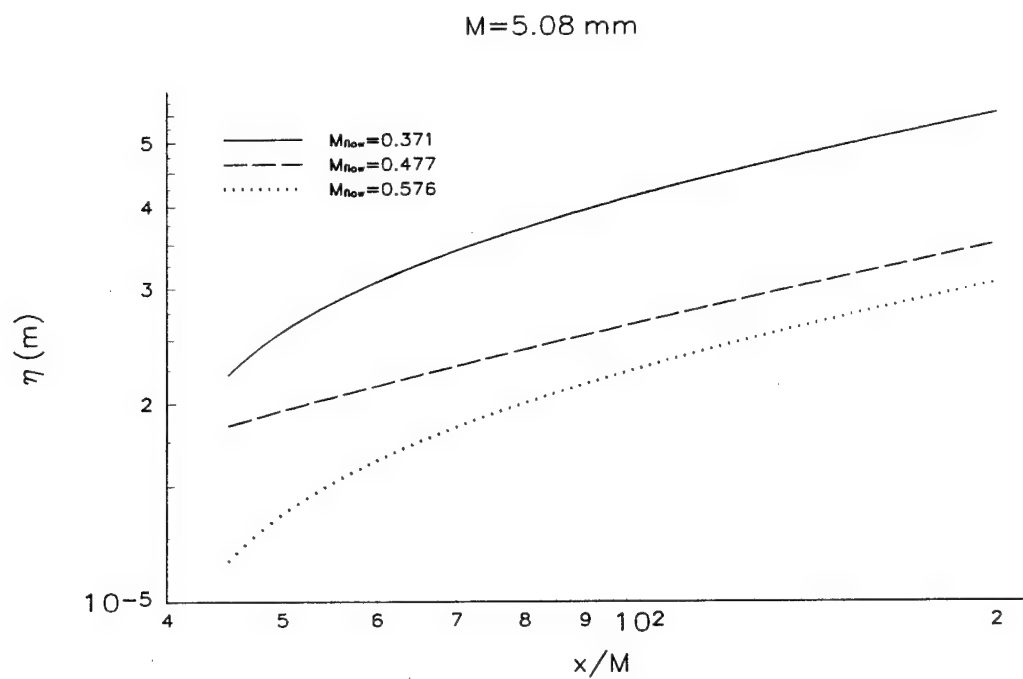


Figure 27: Kolmogorov's length scale for three mean flow Mach numbers.

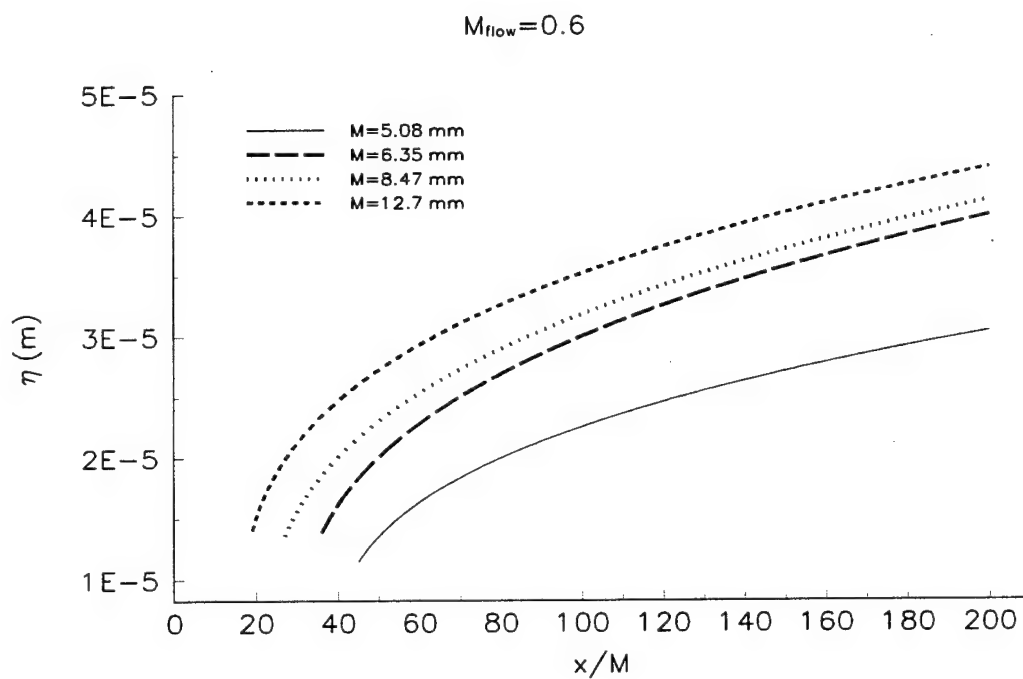


Figure 28: Kolmogorov's length scale for various mesh sizes.



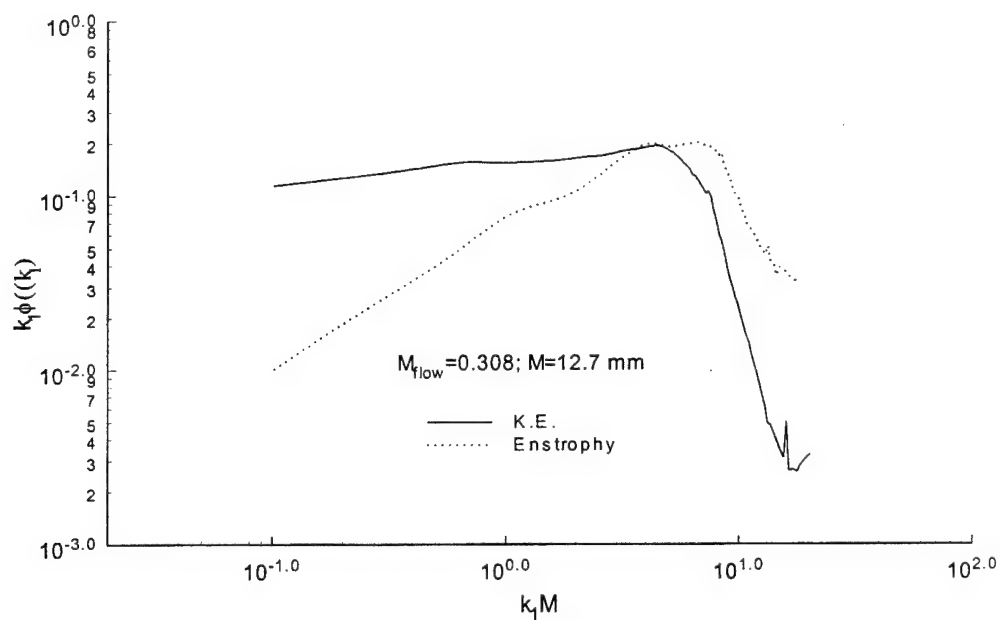


Figure 29: Weighted power spectral densities for turbulent kinetic energy and enstrophy

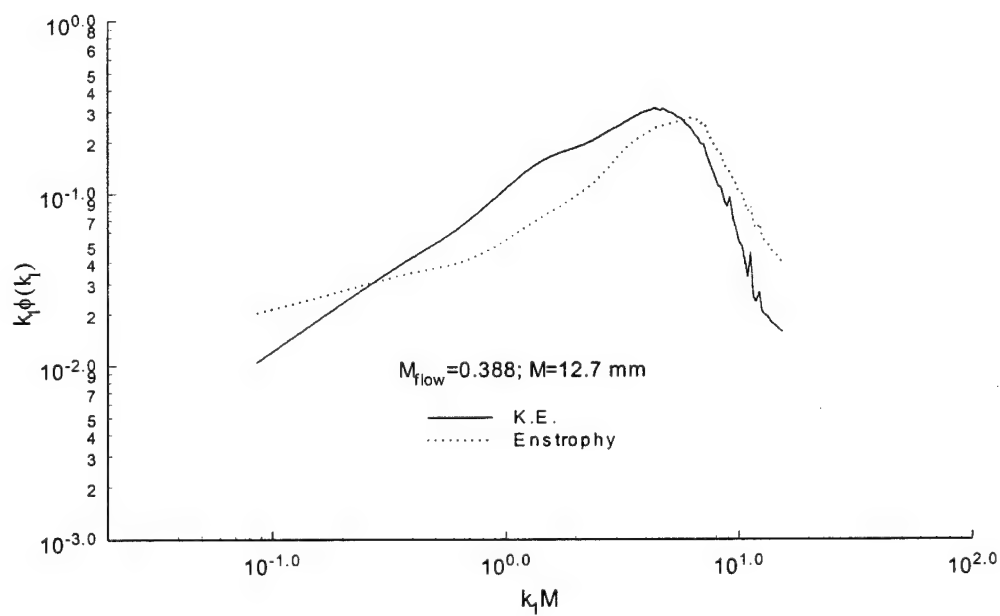


Figure 30: Weighted power spectral densities for turbulent kinetic energy and enstrophy

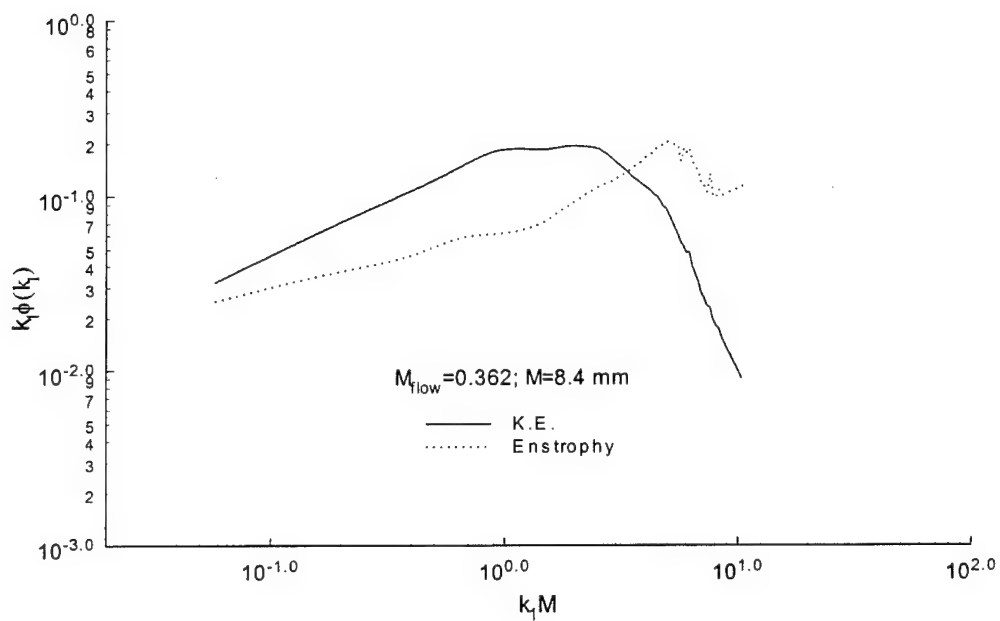


Figure 31: Weighted power spectral densities for turbulent kinetic energy and enstrophy

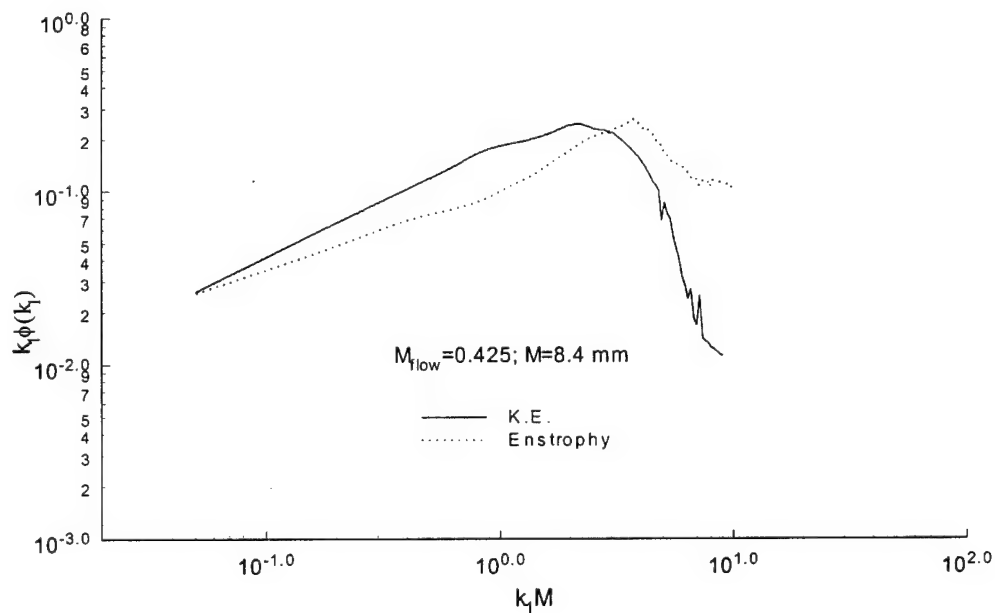


Figure 32: Weighted power spectral densities for turbulent kinetic energy and enstrophy

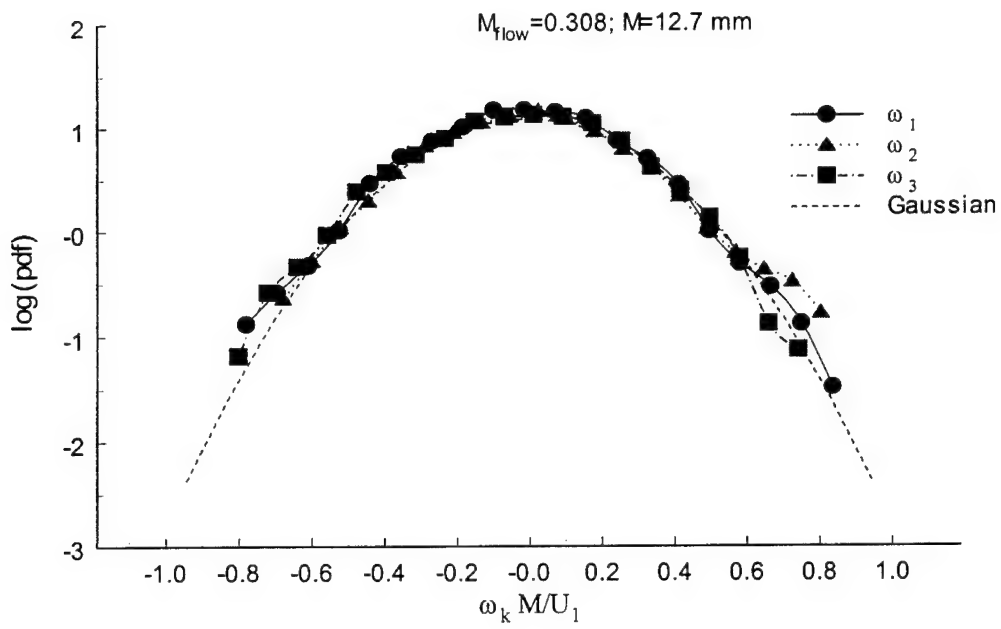


Figure 33a: Probability distributions of vorticity components

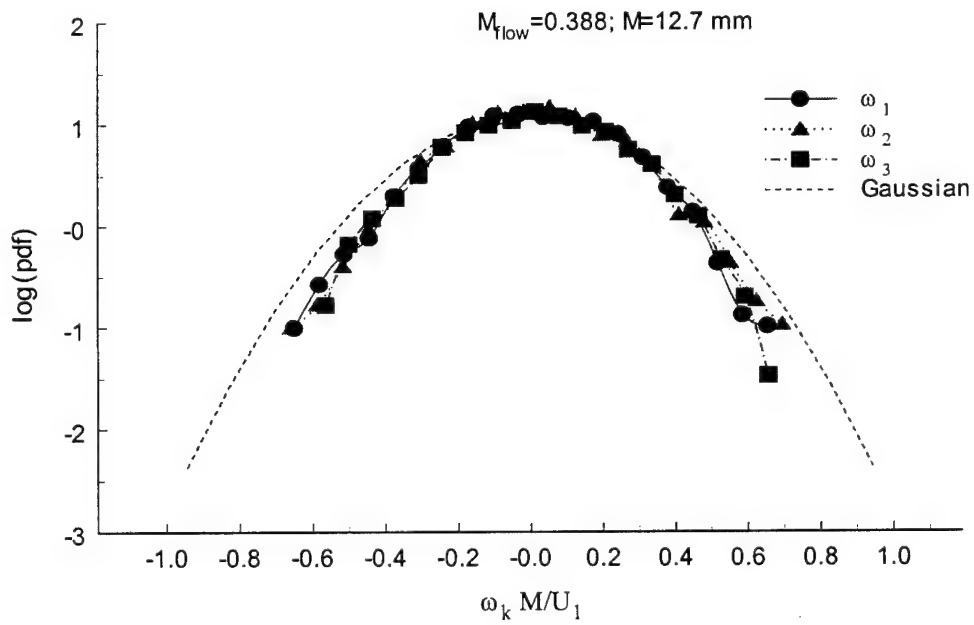


Figure 33b: Probability distributions of vorticity components

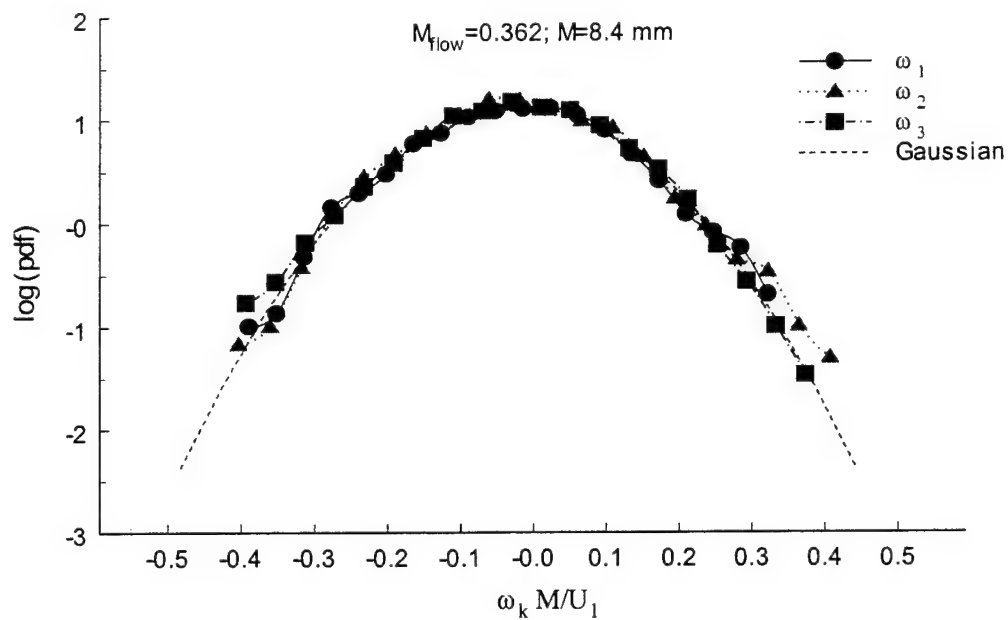


Figure 34a: Probability distributions of vorticity components

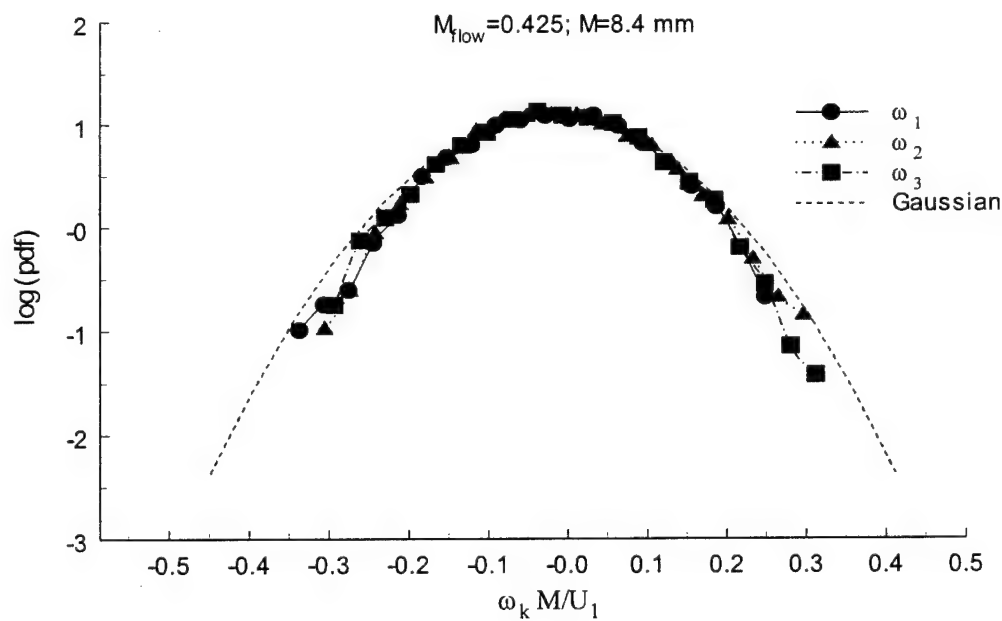


Figure 34b: Probability distributions of vorticity components

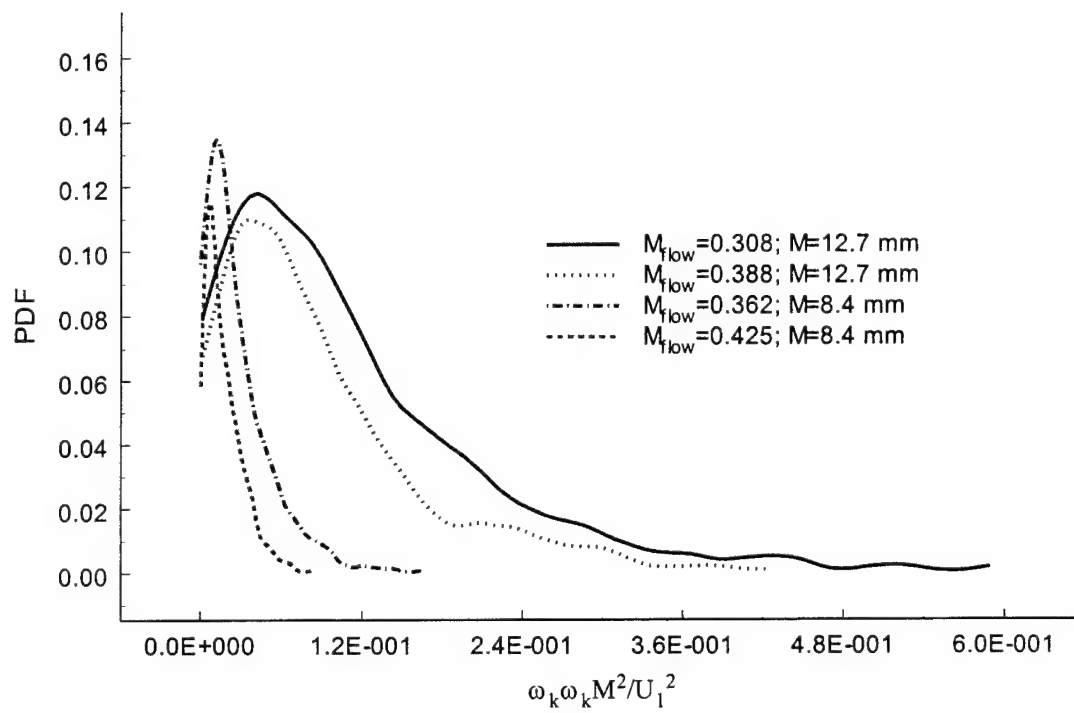


Figure 35: Probability distributions of enstrophy

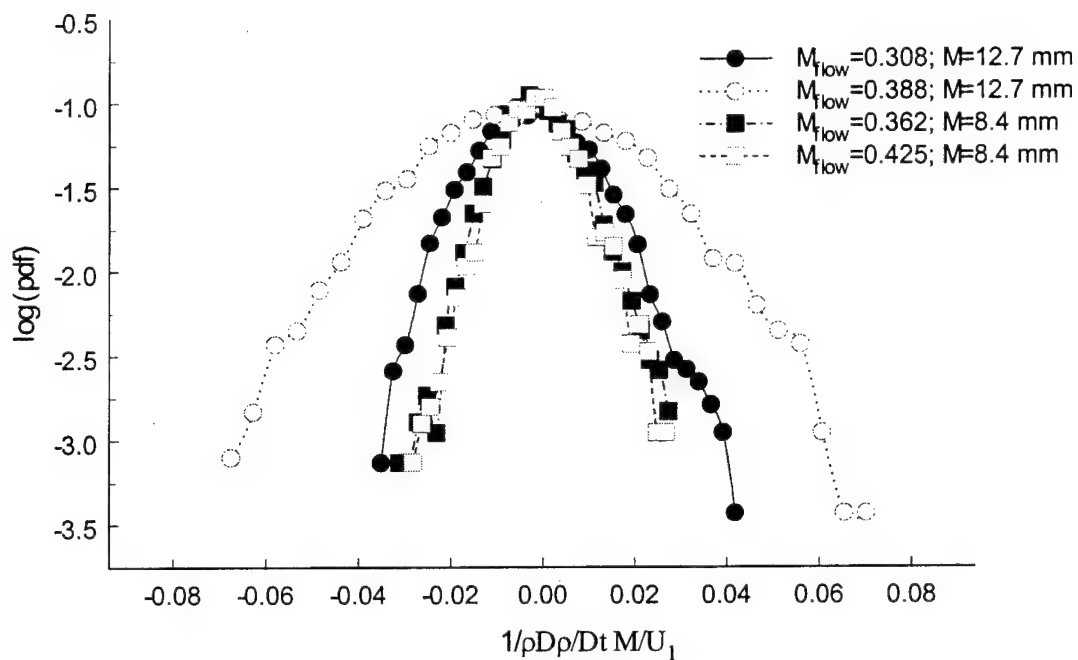


Figure 36: Probabability distributions of dilatation rate

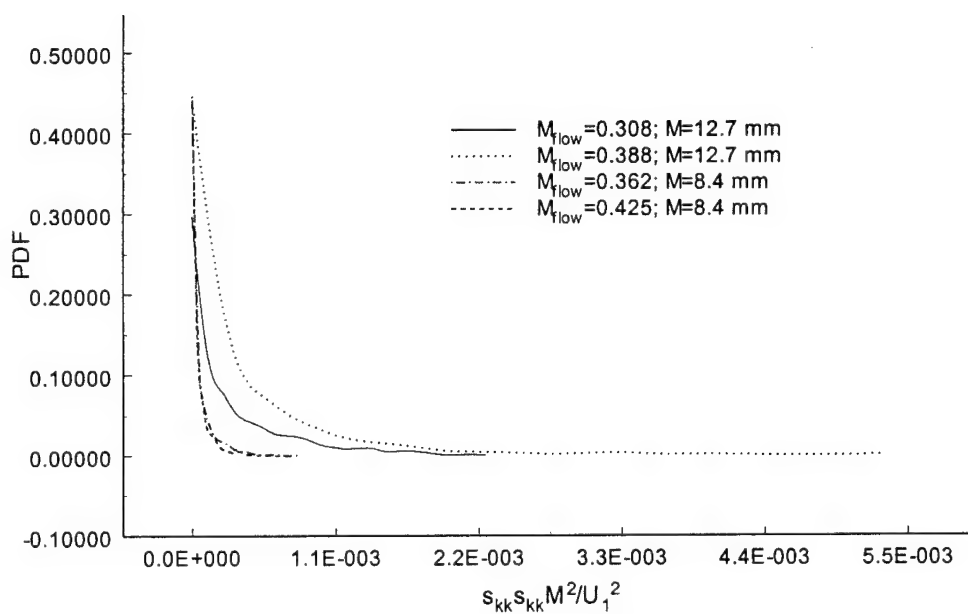


Figure 37: Probability distributions of compressible dissipation

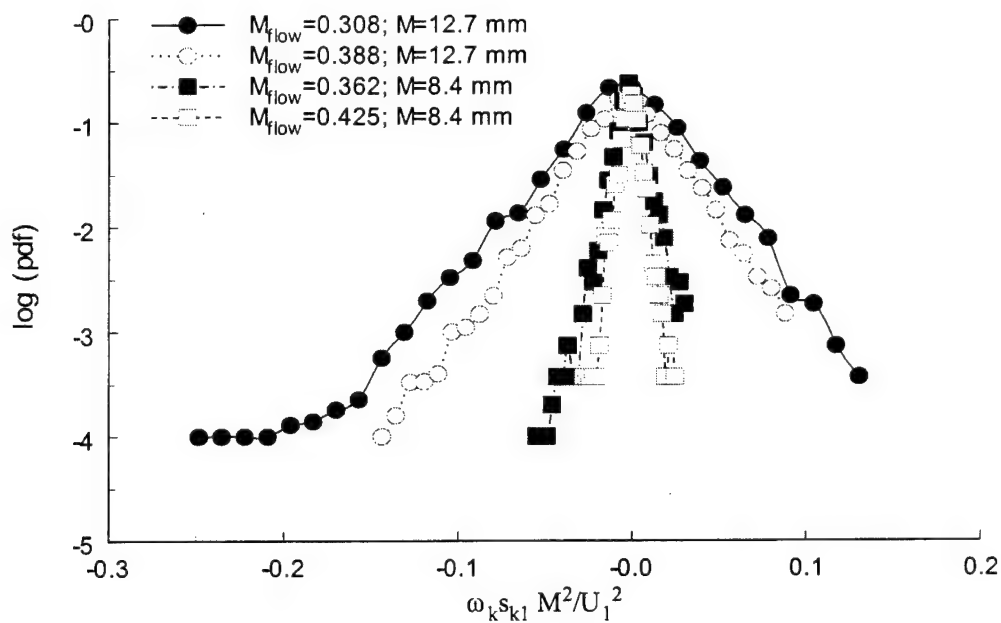


Figure 38: Probability distributions of stretching component  $\omega_k s_{kl}$

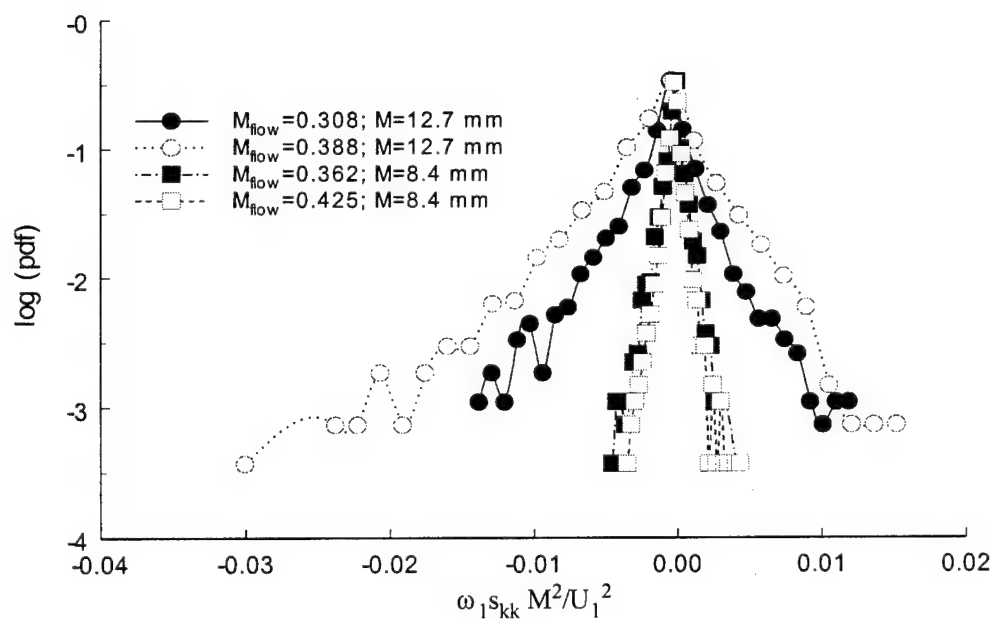


Figure 39: Probability distributions of compressible stretching component  $\omega_1 s_{kk}$

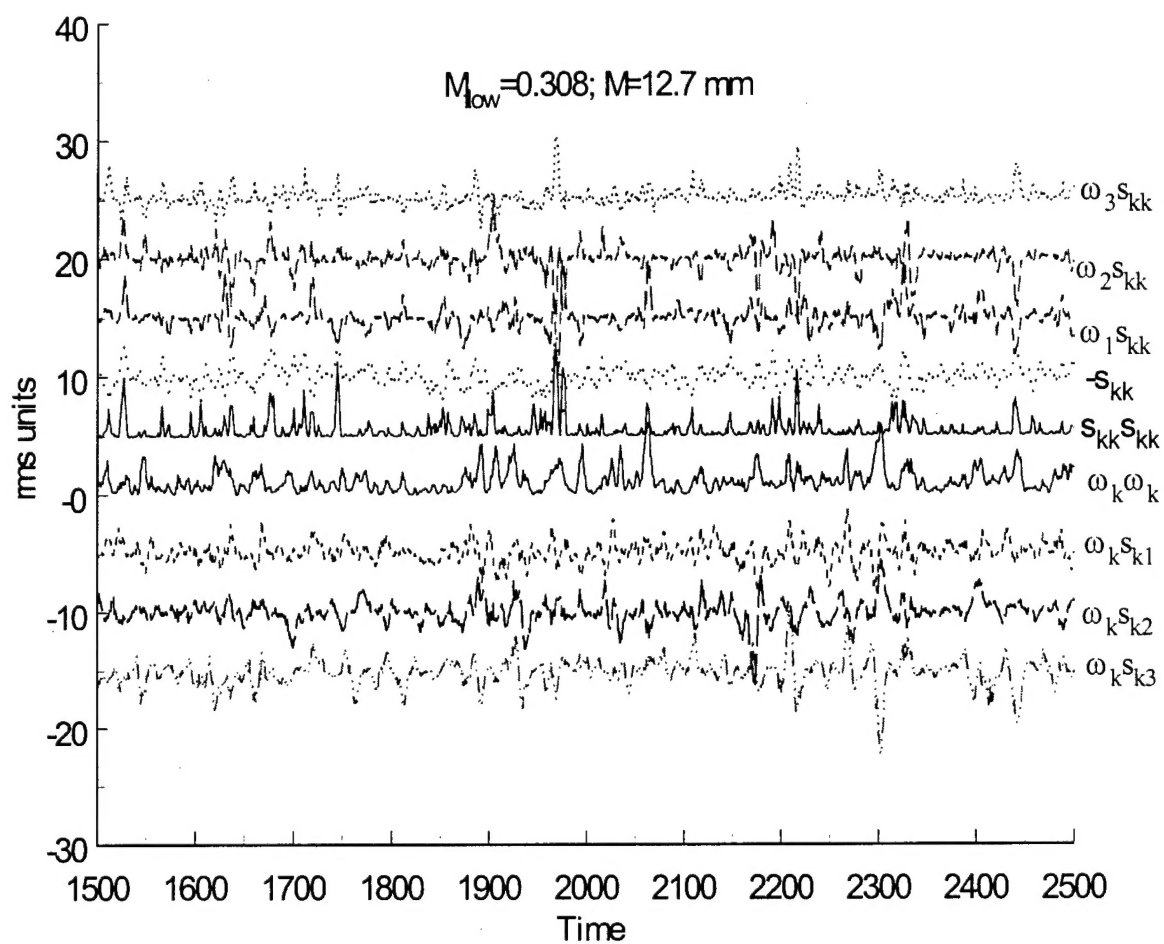


Figure 40a: Typical signals of various quantities normalized by their r.m.s. value.  
 (Actual signals are displaced)



$M_{\text{flow}}=0.308; M=12.7 \text{ mm}$

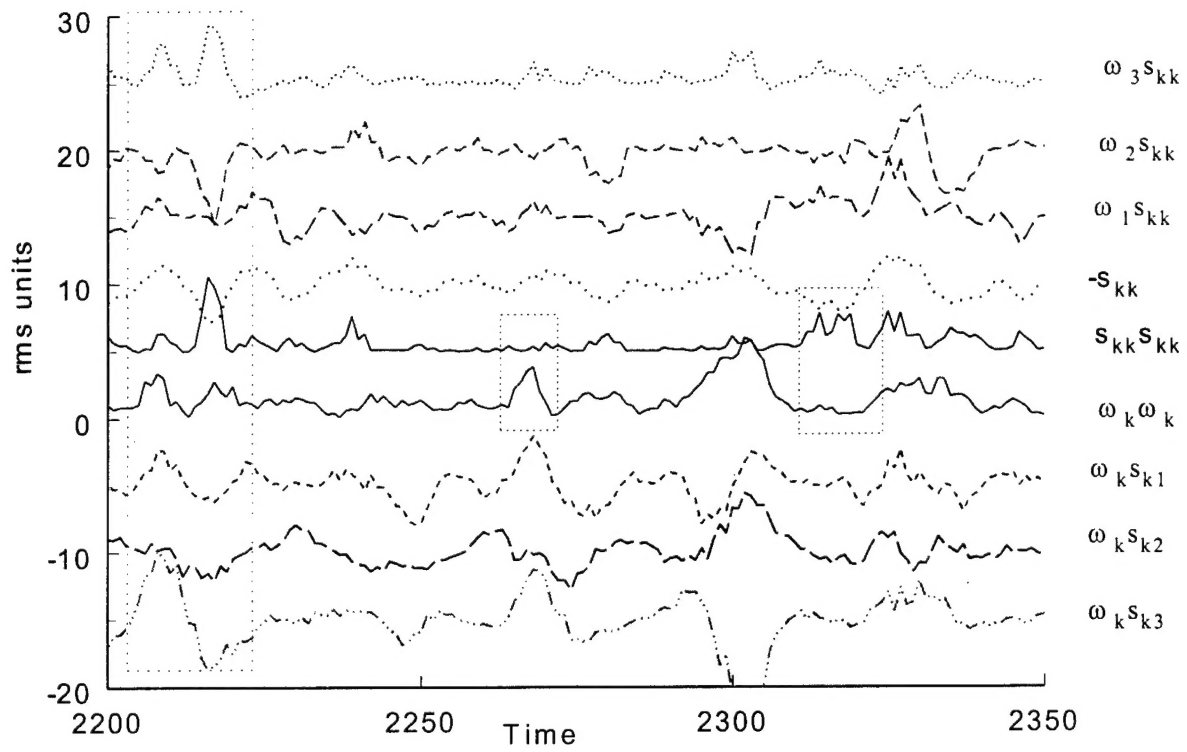


Figure 40b: Typical signals of various quantities normalized by their r.m.s. value.  
(Actual signals are displaced)

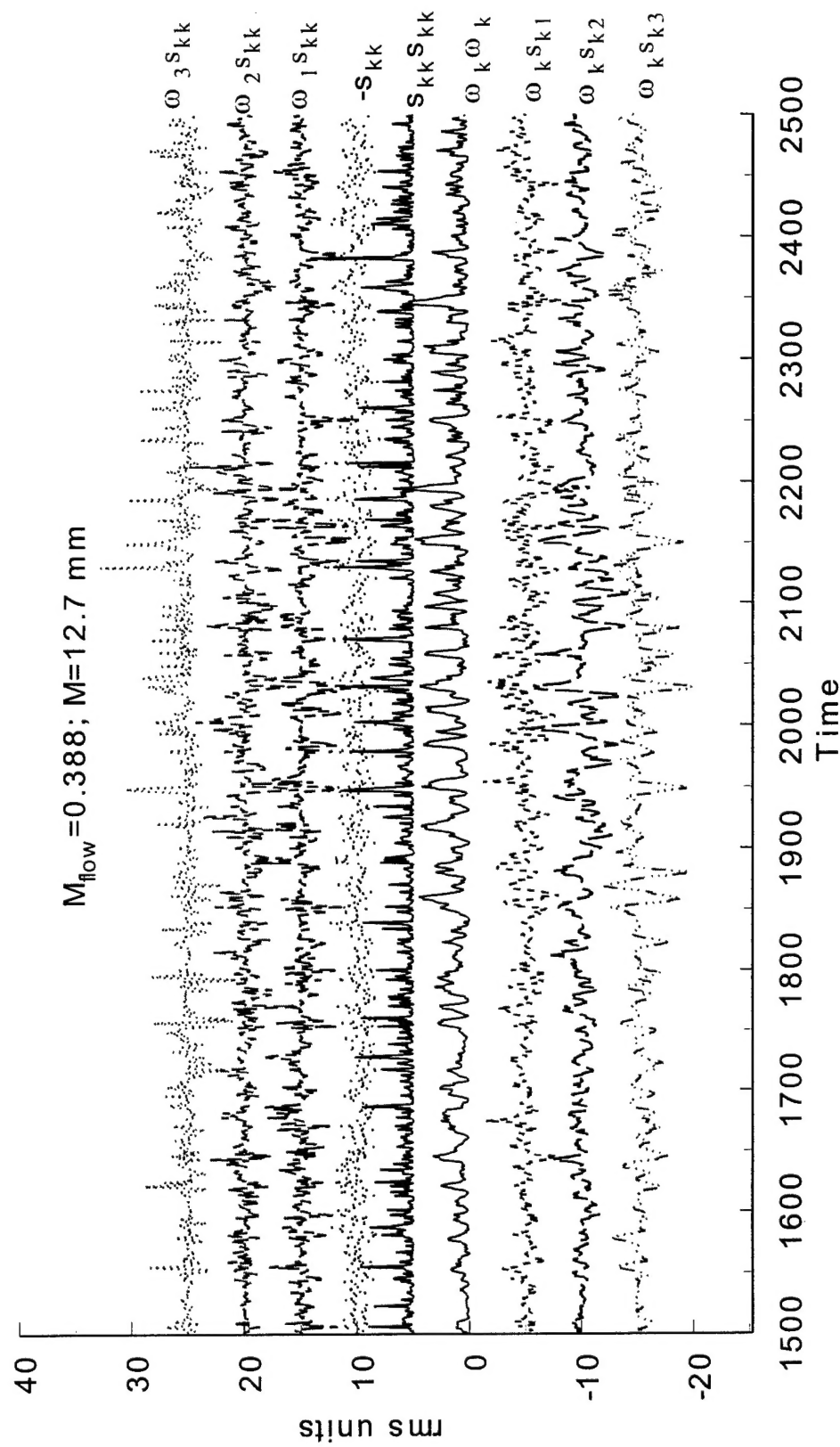


Figure 41: Typical signals

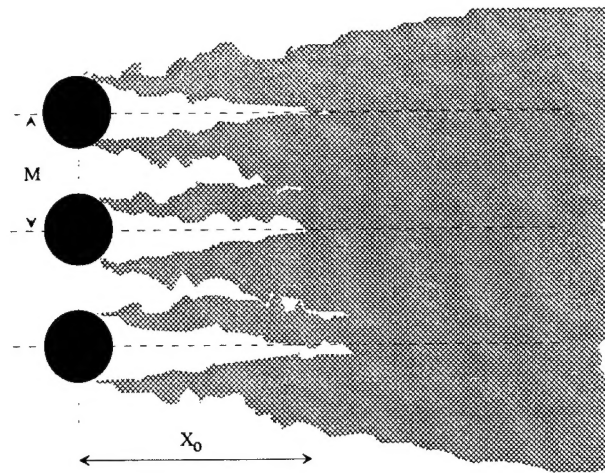


Figure 42a: Incompressible shear layer growth.

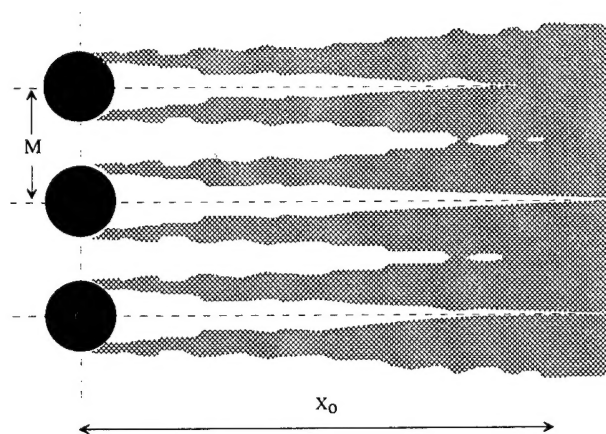


Figure 42b: Compressible shear layer growth.